Design and Applications of Super-Continuum Lasers and Time-of-Flight Camera in Spectroscopy and Healthcare

by

Kaiwen Guo

A dissertation submitted in partial fulfillment
of the requirements for the degree of
Doctor of Philosophy
(Electrical Engineering and Computer Science)
in the University of Michigan
2022

Doctoral Committee:

Professor Mohammed N. Islam, Chair
Associate Professor Ioulia Kovelman
Professor Fred Terry
Associate Professor Jenna Wiens

Kaiwen Guo

kaiwguo@umich.edu

ORCID ID: 0000-0002-5573-0233

© Kaiwen Guo 2022

Dedication

This dissertation is dedicated to my parents, Xiang Guo and Huiyun Wang and my partner Bingjie Li for their love and support throughout my life, my work and my struggles.

Acknowledgements

This dissertation would not have been possible without the warm and kind help from my family, my friends, my colleague, and my mentors.

I am thankful to my advisor, Professor Mohammed Islam, for his continuous help and support throughout my PhD study. From Professor Islam, I not only learned what it takes to become a qualified researcher and engineer, but also how to present my work and express my ideas. Furthermore, I am also grateful for Professor Islam of the opportunity to turn my research on the lab bench into a working prototype that can be deployed in real world.

I am thankful to my many mentors that guided me through my PhD study. Thank you, Professor Terry, for your broad knowledge and clever idea whenever I got stuck in my research. Thank you, Professor Ioulia Kovelman, for your insight of interpreting our measurement data into physiological phenomena. I also want to thank Mike Freeman, Carl DeWilde and Professor Jenna Wiens for your help and support dealing with numerous challenges I encountered during my research.

I am thankful to my colleagues in my lab. There is never a dull moment while working with you in lab. Ramon, thank you for the fun and energy you bring to lab every day and thank you for your secret food tour every time we go to California for conferences. Tianqu, thank you for brainstorming with me and discussing all the fun and crazy ideas at lab. Thank you, Lucas, Brandon, Genny, Robert, Ricky and Brian for your kind and generous help.

I am thankful for all my friends that I am fortunate to meet throughout my life. Without your companion and support, I would not overcome all the difficulties both in my study and in my life. Thank you Qiwen, Ruikun for the endless geeky debates during lunch and thank you for being the subjects that I test my recipes on. Thank you Changchuan for being my friends the past 16 years and thank you for the long phone calls to talk about our work, our life, and our stresses. I also want to thank everyone in my "WeChat lunch group" for giving me a place to laugh, to relax and to share my thoughts. Thank you, Feiran, Hanzhang and Yuxin for helping me figure out my true passion in career.

Most importantly, I am immensely thankful for my parents, Xiang Guo and Huiyun Wang and my girlfriend Bingjie Li. I would never have gotten this far without their support. I am grateful for my parents for their supports and sacrifices so that I can pursue my PhD in a different continent. Bingjie, thank you for being my strongest support during the most stressful time of my PhD study. I am very fortunate to have you believing in me and offering me advises when I am struggling. It is because of you that I know I will not be alone going through this strenuous and volatile time of my life.

Table of Contents

Dedication ii

Acknowledgements iii

List of Tables viii

List of Figures ix

Abstract xviii

Chapter 1 Introduction 1

1.1 Motivation and Chapter Introduction 1
1.2 Personal Contribution 3
1.3 Supercontinuum Source and Supercontinuum Generation 5
1.4 Supercontinuum Source and Infrared Spectroscopy 8
1.5 Indirect Time-of-Flight Camera and Remote Photoplethysmography 10
1.5.1 Indirect Time-of-Flight Camera 10
1.5.2 Photoplethysmography 12

Chapter 2 Long-wave Infrared Supercontinuum Generation to>12μm Based on Novel Chalcogenide Fibers 16

2.1 Introduction 16
2.2 Background and Motivation 17
2.3 LWIR SC Laser Design and Implementation 19
2.3.1 LWIR SC Laser Based on MOPA Configuration 19
2.3.2 Prototyping of the LWIR SC Laser 21
2.3.3 Characterizing SC Fiber Parameters for Optimum LWIR SC Generation 24
2.4 Experimental Results 30

2.4.1 Spectral and Power of Output of LWIR SC Laser 30
2.4.2 Output Beam Profile of LWIR SC Laser 34
2.4.1 Effects of SC Fiber Parameter on SC Generation 36
2.5 Modelling of SC Generation 39
2.6 Discussion 42
2.6.1 Beam Quality 43
2.6.2 Effects of Core/Cladding Composition 44
2.6.3 Effects of NA 47
2.7 Chapter Summary 48
Chapter 3 Non-destructive Characterization of Food Samples with Super-continuum Lasers 55
3.1 Introduction 55
3.2 Stand-off Non-Destructive Determination of Protein Level in Wheat Flour with a Super-Continuum Laser 56
3.2.1 Motivation for Non-contact Protein Level Concentration in Wheat Flour 56
3.2.2 Spectroscopy System with NIR SC Laser 56
3.2.3 Protein Level Prediction from NIR Spectrum 60
3.3 Non-Destructive Detection of Acrylamide in Potato Fries with a High-Power Supercontinuum Laser in both NIR and MIR 62
3.3.1 Motivation for Non-Destructive Detection of Acrylamide 62
3.3.2 Spectroscopy System using NIR and MIR SC Lasers 62
3.3.3 Predicting Acrylamide Level using NIR and MIR Spectrum 66
3.4 Discussion 70
3.5 Chapter Summary 73
Chapter 4 Contactless Measurement of HR and RR with a Time-of-Flight Camera 76
4.1 Introduction 76
4.2 Motivation 77
4.3 Experiment Setup and Procedure 79
4.4 Experiment Results 88
4.4.1 HR Measurement vs Motion Artifacts 93
4.4.2 Different Skin Color 95
4.4.3 Different Gender and Age 97
4.5 Discussion 100
4.5.1 Limitation of RR measurements 100
4.5.2 Limitation of motion compensated HR measurement using ToF camera 102

4.5.3 Future Improvements 103
4.6 Conclusion 104
Chapter 5 Contactless Vital Sign Monitoring (CVSM) System for Driver and Passenger Monitoring based on NIR ToF Camera 111
5.1 Introduction 111
5.2 Background and Motivation 112
5.3 Experiment Setup and Procedure 116
5.3.1 Hardware Configuration 116
5.3.2 HR and RR Extraction 117
5.2.3 In-Vehicle Testing of the System 123
5.4 Experiment Results 124
5.4.1 HR and RR Measurements in Bright and Dark Lighting Condition 124
5.4.2 On-the-Road Testing of HR and RR 126
5.5 Discussion 135
5.5.1 Potential Limitations and Improvements for HR measurements 135
5.5.2 Potential Limitations and Improvements for RR measurements 141
5.6 Chapter Summary 143
Chapter 6 Summary and Future Work 151

List of Tables

Table 2-1 Summary of Key Results and Setup in Recent MWIR/LWIR SC Generation Studies 19

Table 2-2 Summary of Related Fiber Parameter Used in This Study 24

Table 2-3 Three Groups of Fibers for SC Generation Performance Comparison 25

Table 2-4 Measured beam radius and calculated NA within each spectral range 36

Table 2-5 Beam characteristic at different spectral ranges 44

Table 2-6 Estimated Loss due to Cladding Absorption in 0.77NA As_2Se_3/As_4SSe_5 Fiber 45

Table 4-1 Summary of recent studies on IR camera-based HR/RR monitoring system 79

Table 4-2 Demographics of the participant population 87

Table 5-1 Summary of HR/RR measurement techniques used in vehicle 113

Table 5-2 Testing Condition for Each of the Scenario Tested 124

Table 5-3 Success rate and number of pixels transitioned across two consecutive frames at different frame rates 138

Table 5-4 Absolute mean error of RR measurement when the participant is wearing different type of clothing 143

List of Figures

Figure 1-1 Typical transparency window of various optical fiber materials [7] 7

Figure 1-2 Brightness comparison of a 5W SC laser against a conventional light source at 3000K 10

Figure 1-3 Schematic diagram for AM modulated ToF sensor 11

Figure 1-4 Typical working principle of a pulse oximeter comprising a LED and a photodetector. (b) Typical PPG waveform comprising of the AC and DC part 13

Figure 2-1 Schematic diagram of the SC Laser comprising the pump system and soft glass fiber cascade 21

Figure 2-2 Packaged LWIR SC Laser prototype showing the frontend box, the thulium amplifier and the fiber cascade enclosure 21

Figure 2-3(a) As2Se3 splice shown under splicer camera (top) and microscope (bottom) (b) “Tube on groove” mechanical splice: silica v-groove assembly (top) and nitrogen purged enclosure (bottom) 22

Figure 2-4 Loss of As2Se3 fibers showing As-O, Se-O, Se-H absorption band. 0.77NA As2Se3/As4SSe5 and 1.4NA As2Se3/As2S3 fibers also show much higher loss than 0.76NA As2Se3/ GeAs2Se5 fiber at longer wavelength 26

Figure 2-5 Dispersion (a) and MFD (b) of selenide fibers used in this study 27

Figure 2-6 Schematic Diagram of Fluoride Fiber Pump System 28

Figure 2-7 (a) Fiber loss comparison of the 0.3NA, 11µm core size and 0.26NA, 9µm core size. The absorption peaks on the 0.26NA fiber is likely from -OH absorption. (b) MFD comparison of the 0.3NA, 11µm core size and 0.26NA, 9µm core size InF3 fiber 28
Figure 2-8 Packaged MWIR Prototype System with cooling fan and power supply integrated .. 29
Figure 2-9 Measured laser output using a 12µm core size, 0.76NA, As2Se3/GeAs2Se5 fiber shows flat spectral expansion out to beyond 11µm. 31
Figure 2-10 Typical SC spectra for 6.5m, 7.5µm core size ZBLAN, 4m, 9µm core size As2S3, and 4m, 12µm core size As2Se3/GeAs2Se5 fibers. Power steps down and SC edge increases in successive cascade fibers 32
Figure 2-11 SC spectrum generated in 2.5m of 10µm core size As2Se3 fiber, showing a second plateau extending the wavelength edge to ~12 µm..... 33
Figure 2-12 Output spectra for 9m, 7.5µm core size ZBLAN, 4m, 9µm core size As2S3, and 2.5m, 10µm core size selenide fibers..... 34
Figure 2-13 Output beam profile and cross section between (a) 1.1-2.6µm (b) 3.25-3.75µm (c) 4.5-5µm (d) 3.3-5µm (e) 1-5µm (f) 7.5-11µm 35
Figure 2-14 SC Long wavelength edge of (a) different core size As2Se3 fiber. (b) different As2Se3 fiber core/cladding composition..... 37
Figure 2-15 SC Long wavelength edge of (a) different As2Se3 fiber NA. (b) different InF3 fiber NA..... 39
Figure 2-16 Comparison between simulated (blue) and experimental SC spectrum (red) in (a) ZBLAN fiber (b) in As2S3 fiber..... 41
Figure 2-17 Comparison between simulated (blue) and experimentally measured (red) SC spectrum in As2Se3/GeAs2Se5 12µm core diameter fiber 42

Figure 2-18 Simulated SC spectrum compared to experimentally measured SC spectrum in the 0.77NA, As_2Se_3 / As_4SSe_5 fiber 46

Figure 2-19 Measured loss in As2Se3/As2S3 core fibers with different core size 47

Figure 3-1 (a) Output spectrum of the SC laser (b) 10W SC laser and the block diagram used in this study 57

Figure 3-2 Optical setup of the dual-arm spectroscopy system with SC laser as light source used in this study 58

Figure 3-3 Ratio between signal and reference arm at 1500nm measured at 1m distance 60

Figure 3-4 (a)Typical reflectance spectrum of the wheat sample from 1100nm to 2400nm. (b) Reflectance spectrum after being second order derivative transformed 61

Figure 3-5 (a)PLS fitting between the predicted protein concentration versus the Dumas method measured protein concentration (b)Regression vector across the wavelength range 1160nm to 2350nm 61

Figure 3-6 (a) Diagram of the stand-off NIR spectroscopy system (b) High power SC laser and output spectrum used in the system 63

Figure 3-7 (a) Diagram of the MIR spectroscopy system (b) MIR SC laser used in the system 65

Figure 3-8 Typical French fry absorption spectrum measured with the SC laser between (a)1100-2100nm and (b) 2000-2500nm..... 67

Figure 3-9 Typical French fry absorption spectrum measured with the SC laser between 4000-8000nm measured with both a (a) MIR SC laser and a (b) commercial ATR-FTIR..... 67

Figure 3-10 (a) PLSR correlation plot (1100nm-2100nm) between predicted and measured acrylamide levels in French fries. (b) Regression vector plot (1100nm-2100nm) of the PLSR model using the NIR SC spectroscopy system. 68

Figure 3-11 (a) PLSR correlation plot (2000nm-2500nm) between predicted and measured acrylamide level in French fries. (b) Regression vector plot (2000nm-2500nm) of the PLSR model using the NIR SC spectroscopy system. 69
Figure 3-12 (a) PLSR correlation plot (1100nm-2500nm) between predicted and measured acrylamide levels in French fries. (b) Regression vector plot (1100nm-2500nm) of the PLSR model using the NIR SC spectroscopy system. 69
Figure 3-13 (a) PLSR correlation plot (4000nm-8000nm) between predicted and measured acrylamide level in French fries. (b) Regression vector plot (4000nm-8000nm) of the PLSR model using the NIR SC spectroscopy system. 70
Figure 3-14 PLSR correlation plot (4000nm-8000nm) between predicted and measured acrylamide level in French fries measured with a commercial FTIR 70
Figure 3-15 NIR SC laser output two orders of magnitude higher spectral density compared to black body source of same output 72
Figure 4-1 Experimental configuration for proof-of-concept HR, RR measurements using the Pico Flex indirect ToF camera. 80
Figure 4-2 Three ROIs used for RR and HR extraction: ROI-1 is used for HR measurements while ROI-2 is used for RR measurements 81
Figure 4-3 (a) Raw intensity signal from ROI-1 measured in dark/bright environment. The grayscale intensity shows a clear HR signal. (b) Frequency domain HR measured in dark/bright environment. The highest peak in the frequency domain corresponds to measured HR. 82
Figure 4-4 (a) Raw intensity signal from ROI-1 measured under alternating dark and bright environment. The ambient is switched on/off at an interval of 5 s. (b) Frequency domain HR

measured under alternating lighting condition. The highest peak in the frequency domain corresponds to measured HR 83
Figure 4-5 (a) Raw intensity signal and depth signal from ROI-1 when participants are intentionally staying still. The grayscale intensity shows clear HR signal (b) Raw intensity signal and depth signal from ROI-1 when motion artifact is present. The grayscale intensity is dominated by motion induced artifacts 84
Figure 4-6 HR extraction process from the 3D video streams of a ToF camera 86
Figure 4-7 RR extraction process from the 3D video streams of a ToF camera 86
Figure 4-8 (a) Time domain signal for HR extraction: HR signal after motion compensation (top), raw grayscale signal(middle) and raw depth signal (bottom). (b) Frequency domain HR signal: with motion-compensation (top), without motion compensation (bottom) 89
Figure 4-9 ROI-2 (chest) region depth signal, showing the periodic chest wall movement from respiration. The amplitude of the chest wall movement is 4 mm 90
Figure 4-10 HR measurements error rate on all 286 measurements with motion compensation (top) and without motion compensation (bottom) 91
Figure 4-11 Bland-Altman plot for HR measurements on all 286 measurements with motion compensation (left) and without motion compensation (right)..... 92
Figure 4-12 Percentage of ToF based RR measurements versus deviation from reference oximeter 93
Figure 4-13 Percentage of correct HR measurement within each motion score category..... 95
Figure 4-14 HR measurements error rate within groups of: lighter skin color(top) and darker skin color 96

Figure 4-15 Bland-Altman plot for HR measurements within groups of: lighter skin color(left) and darker skin color (right) 97
Figure 4-16 HR measurements error rate within groups of: male (top) and female (bottom)..... 98
Figure 4-17 Bland-Altman plot for HR measurements within groups of: male (left) and female (right) 98
Figure 4-18 HR measurements error rate within groups of: age>35 (top) and age<=35 (bottom) 99
Figure 4-19 Bland-Altman plot for HR measurements within groups of: age>35 (left) and age<=35 (right) 100
Figure 4-20 (a) Time domain signal for RR extraction: Raw depth signal from neck region not containing RR motion (top), raw depth signal from chest region containing RR motion (bottom). (b) Depth signal after ICA separation: Signal component with RR motion (top), signal component without RR motion compensation (bottom)..... 102
Figure 5-1 Experimental configuration for HR/RR measurements in vehicle with a ToF camera 117
Figure 5-2 Position of both ROI-1 and ROI-2 as seen by the ToF camera. The grayscale intensity and depth information from ROI-1 are used for HR measurement and the depth information from ROI-2 is used for RR measurements 118
Figure 5-3 (a)Raw intensity (red) and depth (blue) captured by the ToF camera. Depth change induced by motion (blue rectangle) is inversely proportional to the intensity, which is a key source of erroneous HR reading. (b) When motion artifacts are present, they create artifacts frequency components that overwhelm the actual HR signal..... 118

Figure 5-4 Processes to extract HR while driving using depth and grayscale information from a ToF camera 119
Figure 5-5 Processes to extract RR while driving using depth and grayscale information from a ToF camera 123
Figure 5-6 The user's face seen by an RGB camera (a) in both bright (top) and dark (bottom) condition versus the user's face seen by the ToF camera in both bright (top) and dark (bottom) condition 125
Figure 5-7 Time (Top) and frequency (Bottom) domain of the motion-compensated HR signal in both bright (a) and dark (b) environments 125
Figure 5-8 Waterfall diagram of the success rate of the HR measurements under different testing scenarios on highway 127
Figure 5-9 Waterfall diagram of the success rate of the HR measurements under different testing scenarios on local road 127
Figure 5-10 HR measurements error rate when participants sit in a parked vehicle with motion compensation (left) and without motion compensation (right) 128
Figure 5-11 Bland-Altman plot of HR measurements when participants sit in parked vehicle with motion compensation (left) and without motion compensation (right) 129
Figure 5-12 HR measurements error rate when participants sit in passenger seat on highway with motion compensation (left) and without motion compensation (right) 130
Figure 5-13 Bland-Altman plot of HR measurements when participants sit in passenger seat on highway with motion compensation (left) and without motion compensation (right) 130
Figure 5-14 HR measurements error rate when participants drive on highway with motion compensation (left) and without motion compensation (right) 131

Figure 5-15 Bland-Altman plot of HR measurements when participants drive on highway with motion compensation (left) and without motion compensation (right) 131
Figure 5-16 HR measurements error rate when participants sit in the passenger seat on local road conditions with motion compensation (left) and without motion compensation (right) 132
Figure 5-17 Bland-Altman plot of HR measurements when participants sit in the passenger seat on local road conditions with motion compensation (left) and without motion compensation (right) 132
Figure 5-18 HR measurements error rate when participants drive on a local road with motion compensation (left) and without motion compensation (right)..... 133
Figure 5-19 Bland-Altman plot of HR measurements when drive on a local road with motion compensation (left) and without motion compensation (right)..... 133
Figure 5-20 Typical RR motion measured by ToF camera (blue), and the RR measured by the reference respiration belt (red)..... 134
Figure 5-21 Percentage of ToF based RR measurements versus deviation from reference respiration belt 135
Figure 5-22 Periodic reflection from participant blinking could affect the location of the ROI-1 to jitter. The jittering can lead to additional intensity artifacts that will not be captured by the depth signal (a), leading to erroneous HR reading from the frequency domain (b)..... 136
Figure 5-23 HR measurements error rate when participants drive on highway recorded at 60 FPS (left) and 30 FPS (right)..... 137
Figure 5-24 (a)Grayscale signal from three different ROIs on face captured with the VCSEL illuminated ToF camera, showing similar patterns of artifacts among all three ROIs. (b)Extracted

sparse frequency component using method in [9], showing both HR and artifacts frequency components 140
Figure 5-25 Types of clothes worn by participants in this chapter. Participants are asked to sit in a parked car with engine running and breathe naturally during the measurements. 142
Figure 5-26 Respiration motion on chest measured by the ToF camera while the participants are wearing different types of clothing. Clear respiration patterns can be clearly seen in all cases. 142
Figure 5-27 Respiration motion on chest while the participants are wearing multi-layer cloth with air gaps in between. The chest wall motion measured by the ToF camera is attenuated due to the clothes' poor contact with body. 143

Abstract

The work in this dissertation focuses on expanding the capabilities of various technologies that enable optical contactless detection in various fields of applications. Specifically, we first discuss the design and implementation of supercontinuum (SC) lasers with ultra-broadband spectrum coverage into Long-Wave Infrared (LWIR). We then demonstrate a versatile Contactless Vital Sign Monitoring (CVSM) by leveraging the additional depth information from a ToF camera. Finally, we show that the CVSM system we demonstrate could be a key enabler for unobtrusive driver/passenger monitoring in a driving vehicle.

We solve the conundrum of generating ultra-broadband infrared spectrum and high output power at the same time in Chapter 2. We generate a 417mW supercontinuum spectrum from 1.57 to 12μm with a soft glass fiber cascade consisting of ZBLAN fiber, As_2S_3 fiber and As_2Se_3 fiber pumped by a nanosecond thulium MOPA system. By separating LWIR SC generation processes into a cascade of SC fibers with optimized coupling between each SC fiber, we circumvent the need of complex optical parametrical amplifiers and improved the reliability of the SC source. Our study also suggests that to efficiently generating SC into LWIR, fiber parameters, such as numerical aperture, core size, and core/cladding composition, need to be optimized.

Our SC generation methodology allows us to build monolithic all-fiber supercontinuum sources in both near and mid infrared wavelengths, which we then use to explore the benefits of SC based stand-off spectroscopy systems for non-destructive quality inspections. Specifically,

we demonstrate infrared spectroscopy systems that can predict concentrations of key chemical components of food samples in both the short-wave and mid-wave infrared spectral range. We measure 32 French fry and wheat flour samples with different acrylamide/wheat protein concentrations. Both of our predicted acrylamide/wheat protein concentrations show a good linear correlation to the reference concentration obtained through golden standard methods. Our results indicate that the SC based system could provide an alternative, non-destructive method to determine the concentration of key chemical components in processed food samples at a stand-off distance.

The latter half of this dissertation considers contactless technology for physiological parameter monitoring. In response to the COVID-19 pandemic, we develop a Contactless Vital Sign Measurement (CVSM) system that measures heart rate (HR) and respiratory rate (RR) of an individual with an indirect ToF camera. Compared with conventional cameras (IR or RGB), the additional depth information from the ToF camera allows us to compensate for motion artifacts during the HR measurement and directly derive the RR through the detection of chest wall movement during breathing. We conduct a pilot human study with 29 participants to show the system performs reliably across users of different skin color, age, and gender. We also show that our depth-based motion compensation greatly increases the reliability as well as the success rate (defined as measurement results within 10% of reference measurements) of the HR measurements.

We then further develop the CVSM system and demonstrate the system's capability of measuring HR and RR for in-vehicle driver/occupants monitoring. The indirect ToF used in the study is inherently robust against the illumination changes in the vehicle, while the depth information is used to compensate for motion induced intensity artifacts encountered during

driving. We investigate the system's performance in various scenarios including monitoring both drivers while driving on highway and local road. Our results show that our CVSM system is ambient light agnostic and the success rates of HR measurements on highway are 82% and 71.9% for passenger and driver respectively. Furthermore, we show that the system measures RR on users driving on highway with a mean deviation of -1.4 breaths per minute.

Chapter 1 Introduction

1.1 Motivation and Chapter Introduction

Being able to characterize a subject without physical contact has always been a major goal in fields such as material characterization, industrial inspection, or even medical diagnosis. Especially after the COVID-19 pandemic, contactless interaction is emphasized more than ever to contain the spread of the virus. Among numerous technologies been invented to reach this goal, optical methods in infrared have remained a persistent focus among researchers because this wavelength range is non-distracting to human user (invisible to naked eye) and at the same time provide rich information of the targets being measured. Two of the technologies of interest that emerged over the past decades are supercontinuum (SC) sources and Time-of-Flight (ToF) camera. In this dissertation, we discuss researches that advance the capabilities of these two technologies.

In Chapter 2, we demonstrate a novel SC source architecture that allows us to generate both ultra-broad band Long-wave Infrared (LWIR) spectrum and high output power at the same time. Specifically, we generate SC spectrum spanning from 1.57 to 12μm with highest on-time average power of 417mW with a cascade of soft-glass fiber and a Master Oscillator Power Amplifier (MOPA) based design. In addition, even with the multimode As_2Se_3 fiber, we measure a fundamental spatial mode output with near diffraction limit beam quality across a wide wavelength range. To effectively utilize our cascaded SC generation scheme, we study the effects of different core sizes, core/cladding composition, and numerical aperture (NA) to optimize the long wavelength edge of the generated SC spectrum. With high average power and

beam quality, this SC source could serve as an active illumination source that enable applications such as stand-off infrared spectroscopy to operate under conditions (e.g., in dark environment or under harsh weather) that are otherwise infeasible with natural or conventional light sources. For example, this light source has been deployed in a stand-off spectroscopy system that can detect trace amount of chemical particles from five meters away [1].

Following the development of the SC source, we subsequently discuss novel spectroscopy applications with our SC sources. In Chapter 3, we build SC-based stand-off spectroscopy system and measure key chemical concentrations in processed food samples. We show clear linear correlation between the measured infrared spectra and the concentrations measured by gold-standard methods. We measure the wheat flour samples in the NIR wavelength while measure the French fry samples in both NIR and MIR wavelength. We attribute the benefits of the SC based system to the high brightness empowered by the near diffraction limited beam quality of the SC source. Our results suggest that SC sources could enable the illumination of food samples from a distance that is hard to achieve with conventional light sources and therefore be used as a light source for non-contact and non-destructive quality monitoring system in food industry.

The other area this dissertation focuses on is to develop a Contactless Vital Sign Monitoring System (CVSM) that measures heart rate (HR) and respiration rate (RR) using a NIR indirect ToF camera. In Chapter 4, we describe the methodology of deriving HR and RR from the 3D video captured by the ToF camera. We develop a novel method that use the depth information from the ToF camera to compensate for motion artifacts which normally dominate underlying HR signal. Our pilot human study with twenty-nine participants of varying demographics shows that the depth-based motion compensation increases the success rate of HR

measurement to 75% from only 35% when only the 2D grayscale image is used. We further show that the system performs well among participants of various demographics such as skin color, gender, and age.

Subsequently, in Chapter 5, we build upon the CVSM demonstrated in Chapter 4 to monitor HR and RR of the driver/occupants in a moving vehicle. The ToF camera is agnostic to ambient light variation while the additional depth information allows to compensate for motion induced artifacts during driving. Thus, the CVSM system can address the challenges of varying ambient illumination as well as the interference from excessive motion while driving. Furthermore, to adapt for the complex environment in a car cabin, we propose a depth-based method to estimate the amount of motion during the different sections within a measurement period, therefore improving the reliability of HR measurements. We then systematically investigate the performance of the CVSM system by performing HR/RR measurements in various realistic environments with different degrees of motion from the roads and the drivers. Our study finds that with the depth-based motion compensation, HR measurement success rate increase from 13.6% to 71.9% while the user is driving on the highway. With the ability to measure two important physiological parameters at the same time, the ToF based CVSM system can be used as a low-cost, compact, and multi-modal sensor that enable applications such as in-vehicle sudden sickness detection, remote and in-patient patient monitoring, or unobtrusive public health screening.

1.2 Personal Contribution

The work presented in this dissertation also involves the contributions from my brilliant colleagues that I worked with during my PhD study. In this section, I would like to thank my coworkers for the help in making these projects possible and I would like to discuss my personal

contributions in each of the projects that are presented in this dissertation. For the LWIR SC laser development, I participate in the conceptualization of the SC architecture and propose a series of experiments to understand how different SC fiber parameters affect the SC generation in LWIR. Also, to assist the experiment design, I expand the capability of the existing numerical simulation tool to model the broadband SC generation in exotic fibers such as chalcogenide fibers. As for implementing the LWIR SC source, I succeed in making the first high efficiency fusion splice between sulfide fibers and selenide fibers, which turns out to be a crucial milestone that makes the high power LWIR SC source possible. I also lead the effort of optimizing the operating parameters and characterizing the SC output. Finally, I participate in turning the table-top SC source into a portable prototype that can be deployed in the field.

As for the spectroscopy system using the SC laser. I design and build the optical systems that measure the transmission/reflection spectrum of various food samples. I am also in charge of measuring the optical spectrum of various food samples.

Finally, for the CVSM project, I develop the method of using the depth information to compensate for the motion artifacts. Also, I write the program to process the 3D videos from the ToF camera to extract HR and RR automatically. I also lead the pilot study to confirm the CVSM system's uniform performance over users of different demographics. As for using the CVSM in the vehicle, I further develop the CVSM system to use in a driving vehicle and propose the method of using the depth data to assess the measurement quality of the HR measurements. Lastly, I also conduct the systematic investigation of the CVSM system's performance under different driving conditions.

1.3 Supercontinuum Source and Supercontinuum Generation

Supercontinuum (SC) Laser is a specialty light source that combines the brightness advantage of a single mode laser with the broadband advantage of a conventional light source such as halogen lamp or light emitting diode. The output brightness of a supercontinuum source can be several orders higher than halogen lamps while still covers a spectral range of several octaves. This unique combination allows supercontinuum laser to be an ideal source for applications such as microscopy and remote spectroscopy.

Supercontinuum generation was first discovered by Alfano and Shapiro [2] by propagating a high peak power optical pulse (usually from a mode-lock laser) through a nonlinear crystal. Over the years, supercontinuum generations have been discovered in many different mediums such as various gases, glasses, and inorganic liquids [3,4]. One of the most interesting categories of supercontinuum generation is supercontinuum generation waveguide such as optical fibers. Compared to bulk glass crystals, optical fibers have lower background loss over a broad spectral range as well as the superior confinement of optical pulse over a longer distance. These benefits enabled efficient supercontinuum generation with lower peak power and monolithic all-fiber design, which in turn makes them suitable sources for various industrial applications. Broadly speaking, SC generation in optical fibers can be described in two major categories: short-pulse regime supercontinuum generation (sub pico-second and shorter) and long-pulse regime (pico-second to nano-second) [5]. Both categories rely on optical non-linear effect to generate the broadband spectrum, but their properties vary due to different dominating non-linear effects involved in the SC generation process.

In a typical implementation of short-pulse regime supercontinuum generation, a high peak power femtosecond pump pulse from either a mode-lock laser or an optical parametrical

amplifier is injected into a very short piece of optical fiber (typically on the order of 10cm) to generate the SC spectrum. If the center wavelength of the pulse is within the anomalous dispersion regime of the optical fiber, the SC generation process will be strongly dominated by soliton-related effects. In the first stage of the SC generation, the pump pulse first goes through the soliton fission process, where the higher order solitons are broken up into a series of sub-pulses [6]. Through this process, the narrow input pump spectrum broadens into a broad SC spectrum symmetrically. Each of the sub pulses will undergo the process of solution self-phase shifting through Raman scattering. Therefore, the spectral expansion after the initial soliton fission becomes asymmetric where the long wavelength edge of the spectrum continues to expand while the shorter wavelength edge stays the same.

In contrast to the SC generation with femtosecond pulses, SC can also be generated with longer pulses (picosecond to nanosecond) with longer optical fibers at lower pump peak powers. Such lower peak power and pulse duration demands allow one to use more versatile pump sources for SC generation. For example, in this dissertation, we generate ultra-broadband mid-infrared SC spectrum by using a Master Oscillator Power Amplifier (MOPA) design, which enables scalable and high average output power at the same time. Unlike the soliton fission dominated process in the femtosecond regime, SC generation in the longer pulse regime heavily relies on four-wave-mixing and modulation instability at the beginning of the process to break the longer pump pulse into a train of femtosecond sub-pulses. Each of these modulation-instability generated pulses then undergo a mixture of non-linear effects such as self-phase modulation and soliton self-phase shifting, which broaden the narrow input spectrum into SC spectrums that could span several octaves. Even though this process sounds similar to the soliton fission process, the fundamental difference lies on the fact that modulation instability generated

pulses are seeded from noise, rather than the soliton dynamics as seen in the case of femtosecond regime [5].

In terms of the performance specifications of supercontinuum laser, two major parameters that we seek to expand on are wavelength coverage as well as output power. The output spectral range of a supercontinuum source is determined by a combination of multiple factors such as transparency window of the supercontinuum fiber, dispersion characteristics of the supercontinuum fiber, input (pump) peak power and wavelength, etc. To expand the wavelength coverage well into mid-infrared range, one need to understand and optimize each of these factors. The transparency window of the optical fiber is largely determined by the materials that the fiber is manufactured with. To achieve transparency in the mid-infrared regime, materials consist of heavier molecules are needed. Figure 1.1 shows the transparency window of some commonly used optical fiber material [7]. The transparency window of the widely used silica fiber ends at ~2.5um and therefore cannot be used for SC generation in the mid-infrared range. Instead, one can use chalcogenide fibers such as sulfide or selenide materials as their transparency window extend to ~7.5um and ~10um respectively.

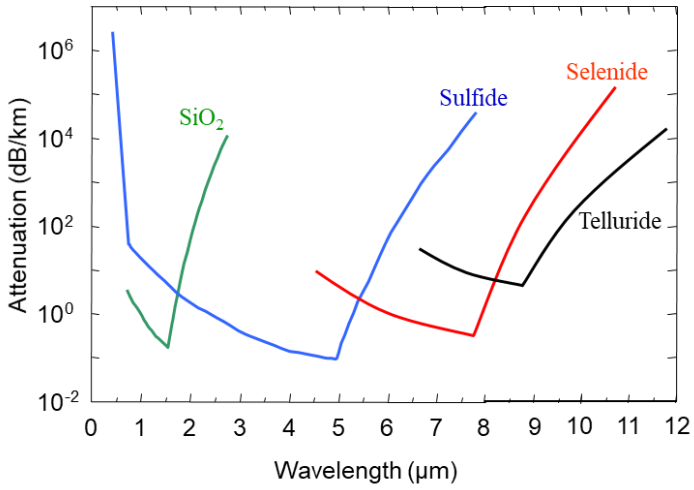


Figure 1-1 Typical transparency window of various optical fiber materials [7]

However, the use of chalcogenide material also brings new problems. In order to generate ultra-broadband SC spectrum efficiently, the pump wavelength length should be in the anomalous dispersion regime and close to the zero-dispersion wavelength (ZDW) of the supercontinuum fiber [8]. For chalcogenide fibers, ZDW is usually above 5um for the fundamental mode, which limits the availability of suitable pump sources. One solution is to use Optical Parametric Amplifiers (OPAs) to directly generate high peak power pump pulse beyond 5um and directly pump a short piece of chalcogenide supercontinuum fibers [8,9,10,11]. Such approach is straightforward but requires bulk and complicated OPAs as the pump source, which might not be realistic to use under challenging environments. In this dissertation, we present an alternative solution where we start with a MOPA based pump source at shorter wavelength length (1.9-2.4um) and use a cascade of various SC fibers to efficiently generate an ultra-broadband supercontinuum spectrum up to 12um. A more detailed discussion of the SC source design and numerical simulation for SC generation in pico-to-nanosecond regime will be presented in Chapter II of this dissertation.

1.4 Supercontinuum Source and Infrared Spectroscopy

Infrared spectroscopy is a technique based on the optical absorption from vibration of different atoms and molecules and is one of the most important analytical tools used nowadays. Various sampling and detection schematics have been developed to study samples at different spectral ranges in the infrared. Roughly speaking, the infrared radiation can be divided into three spectral regions: near-infrared region (~0.7 um to 2.5um), mid-infrared region (~2.5 um to 25 um) and far-infrared region (25um-100um). Since the supercontinuum source discussed in this dissertation covers wavelength range from ~ 0.7 to 12um, we will focus our discussion on near-infrared and mid-infrared regions.

The absorption in the near-infrared region can be attributed to the overtones or the combination of the fundamental stretching bands in the ~3-6 um [12]. Compared to fundamental bands, the overtone bands are usually broader and usually 1-2 orders of magnitude weaker in intensity, making it less ideal than mid-infrared region for both quantitative and qualitive analysis. However, one distinctive advantage of near-infrared wavelength range is that both light sources and detectors are more mature. These benefits make near-infrared source a suitable wavelength of choice for stand-off spectroscopic inspection. In fact, near-infrared spectroscopy has become a routinely used method for the compositional, functional and sensory analysis of food ingredients [13] since most food ingredients contains absorption features from the overtone and combinational band of C-H, N-H or O-H stretching [13]. In this dissertation, we take the advantage of the high-brightness advantage of the supercontinuum laser and demonstrate a stand-off inspection system based on a 10W all-fiber supercontinuum laser operating in the wavelength range between ~0.7um to 2.5um. The near-diffraction limit beam quality of the SC laser allows higher energy to be projected to the sample, which in turn could increase the acquisition speed as well as the operating range compared to near-infrared spectroscopy system with a conventional light source.

Moving into the mid-infrared region, the absorption features come from the fundamental bands which are both stronger and narrower than the near-infrared region. Most organic functional groups show distinctive absorption bands in the MIR region, which makes MIR a good wavelength range for direct and qualitive analysis [12]. For example, one of the chemicals of interest in this dissertation is acrylamide generated through the frying process of carbohydrates. Acrylamide has strong and distinctive absorption in the MIR region but no absorption features in the NIR region [14]. By measuring the samples in the MIR region, we

could directly measure the chemical absorption from acrylamide instead of the indirect measurements implied from the change of chemical composition of carbohydrates during the frying process. However, one disadvantage of conventional MIR spectroscopy is the lack of high brightness source in this wavelength range. Because of the black-body radiation curve, the energy density of a conventional light bulb can be very low in the MIR region. Because of this, SC sources can provide a unique opportunity for MIR spectroscopy because SC lasers offer both a flat spectrum across a wide spectrum range as well as brightness at least two orders of magnitude higher than conventional light sources such as halogen lamp (Fig.1.2). Moreover, because of the high brightness of the SC sources, they can be useful in applications such as evanescent wave spectroscopy or hyperspectral microscopy, where the broadband illumination needs to be focused into a small area to increase the optical throughput of such systems.

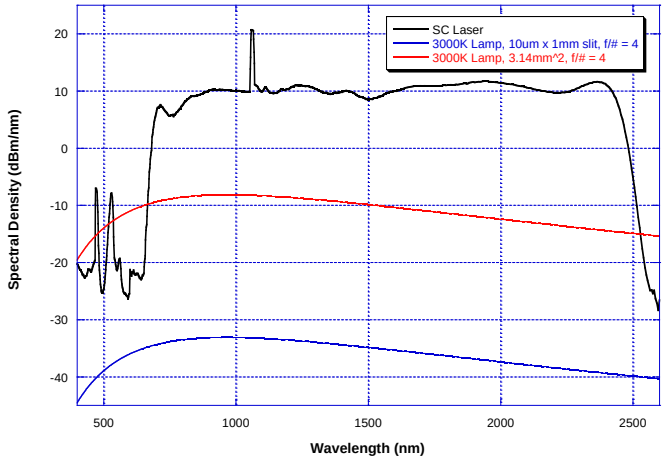


Figure 1-2 Brightness comparison of a 5W SC laser against a conventional light source at 3000K

1.5 Indirect Time-of-Flight Camera and Remote Photoplethysmography

1.5.1 Indirect Time-of-Flight Camera

Time-of-Flight (ToF) cameras are sensors that is capable of directly acquiring the 3D point cloud of an object or scene at high frame rate. Depending on the schematic of acquiring the

depth information, ToF cameras can be categorized into direct or indirect ToF cameras. Direct ToF camera obtains depth information by measuring the time traveled by the reflection light while the indirect ToF camera measures depth through the calculation of either the frequency or phase shift between the emitted and reflected light [15]. In this dissertation, the discussion will be focused on the amplitude modulated (AM) indirect ToF camera as this type of camera allows the capture of both intensity and depth data simultaneously on every pixel, which is critical to the application of remote photoplethysmography.

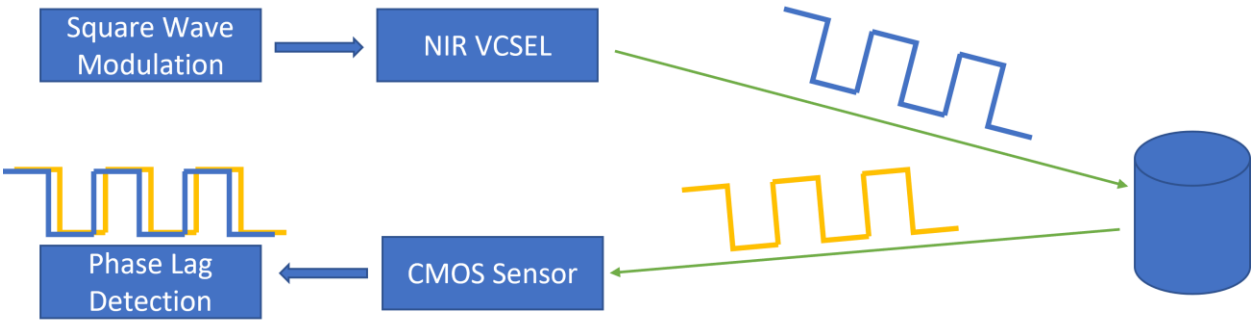


Figure 1-3 Schematic diagram for AM modulated ToF sensor

Typically, an AM modulated ToF sensor consists of two parts: the transmitter and the receiver. The transmitters in most cases are VCESL lasers at either 850nm or 940nm that are being modulated with either square wave or sinusoidal wave at tens of MHz frequency. The transmitted optical pulses are then reflected by the targets in the scenes and imaged by the CMOS sensor on the receiver side. Each of the pixel on the sensor detects a phase shifted signal with the amplitude of the phase shift depending on the distance of the objects imaged by each pixel. The depth seen by each pixel is then calculated as [15]:

$$d = c \times \frac{\Delta\varphi}{4\pi f_m} \qquad 1.1$$

Where $\Delta\varphi$ is the measured phase shift, c is the speed of light in air and f_m is the repetition rate of the light source.

1.5.2 Photoplethysmography

Photoplethysmography (PPG) is a widely used non-invasive technique that has been deployed to measure HR in both clinic and everyday scenarios since 1974 [16]. The working principle of PPG is based on the detection of small variation in light intensity caused by the changes of blood volume from heartbeat [17]. A typical pulse oximeter (Figure 1.4) based on PPG is very simple in design: a light source (usually red or infrared LED), and a photodetector to detect the light intensity change from the blood volume. A typical PPG signal is shown in Figure 1-4, which comprises of an AC signal superimposed onto a DC signal. Multiple physiological signals can be extracted from the AC and DC parts of the PPG signal. For example, HR can be intuitively extracted from the fundamental frequency of the AC signal and the perfusion index can be derived from the intensity ratio between the AC and DC signal [18]. More recently, with the maturing of the CMOS sensor, people have investigated using ambient light and cameras to measure PPG signal at a remote distance (rPPG). rPPG offers a low-cost and flexible solution to measure the HR of user in a contactless manner, which can expand the application scenarios for HR measurements. However, as a contactless technology, rPPG suffers from the vulnerability to motion artifacts and changing environment light. These disadvantages could significantly reduce the rPPG performance in these challenging situations. To overcome this, in this dissertation, we propose a solution using an indirect ToF camera to perform rPPG based HR measurement and respiration measurement at the same time. The active illumination and depth data from the indirect ToF camera allows us to perform rPPG based HR measurements regardless of ambient light condition and, at the same time, compensate for the motion induced artifacts that could corrupt the HR measurements. Detail of this system will be discussed in detail in Chapter 4.

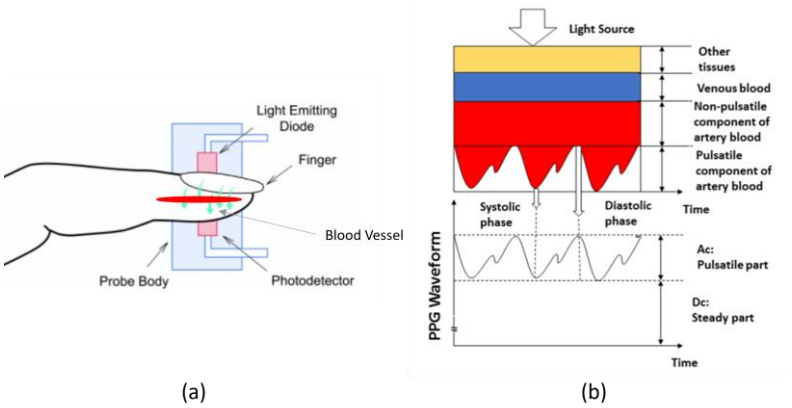


Figure 1-4 Typical working principle of a pulse oximeter comprising a LED and a photodetector. (b) Typical PPG waveform comprising of the AC and DC part

Reference

[1] Martinez, Ramon A., et al. "Active mid-wave to long-wave supercontinuum FTIR sensor for standoff chemical detection." Journal of Lightwave Technology 37.14 (2019): 3626-3636.

[2] Alfano, Robert R., ed. "The supercontinuum laser source." (1989): 458.

[3] Kandidov, Valeriy Petrovich, Il'ya Sergeevich Golubtsov, and Ol'ga Grigor'evna Kosareva. "Supercontinuum sources in a high-power femtosecond laser pulse propagating in liquids and gases." *Quantum Electronics* 34.4 (2004): 348.

[4] Hilligsøe, Karen Marie, et al. "Supercontinuum generation in a photonic crystal fiber with two zero dispersion wavelengths." *Optics Express* 12.6 (2004): 1045-1054.

[5] Dudley, John M., Goëry Genty, and Stéphane Coen. "Supercontinuum generation in photonic crystal fiber." *Reviews of modern physics* 78.4 (2006): 1135.

[6] Agrawal, Govind P. "Nonlinear fiber optics." *Nonlinear Science at the Dawn of the 21st Century*. Springer, Berlin, Heidelberg, 2000. 195-211.

[7] Aggarwal, Ishwar D., and Jas S. Sanghera. "Development and applications of chalcogenide glass optical fibers at NRL." *J. Optoelectron. Adv. Mater* 4.3 (2002): 665-678.

[8] Petersen, Christian Rosenberg, et al. "Mid-infrared supercontinuum covering the 1.4–13.3 μm molecular fingerprint region using ultra-high NA chalcogenide step-index fibre." *Nature Photonics* 8.11 (2014): 830-834.

[9] T.Cheng, et a, "Mid-infrared supercontinuum generation spanning 2.0 to 15.1 μm in a chalcogenide step-index fiber," Opt. Lett. 41, 2117–2120 (2016).

[10] Z. Zhao, et al, "Mid-infrared supercontinuum covering 2.0–16 μm in a low-loss telluride single-mode fiber," Laser Photon. Rev. 11, 1700005 (2017).

[11] D. Deng, et al, "Mid-infrared supercontinuum covering 3–10 μm using a As2Se3 core and As2S5 cladding step-index chalcogenide fiber," J. Ceram. Soc. Jpn. 124, 103–105 (2016).

[12] Stuart, Barbara H. Infrared spectroscopy: fundamentals and applications. John Wiley & Sons, 2004.

[13] Osborne, Brian G. "Near-infrared spectroscopy in food analysis." Encyclopedia of analytical chemistry: applications, theory and instrumentation (2006).

[14] NIST Webbook. https://webbook.nist.gov/cgi/cbook.cgi?ID=C79061&Type=IR-SPEC&Index=1#IR-SPEC

[15] Zanuttigh, Pietro, et al. "Time-of-flight and structured light depth cameras." Technology and Applications (2016): 978-3.

[16] Miyasaka, Katsuyuki, et al. "Tribute to Dr. Takuo Aoyagi, inventor of pulse oximetry." *Journal of anesthesia* 35.5 (2021): 671-709.

[17] Biswas, Dwaipayan, et al. "Heart rate estimation from wrist-worn photoplethysmography: A review." *IEEE Sensors Journal* 19.16 (2019): 6560-6570.

[18] Coutrot, Maxime, et al. "Perfusion index: Physical principles, physiological meanings and clinical implications in anaesthesia and critical care." *Anaesthesia Critical Care & Pain Medicine* 40.6 (2021): 100964.

Chapter 2 Long-wave Infrared Supercontinuum Generation to>12μm Based on Novel Chalcogenide Fibers

2.1 Introduction

With a SC source that comprises a master oscillator power amplifier (MOPA) followed by concatenated soft glass fibers, we generate SC with a continuous spectrum ranging from 1.57 to 12μm with highest on-time average power of 417mW at 33% duty cycle. The broadest spectrum is generated in 9m ZrF_4 -BaF_2 -LaF_3 -AlF_3 -NaF (ZBLAN) fiber, 4m of As_2S_3 fiber and 2.5m of 10μm core diameter As_2Se_3 fiber while the highest power is achieved in a cascade of 6.5m ZBLAN fiber, 4m of As_2S_3 fiber and 4m of 12μm core diameter As_2Se_3 fiber.

In both a tabletop and a packaged prototype SC laser, we measure a fundamental spatial mode output with near diffraction limit beam quality across a wide wavelength range, which is somewhat unexpected because the As_2Se_3 fiber is multimode below 12μm wavelength. We study the SC generation behavior in As_2Se_3 fibers with different core sizes, core/cladding composition and numerical aperture (NA) to optimize the long wavelength edge of the generated SC spectrum. Furthermore, simulations are used to confirm the results as well as to predict fiber improvements for further wavelength expansion. Our results suggest that low loss cladding material, well confined fundamental mode through high fiber NA and optimized fiber core size are relevant parameters for generating high power broad SC spectra covering the mid-wave infrared (MWIR) and a large portion of the long-wave infrared (LWIR) spectral regions. With high average power and beam quality, this SC laser could serve as a controllable light source in applications such as stand-off infrared detection, spectroscopy and medical diagnostics and treatments [1]. For

example, such light source can be used as an illuminator in remote sensing to project a beam over a long distance [2].

This chapter is organized as follows. In Section 2-2, we discuss the current state-of-art in LWIR SC generation as well as the motivation behind our approach to LWIR generation. In Section 2-3, we describe the experimental setup as well as fiber characteristics used in the studies. In Section 2-4, we present the experimental results including our best SC spectrum, beam quality measurements and comparison of SC spectrum generated in fiber with different parameters. Section 2-5 describes the numerical modelling employed to verify and predict the SC generation in soft glass fibers. In Section 2-6, we provide our explanations on the experimental results as well as discuss their implications on SC generation in the LWIR spectral region. We then summarize this chapter in Section 2-7.

2.2 Background and Motivation

LWIR SC sources can provide high-brightness illumination with a continuous spectrum covering the infrared fingerprint band, where most chemicals have distinctive absorptive signatures. In recent years, with the maturing of low-loss chalcogenide fibers, SC sources that generate LWIR [8–14 μm] and MWIR [3–8 μm] light through soft glass fiber such as chalcogenide fibers have attracted much attention. For example, in 2012, Gattass et al. reported an all-fiber SC system based on chalcogenide fibers with average power of 565 mW that covers wavelength from 1.9 μm to 4.8 μm [3]. In 2014, Petersen et al. first reported an 0.15 mW ultrabroad SC spectrum that covers 1.4–13.3 μm with a short piece of GeAsSe fiber pumped by a mid-infrared optical parametric amplifier (OPA) centered at 6.5 μm [4]. In 2015, Deng et al. generated a <4 mW, 3 – 10 μm SC spectrum with a As_2Se_3 / As_2S_5 core/ cladding material fiber

using a 7 μm OPA [5]. Kedenburger et al. reported high-power SC generation from 2.3 μm to 4.9 μm with As_2S_3 fiber pumped by a tunable OPA [6]. A multi-milliwatt SC source covering up to 7.5 μm is reported by Moller et al. through pumping a $As_{38}Se_{62}$ suspended core selenide fiber with a high-rep-rate OPA [7]. In 2016, an ultrabroadband SC spectrum covering 2–15.1 μm was achieved by pumping a short piece of As_2Se_3 fiber with a tunable OPA [8]. Zhang et al. reported a 17 mW SC spectrum from 2.2 μm to 12 μm with a GeSbSe/GeAs fiber and a femtosecond OPA [9]. Also in 2016, a SC system based on cascading multiple soft glass fibers was reported. Petersen et al. demonstrated a SC source with concatenated ZBLAN and suspended core selenide fiber with 6.5 mW output power [10]. Robichaud et al. reported a 1.5 mW SC source that covers 3–8 μm by cascading ZBLAN and AsSe fiber to an erbium-doped ZBLAN fiber amplifier [11]. In 2017, Petersen et al. reported 35.4 mW SC covering 1–11.7 μm generated in a tapered photonic crystal fiber (PCF) pumped by a femtosecond mode-locked laser [12]. Hudson et al. generated more than 30 mW SC spectrum that covers 1.8–9.5 μm by pumping tapered As_2Se_3 fiber with a holmium-doped ZBLAN fiber laser [13]. Also in 2017, Zhao et al. generated a 2–16 μm SC spectrum with a 7 μm OPA pumped telluride fiber [14]. To place this work in context, recent results and brief experimental conditions of these studies are summarized in Table 2-1. As we reported in [15], we generate 417 mW of LWIR SC generation covering 1.6 μm to >11 μm wavelength range with a concatenated soft glass fiber setup pumped by a thulium (Tm) MOPA system. In this chapter, we will provide a more detailed study on the generated SC spectrum, spatial mode, as well as the influences of different selenide fiber parameters on ultra-broadband SC generation in the LWIR region.

Table 2-1 Summary of Key Results and Setup in Recent MWIR/LWIR SC Generation Studies

Ref	SC Fibers	Pump Wavelength (μm)	Output Power (mW)	Spectral Range (μm)	Rep Rate	Pulse Width
[3]	10 μm core size As_2S_3 step-index	2	565	1.9–4.8	10MHz	40ps
[4]	16 μm core size As_2Se_3/GeAsSe step-index	6.3	0.1	1.4-13.3	1kHz	100fs
[5]	27 μm core size As_2Se_3/As_2S_5 step-index	7	<4	3-10	1kHz	200fs
[6]	9μm core size As_2S_3 step-index	4.1	550	2.3-4.9	42MHz	450fs
[7]	4.5 μm core size suspended core As_38Se_{62}	4.4	15.6	1.7-7.5	21MHz	320fs
[8]	15 μm core size As_2Se_3/$AsSe_2$ step-index	9.8	<3.8	2-15.1	1kHz	170fs
[9]	6μm core size GeSbSe/GeAs step-index	4.5	17	2.2-12	21MHz	330fs
[10]	4.5 μm core size suspended core $As_{38}Se_{62}$ fiber	2	6.5	2-7	40kHz	3ns
[11]	18 μm core size AsSe step-index	2.8	1.5	3-8	2kHz	400ps
[12]	Tapered $Ge_{10}As_{22}Se_{68}$ PCF	4	35.4	1-11.5	21MHz	252fs
[13]	3μm core size tapered As_2Se_3/As_2S_3 fiber	2.87	>30	1.8-9.5	42MHz	230fs
[14]	20 μm core size GeTeAgI Step-index	7	<11.5	2-16	1kHz	150fs
[15]	12 μm core size As_2Se_3/GeAsSe step-index	2	417 (on time)	1.57 to >11	800kHz	1ns

2.3 LWIR SC Laser Design and Implementation

2.3.1 LWIR SC Laser Based on MOPA Configuration

We use a cascade of soft glass fibers pumped by an all-fiber nanosecond MOPA system to generate broadband SC. A block diagram of the SC laser system, shown in Fig. 2-1, comprises a MOPA pump system and a cascade of three soft glass fibers for SC generation. The pump system comprises a distributed feedback seed laser diode operating at 1.553μm, followed by a forward pumped erbium /ytterbium co-doped fiber (EYDF) pre-amplifier, a backward pumped EYDF mid-stage amplifier and a backward pumped thulium (Tm) power amplifier. To prevent

back-reflection and reduce noise, an isolator and a bandpass filter are placed in between the pre-amp and mid-amp. Within the pump system, 1.1 ns optical pulses from the seed laser with variable rep-rate from 100 kHz to 800 kHz are first amplified through the first two stages of the EYDF amplifiers. The amplified signal undergoes pulse breakup induced by modulation instability in 10 m SMF 28 fiber (8.2 μm core diameter, 0.14 NA), and these pulses spectrally extend into a 1.5μm to 2.4μm SC spectrum through soliton self-frequency shifting. A fiber-based mode field adapter (MFA) then couples the generated SC into a large mode area, 8m double-clad thulium fiber (25/400 core/cladding diameter) power amplifier. The amplified signal is coupled into an output MFA and generates a SC spectrum covering 2-2.8μm with an average peak power of ~15kW within the MFA output pigtail fiber (7μm core diameter, 0.2NA). Further details of this MOPA pump system are provided in reference [16].

The advantage of using a thulium amplifier is that spectral components below 2μm get absorbed, while those above 2μm are further amplified. Therefore, SC expansion starts at 2μm instead of 1.5μm, improving the SC generation efficiency. Moreover, by reducing the residual power at 1.5μm, we observe an increase of damage threshold in the selenide fiber, which we think is related to higher background and two photon absorption in As_2Se_3 fiber near 1.5μm [17,18]. The power amplifier is also modulated by a 33% duty cycle, 100Hz square wave to reduce the thermal load while maintaining a high average power output when the power amplifier in on. With the MOPA design, the average output power can be changed by varying the system rep-rate while maintaining approximately constant pulse peak power. This feature allows us to test different As_2Se_3 fibers with different damage thresholds at the same input peak power.

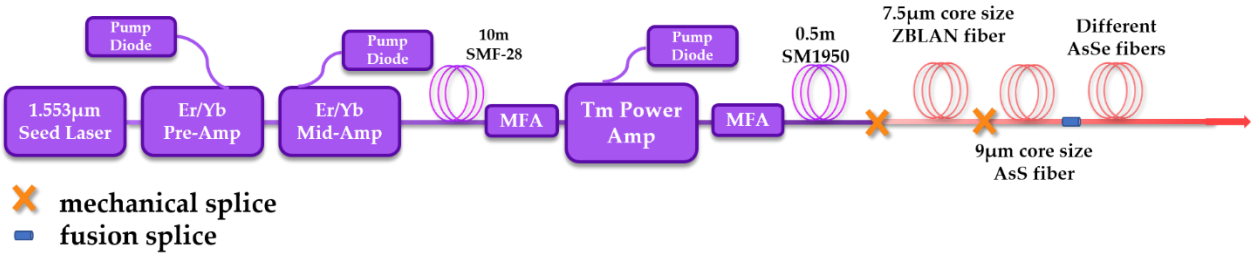


Figure 2-1 Schematic diagram of the SC Laser comprising the pump system and soft glass fiber cascade

The output from the pump system is then coupled into a soft glass fiber cascade of ZBLAN, As_2S_3 and As_2Se_3 fibers, where the dominant SC generation into the LWIR occurs. Within the fiber cascade, the first soft glass fiber is single mode ZBLAN fiber with NA of 0.26 and core diameter of 7.5µm (cut-off wavelength 2.54 µm). The ZBLAN fiber is followed by As_2S_3 fiber with a NA of 0.3 and core diameter of 9µm. The final piece in the fiber cascade is As_2Se_3 fiber, which is responsible for extending wavelength into the LWIR region. Multiple pieces of As_2Se_3 fibers are tested in the system to map out an optimum combination of As_2Se_3 fiber parameters, since the As_2Se_3 fiber has a strong influence on the output wavelength range, average power and beam quality.

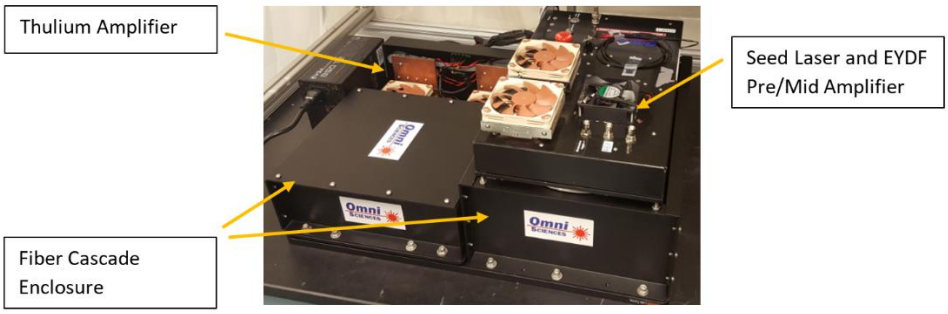


Figure 2-2 Packaged LWIR SC Laser prototype showing the frontend box, the thulium amplifier and the fiber cascade enclosure

2.3.2 Prototyping of the LWIR SC Laser

Based on the design of Fig. 2-1, we build both a tabletop system for proof of concept and a packaged prototype with integrated power supply and cooling for easy transportation and

operation. Figure 2 shows the packaged prototype with a form factor of 65cm×45cm×25cm. In Fig. 2-2, the box on the upper right corner contains the front end of the pump system, which includes the seed laser, EYDF pre-amp and mid-stage amp. The output of this box is connected to the upper left corner in Fig. 2-2, where the thulium power amp is located. The compartment underneath the front-end box stores the soft glass fiber cascade. This packaged prototype is entirely air-cooled with cooling fans on top of the pump diodes and gain fibers.

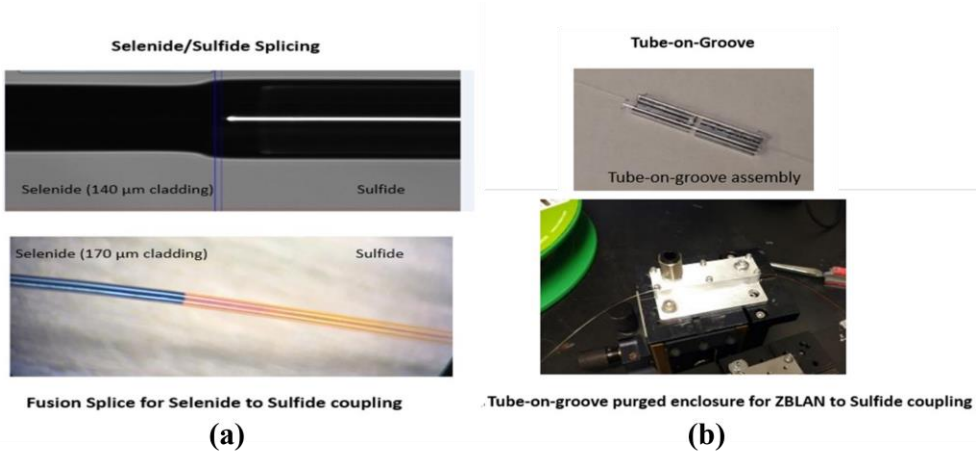


Figure 2-3(a) As2Se3 splice shown under splicer camera (top) and microscope (bottom) (b) "Tube on groove" mechanical splice: silica v-groove assembly (top) and nitrogen purged enclosure (bottom)

Coupling between different fibers within the soft glass fiber cascade is challenging due to the significantly different material properties between silica, ZBLAN and chalcogenide fibers. For example, silica glass has a glass transition temperature of ~1200°C, while ZBLAN has a glass transition temperature of ~265°C, making splices between these fibers difficult. Although a fusion splice between ZBLAN and silica has been reported [19], we found that our mechanical coupling provides fiber coupling with similar or even better robustness and efficiency than what we are able to achieve with our silica–ZBLAN splice. On the other hand, the material properties between As_2Se_3 and As_2S_3 are similar enough as glass transition temperature of As_2S_3 and

As_2Se_3 is ~185°C and ~170°C, respectively [20]. Therefore, we are able to fusion splice the sulfide and selenide fibers together with a Vytran filament-based splicer (Vytran LFS-4000) at low filament temperature setting (Fig.2-3 (a)), thereby eliminating any Fresnel reflections that result from the large material-air refractive index difference (17% on the As_2S_3-air interface and 21% on the As_2Se_3-air interface), improving throughput and minimizing reflection backward into the pump system. Compared to the butt-couple, the coupling efficiency improved by roughly 40%. The final splice has a ~60% coupling efficiency from As_2S_3 fiber to As_2Se_3 fiber.

Optical coupling between ZBLAN and As_2S_3 (sulfide) fiber is proving to be more difficult, and we have to date not been able to achieve reliable fusion splices between ZBLAN and As_2S_3 fibers. In our table-top system, we use three-axis XYZ-stages to couple between these two fiber types. To achieve a more compact and permanent coupling between these fibers, we have designed a special mechanical splice referred to as "tube-on-groove" to couple from the silica MFA pigtail to the ZBLAN fiber and from the ZBLAN fiber to the As_2S_3 fiber. In the "tube-on-groove" butt-couple, two fibers are first aligned and epoxied onto a pair of silicon v-grooves to ensure optimum coupling efficiency between the two fibers. We then fix the aligned v-grooves onto two sapphire rods for higher mechanical strength, as shown in the top of Fig. 2-3 (b). This assembly is further protected with a nitrogen purged enclosure to insulate the hydroscopic ZBLAN fiber from environmental water vapor contamination (bottom of Fig. 2-3 (b)). With this more compact type of "tube-on-groove" design, the coupling efficiency between fused silica MFA output to ZBLAN fiber is ~70%, and the coupling efficiency between ZBLAN and As_2S_3 fibers is ~60%.

2.3.3 Characterizing SC Fiber Parameters for Optimum LWIR SC Generation

To better understand the fiber parameters needed for optimum LWIR generation, six different As_2Se_3 fibers with varying NAs, core sizes and core/cladding compositions are tested. All the fibers are prepared through the double crucible method and their parameters as listed in Table 2-2.

Table 2-2 Summary of Related Fiber Parameter Used in This Study

Fiber Number	Core Size (μm)	NA	Core/Clad Material
1,2,3	10,12,14	0.76	$As_2Se_3/GeAs_2Se_5$
4	11	0.77	As_2Se_3/As_4SSe_5
5	10	1.4	As_2Se_3/As_2S_3
6	9	0.23	As_2Se_3

In section 2-4, these six fibers will be further divided into three groups (Table 2-3) to investigate the role of core size, NA and core/cladding composition in LWIR SC generation. To investigate the effects of core size, Group 1 consists of three As_2Se_3 fibers of same NA and core/cladding composition but with 10, 12 and 14μm core diameters, respectively. To investigate the effects of fiber core/cladding material, Group 2 consists of two fibers with similar NA and core size but different core/cladding composition. One fiber in Group 2 uses As_2Se_3/ $GeAs_2Se_5$ as core/cladding material, while the other uses As_2Se_3/ As_4SSe_5 as core/cladding material. Finally, we investigate the effects of fiber NA in fiber Group 3. Since changing the fiber NA also requires changing the core/cladding composition, we use fibers with different NA but core/cladding composition as similar as possible in this group. A tabularized fiber parameters are presented in Table 2-3.

Table 2-3 Three Groups of Fibers for SC Generation Performance Comparison

Fiber Group	Core Diameter (μm)	NA	Core/Clad Material	Varying Parameter
1	10/12/14	0.76	$As_2Se_3/GeAs_2Se_5$	Core Sizes
2	10	0.76/0.77	$As_2Se_3/GeAs_2Se_5$ $As_2Se_3/As4SSe_5$	Different Cladding Material
3	19/10/10	0.23/0.77/1.4	$As_2Se_3/GeAs_2Se_5$ As_2Se_3/As_4SSe_5 $As_2Se_3/As2S_3$	Different NA

Related parameters among selenide fibers such as loss, dispersion and mode field diameters are measured or calculated to assist our understanding of our experimental results. Fiber losses are measured with the cutback method on the 14μm core, 0.76 NA, $As_2Se_3/GeAs_2Se_5$ fiber, the 10μm core, 0.77 NA As_2Se_3/As_4SSe_5 fiber, and the 10μm core, 1.4 NA As_2Se_3/As_2S_3 fiber using a combination of a FTIR spectrometer and an external cavity quantum cascade laser source (Daylight Solutions, MN 31090- UT) in the wavelength ranges of 7.5-10.53μm. Figure 2-4 shows the loss measurement overlapped with typical As_2Se_3 fiber loss [21]. Our measurement shows that the background loss of the 0.76 NA As_2Se_3 fiber is <0.5dB/m, comparable to typical loss of As_2Se_3 fiber. Several absorption peaks are from impurities in the As_2Se_3 fiber. On the loss curve of 0.76 NA fiber, the ~9 μm and ~9.8 μm features corresponding to the As-O and Se-O absorption, while a higher Se-H absorption leads to the ~4.5 μm absorption peak [4]. In our measurement, the As-O peak is less visible, likely due to the limited signal-to-noise ratio limit of our measurement and the dominating Se-O absorption at a close by wavelength of 9.8 μm. Our loss measurement also shows that, starting from 8 μm, the 0.77 NA and 1.4 NA As_2Se_3/As_2S_3 fibers have significantly higher loss compared to the $As_2Se_3/GeAs_2Se_5$

fibers, which is likely from the sulfide content in the cladding. We will discuss this further in Section 2-6.

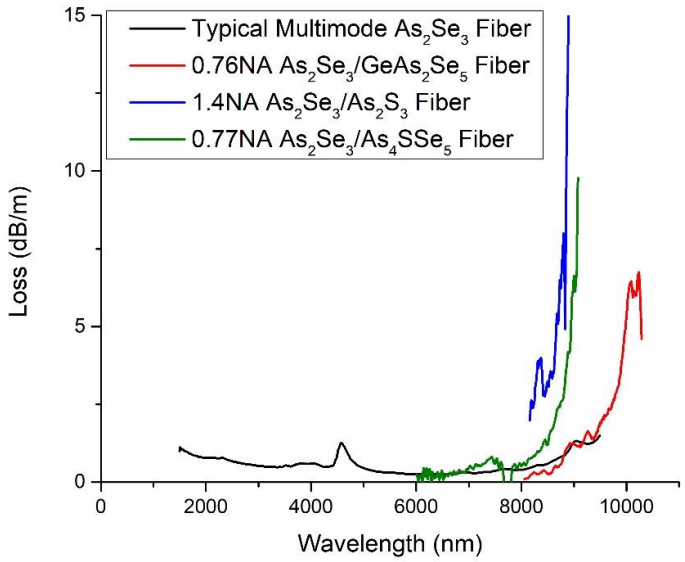


Figure 2-4 Loss of As2Se3 fibers showing As-O, Se-O, Se-H absorption band. 0.77NA As2Se3/As4SSe5 and 1.4NA As2Se3/As2S3 fibers also show much higher loss than 0.76NA As2Se3/ GeAs2Se5 fiber at longer wavelength

The dispersion and mode field diameters (MFD) of As_2Se_3 fibers are calculated through a 1-D Finite Element Method (FEM) based numerical solver described in [22]. The selenide fiber Sellemier equation used in the FEM solver is from [23] and the fiber manufacturers (Coractive and IRFlex). As an example, Figure 2-5 shows the dispersion and MFD of the selenide fibers used in this study. Selenide fibers with similar NA of ~0.76 share a similar zero dispersion wavelength of ~6 μm, and the fundamental modes are well confined within the fiber core region across the LWIR wavelength range.

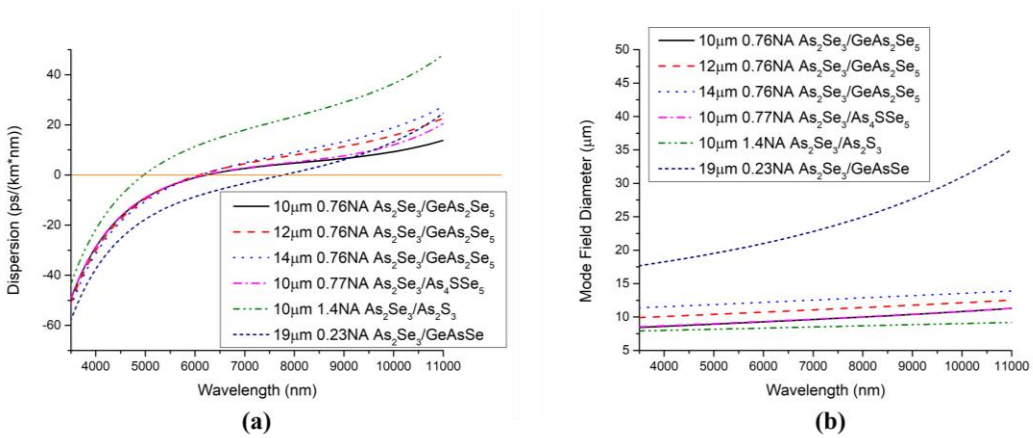


Figure 2-5 Dispersion (a) and MFD (b) of selenide fibers used in this study

To further explore the front section of the fiber cascade that generates SC wavelengths less than about 5.2 μm, we also developed a MWIR SC system. In addition to the 0.26NA 7.5μm core diameter ZBLAN fiber used in the thulium MOPA pumped fiber cascade (Fig. 2-1), we also test two different fluoride fibers with the EYDF mid-amplifier output to assess the influence of fiber MFD on SC generation. The two additional fluoride fibers are a 0.26NA, 9μm core diameter, indium fluoride (InF_3) fiber and a 0.3NA, 11μm core diameter, InF_3 fiber. InF_3 fibers are chosen because they have a transmission window up to 5.3μm, compared to 4.2μm in ZBLAN fiber. The InF_3 fibers are pumped with a system shown in Fig. 2-6, which consists of only the EYDF pre- and mid-stage amplifiers. The Tm power amp is not required in this set-up because the fluoride fibers do not exhibit nonlinear absorption at the pump wavelength of 1.553μm. Loss profiles of both fluoride fibers are provided by the fiber manufacturers. Figure 2-7 (a) shows that the background loss of the 0.26NA InF_3 fiber is consistently higher than the 0.3NA fiber with more distinctive absorption peaks at ~1.7μm, ~1.8μm and ~2.8μm. The peaks on both loss curves at ~3μm likely result from residual water content in the fiber. We also calculate the InF_3 fiber MFD using the same FEM used to model the As_2Se_3 fibers, which shows the MFD of the 0.26 NA fiber expands faster than the 0.3NA fiber as wavelength increases

(Figure 2-7 (b)). At 5.5μm wavelength, the MFD of the 0.26NA fiber is 16μm, compared with 13.5μm in the 0.3NA fiber. We think the MFD expansion in the 0.26NA fiber is influencing the long wavelength edge of the SC spectrum, which is further discussed in detail in the Section 2-6.

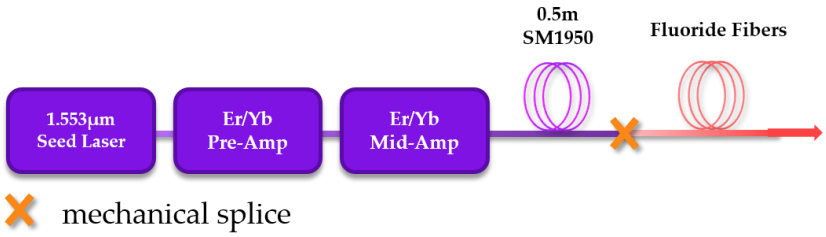


Figure 2-6 Schematic Diagram of Fluoride Fiber Pump System

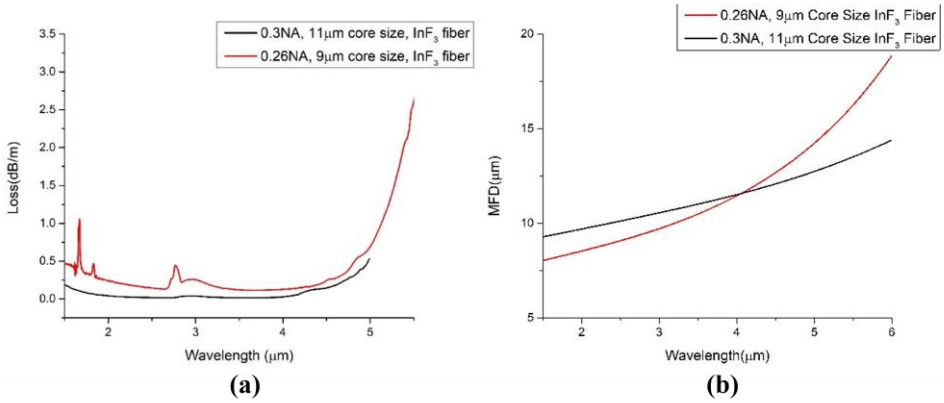


Figure 2-7 (a) Fiber loss comparison of the 0.3NA, 11μm core size and 0.26NA, 9μm core size. The absorption peaks on the 0.26NA fiber is likely from -OH absorption. (b) MFD comparison of the 0.3NA, 11μm core size and 0.26NA, 9μm core size InF3 fiber

Similar to our LWIR system, we build for the MWIR SC systems both a table-top system and a packaged prototype. The table-top system uses a three-axis XYZ stage to couple from silica fiber to fluoride fiber, while the packaged prototype system uses the "tube on groove" mechanical splice to couple between silica fiber and fluoride fiber. Without the need for thulium power amplifier and the soft glass fiber cascade, we manage to pack the ZBLAN or InF_3 SC fiber and the power supply into a single box similar to the front-end box of the LWIR prototype. The packaged prototype is shown in Fig. 2-8, which has a form factor of 43cm×25cm×9cm

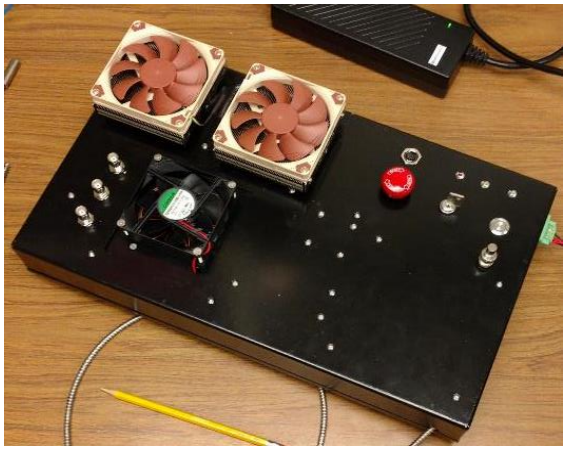


Figure 2-8 Packaged MWIR Prototype System with cooling fan and power supply integrated

To characterize the performance of our MWIR and LWIR SC light sources with different SC fibers, we measure the spectral output and beam quality of the SC output. The average output power is measured with a power meter (Coherent FieldMax) equipped with a thermo-electric measurement head. The wavelength expansion of each fiber is measured by coupling their output to a grating monochromator (Princeton Instruments, SP2150) with various long pass filters to remove higher order diffraction signals and is detected using a thermoelectrically cooled HgCdTe photoconductive detector (Vigo System S.A. PCI-4TE-13) amplified by a lock-in amplifier (Stanford Research Systems, SR865A). The spectrum below 3.5μm is acquired with a 300g/mm density grating blazed at 2μm, while the spectrum above 3.5μm is obtained with an 100g/mm density grating blazed at 5.2μm. The spectra are then corrected for grating efficiency, detector responsivity, and filter losses.

The output beam profile of the selenide fiber is imaged using an InSb-based camera (FLIR Systems, Inc. FLIR A6700sc) between wavelengths of 1-5μm and a micro-bolometer (BAE Systems, Inc. TWV-640) for wavelength passing 7.5μm. During the 1-5μm wavelength

range measurements, four additional spectral filters (1.1-2.6μm bandpass, 3.25-3.75μm bandpass, 3.3μm longpass and 4.5μm longpass) are used to measure the beam quality within narrower spectra ranges.

2.4 Experimental Results

2.4.1 Spectral and Power of Output of LWIR SC Laser

The 12μm core diameter $As_2Se_3/GeAs_2Se_5$ fiber provides highest power output, with 69.7mW (~17%) of the total power past wavelength of 7.5μm and spectral expansion to ~11.3μm. Figure 2-9 shows the spectral density of the output from the 12μm core size selenide fiber, with the spectrum extends from 1.6 to 11.3μm wavelength (measured 20 dB down from the edge of the plateau of the spectrum). From Fig. 2-5, the zero-dispersion wavelength of the $As_2Se_3/GeAs_2Se_5$ fiber is ~6μm. Before the zero-dispersion wavelength, the As_2Se_3 fiber is in normal dispersion regime and the resulting SC spectrum has some distinctive features which are likely from the material loss and cascaded Raman scattering in the sulfide fiber. Once past zero-dispersion wavelength, nonlinear processes such as soliton formation and self-frequency shifting start to dominate, resulting in a smooth spectrum that is ultimately limited by the fiber loss in the longer wavelength. At the 800kHz rep-rate and 33% power-amp duty cycle, the time average power output is 139mW, translating to 417mW when the power-amp is on. The on-time optical power within each spectral range is: 142.5mW (34% of total power) passing 4.6μm; 108.7mW (26% of total power) passing 6.3μm and 69.7mW passing 7.5μm (17% of total power).

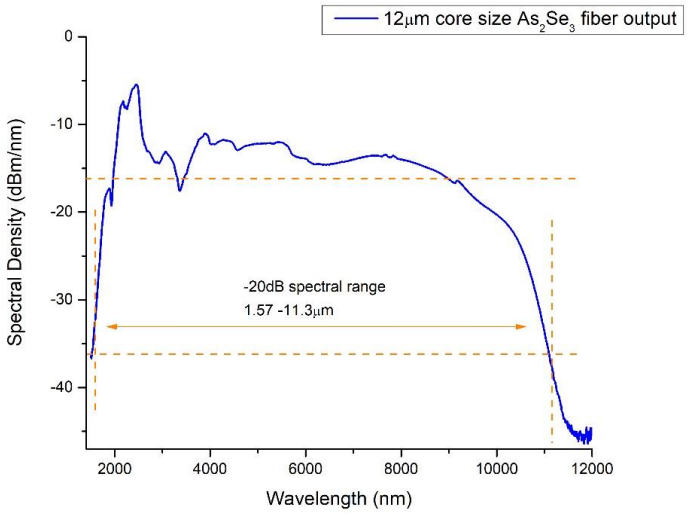


Figure 2-9 Measured laser output using a 12μm core size, 0.76NA, As2Se3/GeAs2Se5 fiber shows flat spectral expansion out to beyond 11μm.

The overall spectrum is generated sequentially in a cascade of soft glass fibers as shown in Fig. 2-10. First, in the ZBLAN fiber, the long wavelength edge was pushed to 4.5μm, which is limited by the absorption edge of ZBLAN fiber. Then, in the As_2S_3 fiber, the long wavelength edge further expands to ~6.5μm, which surpasses the zero-dispersion wavelength of the following As_2Se_3 fiber. Finally, in the $As_2Se_3/GeAs_2Se_5$ fiber, long wavelength edge is pushed to ~11.3μm.

The fiber cascade helps generating high power SC output in several ways: first, by using fibers with high damage threshold but narrower IR transparency windows such as silica and ZBLAN, we eliminate the need of coupling high peak power pulses directly into sulfide and selenide fibers that have lower damage threshold. Secondly, by separating SC generation into three separate fibers, we ensure that the signal coupled into each soft glass fiber has the highest peak power that can be handled by that soft glass fiber while maintaining the broadest spectrum possible from the previous SC fiber. Finally, cascading the soft glass fibers allow us to pump the following soft glass fiber either close or past the zero-dispersion wavelength, which would

improve the SC generation efficiency due to the soliton dynamics in the anomalous dispersion regime [24].

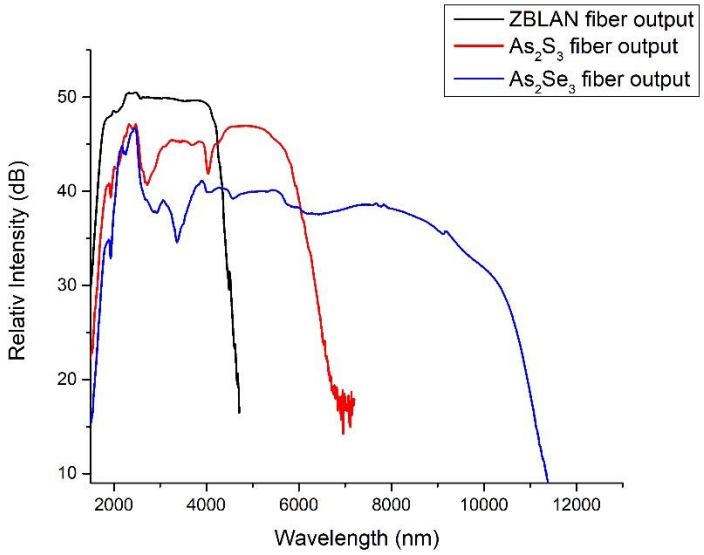


Figure 2-10 Typical SC spectra for 6.5m, 7.5µm core size ZBLAN, 4m, 9µm core size As2S3, and 4m, 12µm core size As2Se3/GeAs2Se5 fibers. Power steps down and SC edge increases in successive cascade fibers

To fully utilize the transparency window of our As_2Se_3 fiber, we use a shorter 2.5m, 10 µm core size as our final stage SC fiber. The shorter fiber length is chosen because the 10 µm diameter fiber is more nonlinear than the 12 µm diameter fiber and therefore requires less fiber length to generate similar spectral expansion. If the selenide fiber is unnecessarily long, too much light will be absorbed at longer wavelength, reducing the SC generation efficiency. We also increase input peak power to the soft glass fiber cascade to pump our selenide fiber with wider and higher power pumping SC spectrum (i.e., output SC spectrum of sulfide fiber). Figure 2-11 shows the SC spectrum generated in 2.5m $As_2Se_3/GeAs_2Se_5$ fiber.

The broadest spectrum is generated with the -20dB wavelength ranging from 1.6 µm to 12 µm. Compared to Fig.2-9, after the initial drop of intensity passing 10 µm, a second plateau is generated and further extend the wavelength range to 12 µm. We attribute this second plateau to the Se-O absorption peak in the As_2Se_3 fiber. In terms of output power, the on-time average

power is 108mW, with 22.5mW passing 7.5µm (21% of total power). The cause of the lower optical power compared to the output 12 µm core diameter fiber is that for the 10 µm core fiber, the MOPA pump system is only operating at 300kHz instead of 800kHz to avoid damage to the As_2Se_3 fiber. We believe with proper protection to the chalcogenide fiber tip, we could achieve comparable power as in the 12 µm core diameter fiber from the 10 µm core fiber.

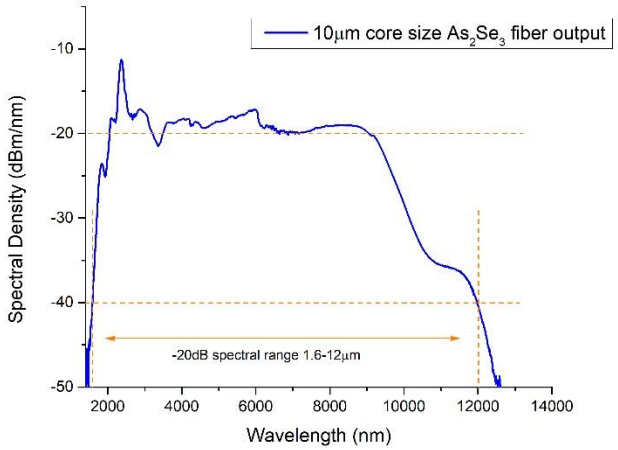


Figure 2-11 SC spectrum generated in 2.5m of 10µm core size As2Se3 fiber, showing a second plateau extending the wavelength edge to ~12 µm

Figure 2-12 shows the evolution of SC spectrum out of each soft glass fiber with in the 10µm core size selenide fiber cascade. At 300kHz rep-rate, we are able to pump the ZBLAN fiber and sequentially the sulfide fiber with higher peak power (~15% higher), leading to better expansion of spectrum in the As_2S_3 fiber, where the long wavelength edge extends to ~7.5µm compared to ~6.5µm in Fig. 2-10. To our knowledge, this is among the broadest expansion so far reported out of the As_2S_3 fiber.

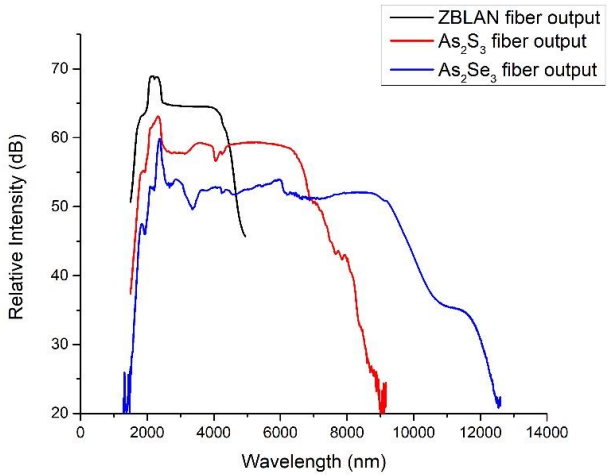


Figure 2-12 Output spectra for 9m, 7.5µm core size ZBLAN, 4m, 9µm core size As2S3, and 2.5m, 10µm core size selenide fibers

In terms of the stability of our SC sources, we measure the time-average power fluctuation of 0.49% (defined as standard deviation/mean). Such noise could potentially be mitigated by injecting seed light of correct wavelength into the SC laser as well as the feedback control of the MOPA pump system.

2.4.2 Output Beam Profile of LWIR SC Laser

We then characterize the beam quality of the SC laser output by measuring the beam profile and divergence angle in different spectral ranges by filtering the fiber output with various spectral filters. The output from the 12 µm core As2Se3 is used due to the higher output power. During the beam measurement, a roughened aluminum plate is used as the target for the wavelength range of 1-5µm, and tar covered cardboard is used as the target for the wavelength range of 7.5-11µm. The output fiber tip is placed 95mm from the target for 1-5µm measurement and is reduced to 51mm for 7.5-11µm wavelength range measurement. The shorter distance used at the longer wavelengths is to compensate for the lower optical power within the 7.5-11µm wavelength range.

Figures 2-13(a)-(f) show images of the beam profiles in different spectral ranges. The left side of each figure shows the beam captured by the camera, while the right side shows the beam cross section along the vertical direction. Through the entire wavelength range, the output beam is tightly confined and shows a nice Gaussian-like shape. The measured beam quality appears nosier in 3.25-3.75μm and 4.5-5 μm because of the lower optical power within the narrow wavelength range. The captured beams also look slightly asymmetrical in the horizontal direction because the camera is pointed towards the target screen at an angle. The single spatial mode output from the SC light source provides a near diffraction limited beam for remote sensing applications.

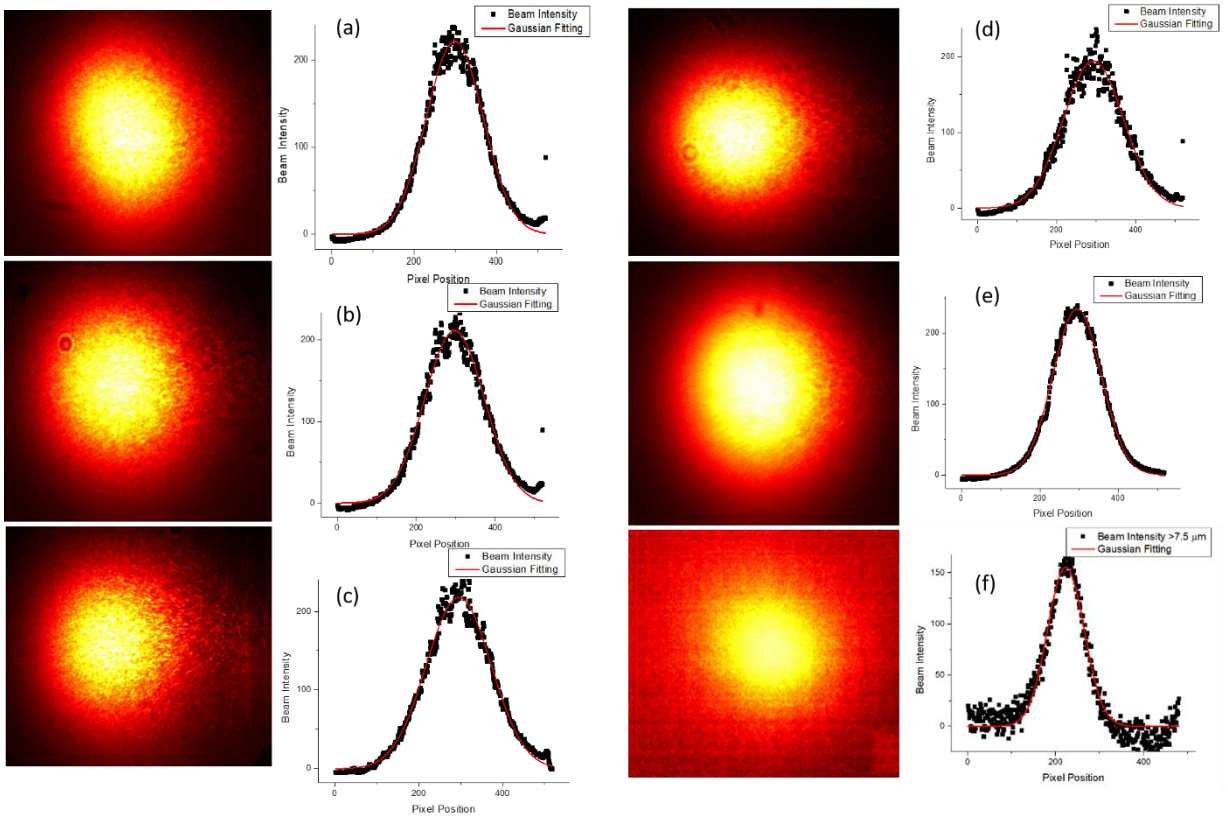


Figure 2-13 Output beam profile and cross section between (a) 1.1-2.6μm (b) 3.25-3.75μm (c) 4.5-5μm (d) 3.3-5μm (e) 1-5μm (f) 7.5-11μm

The divergence and NA of the beam is derived through:

$$\boldsymbol{\theta_{measure} = arctan(r_{beam}/d)} \quad [2\text{-}1]$$

$$\boldsymbol{NA_{measure} = sin(\theta_{measure})} \quad [2\text{-}2]$$

where r_{beam} is the radius of the beam, measured as the $1/e^2$ radius from the image, and d is the distance from fiber tip to the target. As is shown in Table 2-4, the beam divergence increases with increasing wavelength. As described further in the discussion section, we believe this is caused by MFD being tightly confined across the entire wavelength range.

Table 2-4 Measured beam radius and calculated NA within each spectral range

Wavelength	Measured Beam Radius	Measured Beam NA
1.1-2.6μm	25mm at 95mm	0.25
3.25-3.75μm	27mm at 95mm	0.28
3.3-5μm	27.5mm at 95mm	0.28
4.5-5μm	27.5mm at 95mm	0.28
1-5μm	26mm at 95mm	0.28
7.5-11μm	27.2mm at 51mm	0.47

2.4.1 Effects of SC Fiber Parameter on SC Generation

To investigate the effects of different fiber parameters on the SC generation, we also compare the SC generation performance within different fiber groups (Fig.2-14, Fig.2-15). For consistency during the comparisons, the MOPA system is running at 100kHz with 100% duty cycle and all selenide fibers tested are butt-coupled to the sulfide fiber. Also, since we are interested in the SC expansion into longer wavelength, we only measure the spectrum past 7μm, i.e., wavelength components that is generated in the As_2Se_3 fibers. The spectrums are plotted on a relative decibel scale, but each curve is calibrated relative to other curves within the same figures (e.g., same spectrometer setting/acquisition setting, etc.).

Fig. 2-14 (a) shows the comparison of group 1 fibers through which we study the influence of different core sizes. We compare the long wavelength edge of the SC spectrum generated by selenide fiber of different core sizes, but with the same NA and core/cladding composition. The -20dB wavelength for 14/12/10μm core size fibers are 10.3μm, 11.3μm and 11.6μm, respectively. Compared with spectrums generated in 10 and 14μm core size fibers, the long wavelength edge of the SC spectrum from the 12μm core size fiber is slightly shorter than the one from the 10μm core size fiber, but the spectrum is smoother and with much fewer features. We believe this is because 12μm core size represents a good balance between the MFD confinement in the longer wavelengths and the nonlinearity in the shorter wavelengths.

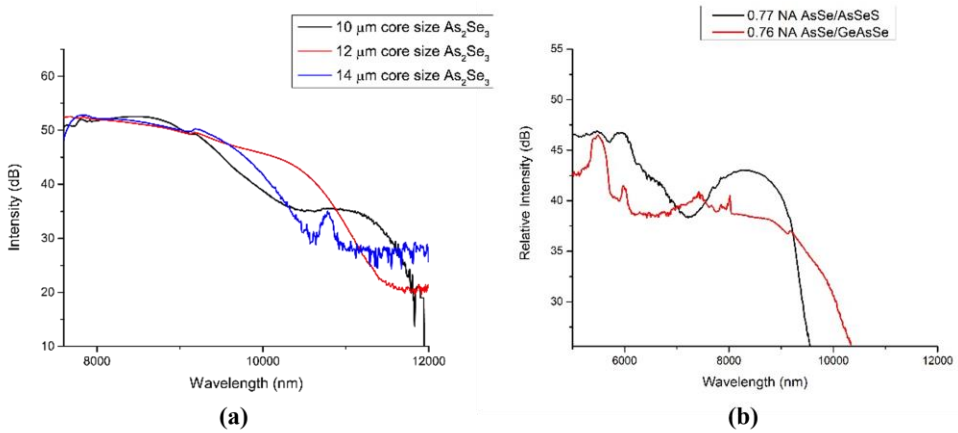


Figure 2-14 SC Long wavelength edge of (a) different core size As2Se3 fiber. (b) different As2Se3 fiber core/cladding composition

In fiber group 2, we compare fiber with similar core size and NA, but different core/cladding composition, as shown in Fig.2-14 (b). Both spectra are smooth, and the -20dB wavelength is 9.7μm for 0.77NA As_2Se_3/As_4SSe_5 fiber while the -20dB wavelength is 10.3μm for 0.76NA $As_2Se_3/GeAs_2Se_5$ fiber. We attribute this difference to the extra loss introduced by sulfide cladding, which we further discuss in the next section.

In fiber group 3, we compare fibers with similar core/cladding composition, but significantly different NA. As is shown in Fig.2-15 (a), even though all three spectra are

relatively smooth, we see considerably different SC generation performance among different fibers. For the 0.77NA fiber, the -20dB wavelength is 10.1μm, while for the 1.4NA fiber, it is only 8.9μm. The 0.23NA fiber has the shortest long-wavelength SC edge, with its -20dB wavelength at ~7.1μm. For the 1.4 NA fiber, besides the extra loss introduced by the As_2S_3 cladding, we also attribute this difference to the MDF being small at shorter wavelength, resulting in poor power coupling between As_2S_3 fiber and As_2Se_3 fiber; on the other hand, the MDF is too large for the 0.23 NA fiber at longer wavelength, leading to excessive cladding-induced loss and reduced nonlinearity from the large mode size.

As further evidence of MFD's effect on SC generation, we also compare the results between different InF_3 fibers in the MWIR regime. Between different InF_3 fibers, we also focus on the long wavelength edge of the generated SC spectrum. For example, Fig. 2-15 (b) shows that the -20dB wavelength is ~4.5μm for 0.26NA fluoride fiber, while the -20dB wavelength is ~5.2μm for the 0.3NA fiber. Both spectra are relatively smooth and featureless since the seed wavelength is very close to the zero-dispersion wavelength of the fluoride fibers; moreover, there are no prominent absorption peaks in the InF_3 fibers over this wavelength range. The background absorption is very similar in both fluoride fibers, and the preceding silica fiber has a smaller core diameter than both fluoride fibers (7 μm core versus 9 μm and 11 μm), leading to comparable coupling efficiency in both fluoride fibers. We believe that the ~0.7 μm difference in wavelength expansion arises from the MFD expanding much faster in the 0.26 NA than the 0.3 NA fiber (Fig. 2-7(b)). We will also discuss this in more detail in Section 2-6.

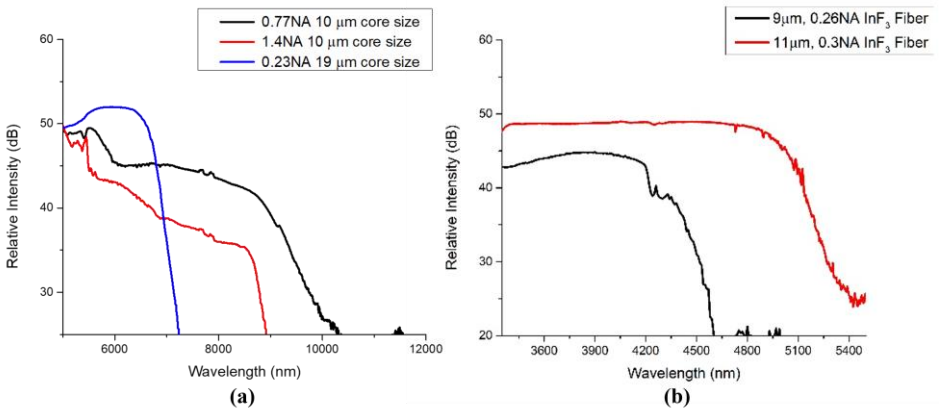


Figure 2-15 SC Long wavelength edge of (a) different As2Se3 fiber NA. (b) different InF3 fiber NA

2.5 Modelling of SC Generation

To help predict and explain the effects of different fiber parameters on the SC generation, we numerically model the SC generation process in soft glass fibers. The simulation of SC generation in cascaded soft glass fibers was first reported by Kubat et al. and is helpful in understanding the physical process behind the SC generation within each soft glass fiber [25]. The modelling of SC generation is done by numerically solving the generalized nonlinear Schrödinger equation [26]:

$$\frac{\partial A}{\partial z} = (\hat{D} + \hat{N})A \qquad [2\text{-}3]$$

In equation [2-3] dispersion term is:

$$\hat{D} = -\frac{i}{2}\beta_2\frac{\partial^2 A}{\partial t^2} + \frac{1}{6}\beta_3\frac{\partial^3 A}{\partial t^3} + \frac{i}{24}\beta_4\frac{\partial^4 A}{\partial t^4} - \frac{\alpha}{2} \qquad [2\text{-}4]$$

where A is the envelope of the input optical pulse, β_i is the *i*th order dispersion of the fiber, and α is the fiber loss. The nonlinear term in equation [2-3] is:

$$\hat{N} = i\gamma(\omega) * (1 + \frac{1}{\omega_0}\frac{\partial}{\partial t}) \int_{-\infty}^{+\infty}[(1 - f_R)\delta(t) + f_R h_R(t)] * \left|A(z, t - t')\right|^2 dt' \qquad [2\text{-}5]$$

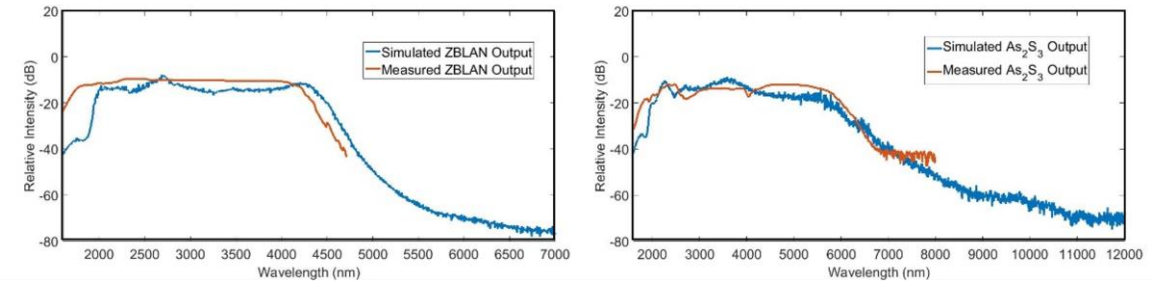
where $\Upsilon(\omega)$ is the wavelength dependent nonlinear coefficient of the fiber, ω_0 is the central angular frequency, f_R is the Raman contribution in the nonlinear process and $h_R(t)$ is the time domain Raman response.

Because the broad bandwidth SC generation covers several octaves of light, it is necessary to use the full form of the generalized nonlinear Schrödinger equation, where the nonlinearities considered include four-wave mixing, self-phase modulation and Raman scattering. The generalized nonlinear Schrödinger equation is solved through a modified version of the nonlinear optics MATLAB toolbox [27]. In our simulation, the number of grid points is 2^{18}, the time step is 2.9 fs, and a time window of 0.76 ns. Moreover, due to the nonlinearity difference between soft glass fibers, we use different propagation steps for each soft glass fiber to achieve balance between computation time and accuracy. In the least nonlinear ZBLAN/InF3 fiber, the step size is 200μm, while in the more nonlinear As_2S_3 and As_2Se_3 fibers, the step size is 50μm and 10μm, respectively. Also, in the simulator, only the fundamental spatial mode is considered and a 15ps Gaussian pulse at 1550nm with 15kW peak power is used as the input pulse to reduce the computation time. We choose the 15ps pulse instead of the actual 1.1ns pulse because it has been shown that 15ps pulse is sufficient to represent most SC generation effects seen with the broader 1.1 ns pulse [24,26]. In the Tm amplifier, the absorption of input SC spectrum by the Tm ion is treated as fiber loss, while the gain from the Tm ions is treated as negative loss in the fiber. This is a relatively crude approximation to a real Tm amplifier, but the output spectrum of such approximation agrees reasonably well with experimental results [28].

The simulator is tested by comparing the experimental and simulated SC generation results at each soft glass fiber output. For ZBLAN/InF_3/As_2S_3 fibers, fiber losses are obtained from the manufactures. For the As_2Se_3 fibers, we used our measured results shown in Fig. 2-4. Fiber dispersions and MFDs are calculated through a MFD solver, as described in the experiment setup section. The nonlinear and Raman gain coefficients are obtained from published studies [3,29-31]. Note that the simulations represent a single shot of the SC generation, while the

experiments are an ensemble average over many pulses. To mimic the real ensemble of multiple pulses, we average the simulated spectrum within a 10 nm bandwidth.

Figure 2-16 (a) shows the comparison between the experimentally measured spectrum and simulated spectrum of our 7.5μm core diameter, 0.26NA ZBLAN fiber. The simulation result agrees with the experiment result in terms of the overall shape and smoothness of the spectrum. Our simulated data shows a longer wavelength edge compared with our experimental result (4.6μm vs. 4.4μm). This discrepancy is likely caused by a higher long wavelength loss in the actual ZBLAN fiber used in the experiment. We next model the SC generation in the next step of the fiber cascade by coupling the simulated output of the ZBLAN fiber into the 9μm core diameter, 0.3NA As_2S_3 fiber, as shown in Fig. 2-16 (b). Between each fiber cascade, the signal is attenuated based on the coupling efficiency measured experimentally. There is again reasonable agreement between the experiment and simulation results, except for the dip at ~4.1μm. This 4.1μm dip in the experimental data may arise from a sharp S-H absorption peak in the fiber.



(a) **(b)**

Figure 2-16 Comparison between simulated (blue) and experimental SC spectrum (red) in (a) ZBLAN fiber (b) in As2S3 fiber

Finally, we model the SC generation in the As_2Se_3 fiber by coupling it to the simulated output from As_2S_3 fiber. As an example, we show simulations using the As_2Se_3 with 10μm core diameter, 0.76NA $As_2Se_3/GeAs_2Se_5$ fiber, which produces the broadest SC generation result. Figure 2-17 shows the simulated output from a 2.5m piece of the As_2Se_3 fiber, and our model matches reasonably well with the experimental results. The peaks in the simulated spectrum is

likely caused by more significant contribution from the Raman effect. The long wavelength edge in our simulated result drops more quickly than the actual SC spectrum, which we believe may be due to loss curve used in the simulator being steeper at the longer wavelength than the actual loss in the fiber. Also, since the refractive index and nonlinear coefficients of the actual fiber are unlikely to be identical to the ones used in the simulation, we also see that our simulated result lacks some fine features seen in the experiments.

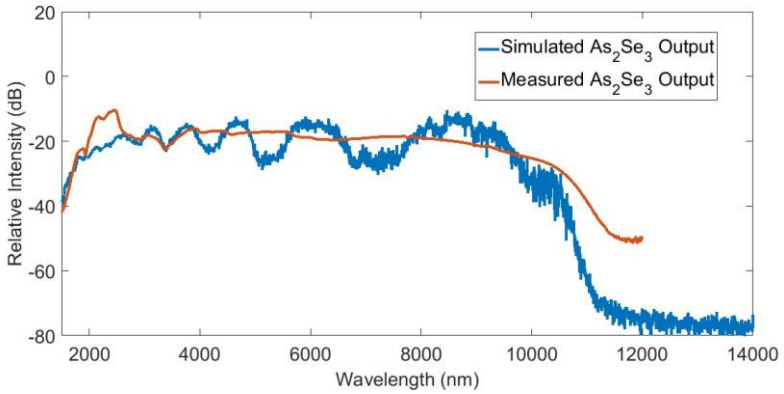


Figure 2-17 Comparison between simulated (blue) and experimentally measured (red) SC spectrum in As2Se3/GeAs2Se5 12μm core diameter fiber

2.6 Discussion

In this section we will review and explain some of the experimental results, and this understanding may provide directions for further improvements in the SC system. We first discuss the LWIR laser beam quality, and then the influence of the fiber parameters on the long wavelength edge of the SC spectrum is described. Some of the fiber parameters of interest include the core/cladding composition, numerical aperture, and core diameter. The importance of these fiber parameters to the long wavelength SC edge can be explained by their influence on the fiber loss and mode properties.

2.6.1 Beam Quality

As shown in Table 2-4, the output beam divergence also increases from 0.25 NA in the 1.1-2.6μm region to 0.47 NA in the 7.5-11.3μm region as the wavelength increases. We attribute the change in NA to the wavelength dependent divergence expected of a Gaussian beam. For an ideal Gaussian beam, the divergence angle and NA can be calculated as:

$$\boldsymbol{\theta_{ideal} = arctan(\lambda/(\pi \times w_0))} \quad [2\text{-}6]$$

$$\boldsymbol{NA_{ideal} = sin(\theta_{ideal})} \quad [2\text{-}7]$$

where θ_{ideal} is the divergence half angle, λ is the wavelength and w_0 is the mode field radius of the beam. The MFD of the 0.76 NA, 12μm core As_2Se_3 fiber is calculated using FEM and is shown in Figure 2-5. In our As_2Se_3 fiber, the MFD of fundamental mode is well confined across a wide wavelength range due to the ultra-high NA of the fiber, which results in a significant wavelength dependence of the beam divergence.

From the measured and theoretical beam divergence, we calculate the beam M^2 number (defined as the ratio between measured beam divergence and ideal beam divergence) at the average wavelength of three typical spectral ranges. As is seen in Table 2-5, the output beam is near diffraction limited beyond 3 μm and shows an improved beam quality (smaller M^2) at the longer wavelength. This result is somewhat unexpected as the single-mode cutoff wavelength of the 0.76 NA fiber is ~12 μm. The underlying reason for the single-mode output could be twofold: first, the SC expansion has to happen in the fundamental mode because of the high nonlinearity. Second, in the 0.76 NA fiber, the differences of propagation constants among the first several higher-order spatial modes are relatively large, and several meters of fibers are not long enough for energy to be effectively coupled into these higher-order modes [32]. This single spatial mode output from the SC light source would make it a very useful tool for the remote sensing applications where projection of the optical beam to long distance is needed.

Table 2-5 Beam characteristic at different spectral ranges

Wavelength	Beam Waist	Measured Divergence (NA)	Ideal Divergence (NA)	M^2
1.1-2.6μm	9.3μm	14.5º (0.25)	7.5 º (0.13)	1.7
3.25-3.75μm	9.87 μm	16.3º (0.28)	12.7º (0.22)	1.3
7.5-11.3μm	12μm	28º (0.47)	24.2º (0.41)	1.2

2.6.2 Effects of Core/Cladding Composition

By comparing the SC spectrum generated by As_2Se_3/As_4SSe_5 core/cladding composition and $As_2Se_3/GeAs_2Se_5$ core/cladding composition (Fig.2-14(b)), we find that fibers with $GeAs_2Se_5$ as cladding material consistently generate SC spectra that expand to longer wavelengths compared with fibers with As_4SSe_5 cladding. We attribute this difference in the long wavelength edge to the loss introduced by the sulfide content in the cladding. Although the fundamental mode in the fiber is tightly confined in the core region in ultra-high NA fibers, the tail will still extend into the cladding region of the fiber. As studied in the evanescent wave spectroscopy [33], cladding loss will contribute to significant power loss even if the beam is well confined in the core. Furthermore, as the wavelength increases, the MFD expands more into the fiber cladding, resulting in higher loss at the longer wavelengths. The extra loss in the cladding can be estimated as:

$$\textbf{Extra Loss} = -\textbf{10log}(\textbf{exp}(\mathbf{r}\gamma\mathbf{L})) \quad (8)$$

where **r** is the percentage of power in the fiber cladding, $\boldsymbol{\gamma}$ is the material loss in the cladding, and **L** is the length of the fiber.

The percentage of power that penetrates into the fiber cladding grows quickly as wavelength increases. In the 0.77 NA As_2Se_3/As_4SSe_5 core/cladding fiber, the calculated power

distribution in the core/cladding region is shown in Table 2-6, where the percentage of power in the fiber cladding is calculated through the Lumerical Mode software [34]. When the wavelength increases, more power penetrates into the fiber cladding region. As the wavelength goes from 8.5μm to 11μm, the percentage of power within cladding increases from 11% to 21%.

In our As_2Se_3/As_4SSe_5 fiber, As_2S_3 contribute to 17% of the cladding composition and by combining the field distribution and sulfide loss at the longer wavelengths from [20], we calculate the extra loss introduced by the sulfide content in fiber cladding. Table 2-6 shows the estimated extra loss introduced by the sulfide doped cladding in our 0.77NA, As_2Se_3/As_4SSe_5 fiber.

Table 2-6 Estimated Loss due to Cladding Absorption in 0.77NA As_2Se_3/As_4SSe_5 Fiber

Wavelength (μm)	**As_2Se_3 Loss (dB/m)**	**Percentage of power in cladding**	**Extra cladding loss (dB/m)**	**Total Loss (dB/m)**	**Measured Loss (dB/m)**
8.5	0.3	11.13%	2.13	2.43	1.4
9	1.31	13.53%	5.81	7.12	6.9
9.74	2.7	16.32%	12.17	14.87	>10
11	>8	21.61%	9.06	>17.06	>10

Table 2-6 also shows that at the longer wavelengths, the loss introduced by the cladding dominates the total fiber loss and increases rapidly as wavelength increases; therefore, the cladding loss may prevent expansion of SC spectrum into the longer wavelengths. Thus, to effectively generate SC in LWIR beyond ~10μm, both the core and cladding need to have low loss in the target wavelength, which is especially true when the pump source is a low peak power MOPA system where longer SC fibers are needed. This phenomenon is also verified through our simulator. In our simulator, we replace the 0.76NA, 12 μm core size $As_2Se_3/GeAs_2Se_5$ fiber with

the 0.77NA, 10 μm core size As_2Se_3/As_4SSe_5 fiber. Figure 2-18 shows the long wavelength edge of the simulated SC when the measured loss of the 0.77NA As_2Se_3/As_4SSe_5 is used. The long wavelength edge of the generated SC spectrum is ~9.9μm, comparable to our experimental result of 9.74μm in Fig.2-14(b).

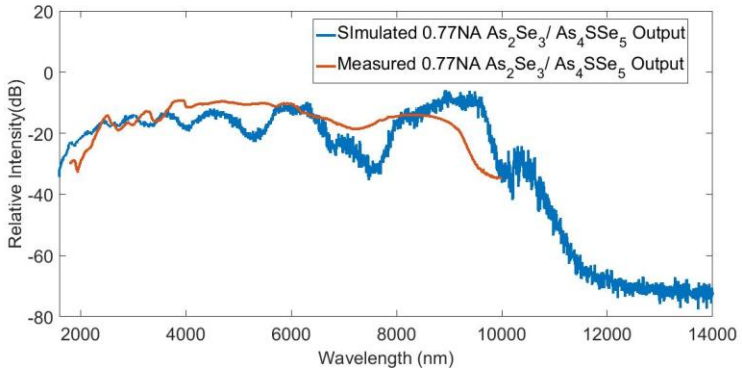


Figure 2-18 Simulated SC spectrum compared to experimentally measured SC spectrum in the 0.77NA, As_2Se_3/As_4SSe_5 fiber

To further demonstrate contribution of fiber cladding to the overall loss of the fiber, we prepare and measure the loss of three As_2Se_3/As_2S_3 fiber with 10 μm, 16 μm and 60 μm core diameter respectively. With the same cut-back method we used in Section 2-3, the measured losses are shown in Fig.2-19. As the core diameter expands, the fundamental mode is more confined in the fiber core and is therefore less affected by the loss of the sulfide cladding. The most well confined 60 μm core fiber, the loss at 10 μm is only ~4.5dB/m, comparable to the loss of the $As_2Se_3/GeAs_2Se_5$ fiber. However, when the core diameter reduces to 16 μm and further to 10 μm, the loss at longer wavelength grows quickly and eventually in the 10 μm core diameter fiber, the loss is >10dB/m at wavelength of just 9 μm, which agrees with our SC generation result.

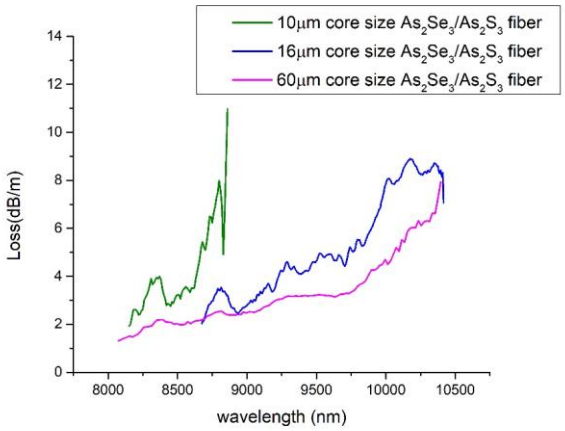


Figure 2-19 Measured loss in As2Se3/As2S3 core fibers with different core size

2.6.3 Effects of NA

Another finding from the experiments is that fiber NA also affects the SC generation performance (Fig.2-15), where either too high or too low an NA value will prevent SC from expanding into longer wavelengths. When the NA is too high, a number of problems arise: (a) at the shorter wavelengths, there are too many spatial modes in the fiber; and (b) the MFD of the fundamental mode will become too small to efficiently couple light from sulfide fiber into the fundamental mode of the selenide fiber. As an example, in our 1.4 NA As_2Se_3 fiber, the MFD of the fundamental mode is only 7.5 μm at 5 μm wavelength, compared with the 12 μm MFD of our As_2S_3 fiber at the same wavelength, resulting in a high coupling loss. In addition, the differences between the propagation constants of adjacent spatial modes in the 1.4 NA fiber is much smaller than the difference in the 0.76NA fiber, making it easier for power to be coupled to higher order mode [32]. On the other hand, when the NA is too low, at longer wavelengths the MFD expands quickly into the lossy fiber cladding, preventing further spectral expansion. For example, the MFD is 31 μm in the 0.23 NA selenide fiber at 10 μm, which is significantly larger than the physical core size of the fiber. Besides the excessive cladding loss, large MFD also leads to a low fiber nonlinearity, preventing SC expansion into longer wavelength. Therefore, it seems

that ~0.76NA is a more optimized NA value because in the 0.76NA fiber, from wavelengths between 5 μm to 10 μm, the fiber MFD only changes from 10.3 μm to 12 μm, enabling both efficient coupling from sulfide fiber as well as tight mode field confinement at longer wavelengths.

The influence of NA is further verified by our fluoride fiber results (Fig.2-15(b)) in the MWIR SC system. For example, at wavelength of 5.5μm, the MFD is ~16μm in the 9μm core diameter, 0.26NA InF_3 fiber; compared to 13.5μm in the 11μm core diameter, 0.3NA fiber. Even though the physical core size of the 0.26NA InF_3 fiber is smaller than the 0.3NA fiber, the effective mode area is 46% larger than the effective mode area in the 0.3NA InF_3 fiber, resulting in poorer SC expansion toward longer wavelengths. Thus, to effectively generate SC in LWIR, we need a fiber with optimized NA which behaves like a "few mode" fiber that maintains a stable MFD of the fundamental mode across the entire wavelength range of interest.

2.7 Chapter Summary

In this chapter, we investigate the effects of different fiber parameters on SC generation in LWIR with a nanosecond thulium MOPA configuration. We generate 417mW SC covering 1.57μm to ~11.3μm through a cascade of ~6m 0.26NA, 7.5μm core diameter ZBLAN fiber, 4m of 0.3NA, 9μm core diameter As_2S_3 fiber and 4m of 0.76NA, 12μm core diameter As_2Se_3/$GeAs_2Se_5$ fiber. To fully utilize the transparency window of the As_2Se_3 material, we also generate wider SC spectrum covering 1.6μm to ~12μm but with an output power of 108mW with concatenated 9m 0.26NA, 7.5μm core diameter ZBLAN fiber, 4m of 0.3NA, 9μm core diameter As_2S_3 fiber and 2.5m of 0.76NA, 10μm core diameter As_2Se_3/$GeAs_2Se_5$ fiber.

Our beam characterization reveals a single spatial mode output with near diffraction beam quality across the entire wavelength range despite the wavelength dependence of the beam

NA. The wavelength dependence of NA is likely due to the beam divergence of the gaussian beam being a function of wavelength, but the fundamental mode MFD is well confined in the ultra-high-NA selenide fiber. We also investigate the influence of different As_2Se_3 fiber parameters on the long wavelength of the generated SC spectrum.

We find that selenide fiber core/cladding material, NA and core size all have effects on SC generation performance in the LWIR spectral region. Lossy cladding composition can affect the long wavelength edge of the SC spectrum by introducing extra loss to the As_2Se_3 fiber. For example, in our 0.77NA As_2Se_3/As_4SSe_5 fiber, even though only 17% of sulfide is added to the cladding, it introduced ~12dB/m extra loss to the fiber at 9.74μm, limiting the SC expansion at longer wavelength. NA's effects on the SC are twofold since NA affects the MFD as well as the number of modes in the selenide fiber. While a too high NA would make the MFD too small at shorter wavelengths, making optical coupling into the selenide fiber more difficult, a too low NA will not be able to confine the fiber mode within the core region at longer wavelength, causing extra loss and lower the fiber nonlinearity.

Moreover, as we can see from the SC generation result in the 10 and 12 μm core diameter $As_2Se_3/GeAs_2Se_5$ fibers, core size plays a subtler effect on the SC generation since smaller core size improves the SC generation efficiency by increasing fiber nonlinearity but at the same time lowers the damage threshold, potentially limiting the total SC output power. Our results suggest that selenide fiber with ~0.76NA and low loss $GeAs_2Se_5$ as cladding material offers a good compromise among these fiber parameters, enabling high-power SC generation covering both LWIR and MWIR spectral region when pumped by an all-fiber MOPA configuration.

Reference

[1] J. Nallala, G. R. Lloyd, N. Shepherd, and N. Stone, "High-resolution FTIR imaging of colon tissues for elucidation of individual cellular and histopathological features," Analyst 141, 630–639 (2016).

[2] M. N. Islam, M. J. Freeman, L. M. Peterson, K. Ke, A. Ifarraguerri,C. Bailey, F. Baxley, M. Wager, A. Absi, J. Leonard, H. Baker, and M. Rucci, "Field tests for round-trip imaging at a 1.4 km distance with change detection and ranging using a short-wave infrared supercontinuum laser," Appl. Opt. 55, 1584–1602 (2016).

[3] R. R. Gattass, L. B. Shaw, V. Nguyen, P. Pureza, I. D. Aggarwal, and J. S. Sanghera, "All-fiber chalcogenide-based mid-infrared supercontinuum source," Opt. Fiber Technol. 18, 345–348 (2012).

[4] C. R. Petersen, U. Møller, I. Kubat, B. Zhou, S. Dupont, J. Ramsay,T. Benson, S. Sujecki, N. Abdel-Moneim, Z. Tang, D. Furniss, A. Seddon, and O. Bang, "Mid-infrared supercontinuum covering the 1.4-13.3 μm molecular fingerprint region using ultra-high NA chalcogenide step-index fibre," Nat. Photonics 8, 830–834 (2014).

[5] D. Deng, L. Liu, T. H. Tuan, Y. Kanou, M. Matsumoto, H. Tezuka,T. Suzuki, and Y. Ohishi, "Mid-infrared supercontinuum covering 3–10 μm using a As2Se3 core and As2S5 cladding step-index chalcogenide fiber," J. Ceram. Soc. Jpn. 124, 103–105 (2016).

[6] S. Kedenburg, T. Steinle, F. Mörz, A. Steinmann, and H. Giessen,"High-power mid-infrared high repetition-rate supercontinuum source based on a chalcogenide step-index fiber," Opt. Lett. 40, 2668–2671 (2015).

[7] U. Møller, Y. Yu, I. Kubat, C. R. Petersen, X. Gai, L. Brilland, D.Méchin, C. Caillaud, J. Troles, B. Luther-Davies, and O. Bang, "Multi-milliwatt mid-infrared supercontinuum generation in a suspended core chalcogenide fiber," Opt. Express 23, 3282–3291 (2015). 8. T.

[8] Cheng, K. Nagasaka, T. H. Tuan, X. Xue, M. Matsumoto, H. Tezuka, T. Suzuki, and Y. Ohishi, "Mid-infrared supercontinuum generation spanning 2.0 to 15.1 μm in a chalcogenide step-index fiber," Opt. Lett. 41, 2117–2120 (2016).

[9] B. Zhang, Y. Yu, C. Zhai, S. Qi, Y. Wang, A. Yang, X. Gai, R. Wang, Z.Yang, and B. Luther-Davies, "High brightness 2.2–12 μm mid-infrared supercontinuum generation in a nontoxic chalcogenide step-index fiber," J. Am. Ceramic Soc. 99, 2565–2568 (2016).

[10] C. R. Petersen, P. M. Moselund, C. Petersen, U. Møller, and O. Bang,"Spectral-temporal composition matters when cascading supercontinua into the mid-infrared," Opt. Express 24, 749–758 (2016).

[11] L.-R. Robichaud, V. Fortin, J.-C. Gauthier, S. Châtigny, J.-F. Couillard, J.-L. Delarosbil, R. Vallée, and M. Bernier, "Compact 3–8 μm supercontinuum generation in a low-loss As_2Se_3 step-index fiber," Opt. Lett. 41, 4605–4608 (2016).

[12] C. R. Petersen, R. D. Engelsholm, C. Markos, L. Brilland, C. Caillaud,J. Trolès, and O. Bang, "Increased mid-infrared supercontinuum bandwidth and average power by tapering large-mode-area chalcogenide photonic crystal fibers," Opt. Express 25, 15336–15348 (2017).

[13] D. D. Hudson, S. Antipov, L. Li, I. Alamgir, T. Hu, M. El Amraoui, Y.Messaddeq, M. Rochette, S. D. Jackson, and A. Fuerbach, "Toward all-fiber supercontinuum spanning the mid-infrared," Optica 4, 1163– 1166 (2017).

[14] Z. Zhao, B. Wu, X. Wang, Z. Pan, Z. Liu, P. Zhang, X. Shen, Q. Nie, S.Dai, and R. Wang, "Mid-infrared supercontinuum covering 2.0–16 μm in a low-loss telluride single-mode fiber," Laser Photon. Rev. 11, 1700005 (2017).

[15] R. A. Martinez, G. Plant, K. Guo, B. Janiszewski, M. J. Freeman, R. L.Maynard, M. N. Islam, F. L. Terry, O. Alvarez, F. Chenard, R. Bedford, R. Gibson, and A. I. Ifarraguerri, "Mid-infrared supercontinuum generation from 1.6 to > 11 μm using concatenated step-index fluoride and chalcogenide fibers," Opt. Lett. 43, 296–299 (2018).

[16] V. V. Alexander, Z. Shi, M. N. Islam, K. Ke, M. J. Freeman,A. Ifarraguerri, J. Meola, A. Absi, J. Leonard, J. Zadnik, A. S. Szalkowski, and G. J. Boe, "Power scalable > 25 w supercontinuum laser from 2 to 2.5 μm with near-diffraction-limited beam and low output variability," Opt. Lett. 38, 2292–2294 (2013).

[17] A. Tuniz, G. Brawley, D. Moss, and B. Eggleton, "Two-photon absorption effects on raman gain in single mode As2Se3 chalcogenide glass fiber," Opt. Express 16, 18524–18534 (2008).

[18] R. E. Slusher, G. Lenz, J. Hodelin, J. Sanghera, L. B. Shaw, andI. D. Aggarwal, "Large Raman gain and nonlinear phase shifts in high-purity As2Se3 chalcogenide fibers," J. Opt. Soc. Am. B 21, 1146–1155 (2004).

[19] H. Okamoto, K. Kasuga, and Y. Kubota, "Efficient 521 nm all-fiber laser: splicing pr 3+-doped zblan fiber to end-coated silica fiber," Opt. Lett. 36, 1470–1472 (2011).

[20] G. Snopatin, V. Shiryaev, V. Plotnichenko, E. Dianov, and M. Churbanov, "High-purity chalcogenide glasses for fiber optics," Inorg. Mater. 45, 1439–1460 (2009).

[21] IRFLEX, "IRF-Se series chalcogenide LWIR fibers (1.5 to 10 μm)," https://www.irflex.com/products/irf-se-series/.

[22] J. Mores, G. Malheiros-Silveira, H. Fragnito, and H. HernándezFigueroa, “Efficient calculation of higher-order optical waveguide dispersion,” Opt. Express 18, 19522–19531 (2010).

[23] H. G. Dantanarayana, N. Abdel-Moneim, Z. Tang, L. Sojka, S.Sujecki, D. Furniss, A. B. Seddon, I. Kubat, O. Bang, and T. M. Benson, “Refractive index dispersion of chalcogenide glasses for ultra-high numerical-aperture fiber for mid-infrared supercontinuum generation,” Opt. Mater. Express 4, 1444–1455 (2014).

[24] J. M. Dudley, G. Genty, and S. Coen, “Supercontinuum generation in photonic crystal fiber,” Rev. Modern Phys. 78, 1135–1184 (2006).

[25] I. Kubat, C. R. Petersen, U. V. Møller, A. Seddon, T. Benson, L.Brilland, D. Méchin, P. M. Moselund, and O. Bang, “Thulium pumped mid-infrared 0.9–9 μm supercontinuum generation in concatenated fluoride and chalcogenide glass fibers,” Opt. Express 22, 3959– 3967 (2014).

[26] C. Xia, Z. Xu, M. N. Islam, F. L. Terry, Jr., M. J. Freeman, A. Zakel, andJ. Mauricio, “10.5 w time-averaged power mid-IR supercontinuum generation extending beyond 4 μm with direct pulse pattern modulation,” IEEE J. Sel. Top. Quantum Electron. 15, 422–434 (2009).

[27] R. Pleban, A. Azari, R. Salem, and T. E. Murphy, “SSPROP,” https:// www.photonics.umd.edu/software/ssprop/.

[28] O. P. Kulkarni, V. V. Alexander, M. Kumar, M. J. Freeman, M. N. Islam, F. L. Terry, Jr., M. Neelakandan, and A. Chan, “Supercontinuum generation from 1.9 to 4.5 μm in ZBLAN fiber with high average power generation beyond 3.8 μm using a thulium-doped fiber amplifier,” J. Opt. Soc. Am. B 28, 2486–2498 (2011).

[29] R. Salem, Z. Jiang, D. Liu, R. Pafchek, D. Gardner, P. Foy, M. Saad,D. Jenkins, A. Cable, and P. Fendel, “Mid-infrared supercontinuum generation spanning 1.8 octaves using step-index

indium fluoride fiber pumped by a femtosecond fiber laser near 2 μm," Opt. Express 23, 30592–30602 (2015).

[30] P. Yan, R. Dong, G. Zhang, H. Li, S. Ruan, H. Wei, and J. Luo,"Numerical simulation on the coherent time-critical 2–5 μm supercontinuum generation in an As2S3 microstructured optical fiber with all-normal flat-top dispersion profile," Opt. Commun. 293, 133–138 (2013).

[31] A. B. Salem, R. Cherif, and M. Zghal, "Raman response of a highly nonlinear As2Se3-based chalcogenide photonic crystal fiber," in PIERS Proceedings (2011), p. 1256.

[32] I. Kubat and O. Bang, "Multimode supercontinuum generation in chalcogenide glass fibres," Opt. Express 24, 2513–2526 (2016).

[33] V. Ruddy, B. MacCraith, and J. Murphy, "Evanescent wave absorption spectroscopy using multimode fibers," J. Appl. Phys. 67, 6070–6074 (1990).

[34] Lumerical Inc., "Lumerical Mode," http://www.lumerical.com/tcadproducts/mode/.

Chapter 3 Non-destructive Characterization of Food Samples with Super-continuum Lasers

3.1 Introduction

In this chapter, we present and discuss spectroscopy systems with SC lasers we presented in the previous chapter for non-destructively measure chemical contents in process food ingredients at a stand-off distance. Specifically, we separately measure protein levels in 32 wheat flour samples with calibrated protein concentrations from 7.9% to 13.4% and French fry powders with calibrated acrylamide level to demonstrate the correlation between the sample spectra and the concentration of the chemical of interest in food samples. We measure the wheat flour samples in the NIR region while measure the French fry samples in both NIR and MIR region. The relationship between measured spectra and chemical concentrations is established through partial least square (PLSR) analysis. Our results show good high linear correlation with the concentrations measured with the gold standard method. To further characterize the performance of the system, we also measure the signal to noise ratio of the NIR system to be 27dB at 1m distance. Our results suggest that supercontinuum sources could enable the illumination of food samples from a distance that is hard to achieve with conventional light sources and therefore be used as a light source for non-contact and non-destructive quality monitoring system in food industry.

3.2 Stand-off Non-Destructive Determination of Protein Level in Wheat Flour with a Super-Continuum Laser

3.2.1 Motivation for Non-contact Protein Level Concentration in Wheat Flour

With 765 million tons of annual consumption, wheat flour is one of the major food ingredients used [1] in many everyday processed foods such as cookie and pizza. For wheat flour-based food products, the recipe parameters are highly dependent on the protein levels in the flour. Therefore, it is important to measure and control the protein content in wheat flour before the processing starts. Currently, real-time measurements of food products are carried out with spectral filter-based systems with conventional light sources (e.g., halogen lamps), which limit the flexibility and the working distance of such systems. Higher precision measurements are usually performed in lab with a table-top near infrared (NIR) spectrometer or through the destructive Dumas method. Such systems, however, do not provide the speed or ease-to-use that are necessary for real-time, stand-off, high signal-to-noise ratio spectroscopy in industrial settings. SC sources could fill this void by offering efficient beam delivery through diffraction-limited beam quality, making SC source an ideal light source for near-line or in-line applications.

3.2.2 Spectroscopy System with NIR SC Laser

To measure the wheat samples at a distance with high signal-to-noise ratio (SNR), we built a dual-arm reflective spectroscopy system that uses an all-solid-core fiber SC laser as its light source. The SC laser is based on a master-oscillator-power-amplifier (MOPA) design consisting of a nano-second seed laser followed by two stages of ytterbium doped fiber amplifiers (Fig.3-1(b)). The SC light is generated by injecting amplified 1ns pulses at adjustable repetition rate from 100kHz to 4MHz into a SC fiber. The resulting SC expansion is generated through nonlinear effects such as modulation instability and soliton self-frequency shifting [2].

Because of the MOPA design, the laser outputs scalable power between 0.3W (100kHz) to 10W (4MHz) with power stability at +/- 0.21% while maintaining the same output spectrum from 670nm to 2500nm (Fig.3-1(a)). Moreover, the output beam maintains near diffraction limited quality across the entire output spectral range, making it an ideal source for longer distance illumination [3].

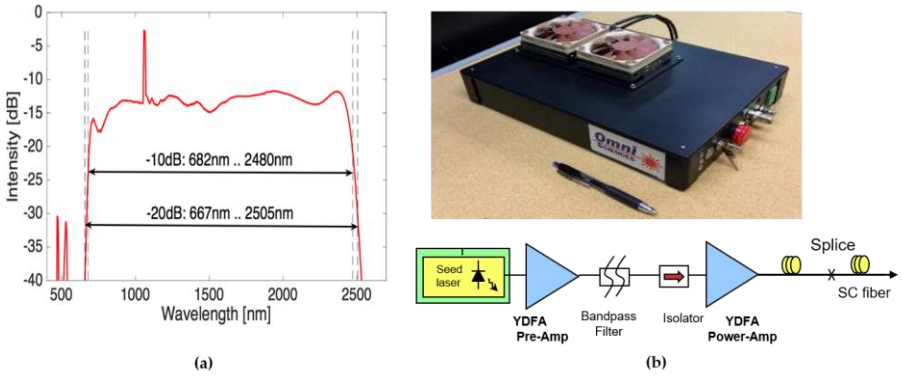


Figure 3-1 (a) Output spectrum of the SC laser (b) 10W SC laser and the block diagram used in this study

The spectroscopy system is set up with a reference arm to reduce the source fluctuation and increase the measurement consistency across different samples. To prevent the high source output power from damaging the sample, the output of the SC laser is first coupled into a monochromator (Princeton Instrument, 300g/mm grating, blazed at 2um) for wavelength selection. The selected wavelength is then split into two beams with a wedged CaF_2 window. 99% of the transmitted energy is transmitted by the CaF_2 window and directed to the sample while the reflected 1% is used to correct for the light source intensity fluctuation (Fig.3-2). To maintain the stability of the reference arm, the polarization dependent splitting ratio of the CaF_2 window needs to be controlled. Therefore, a polarizer is added before the CaF_2 window to convert the elliptical polarization of the SC output into constant linear polarization. The diffusely reflected light from the sample is then focused through a CaF_2 lens into an InGaAs detector.

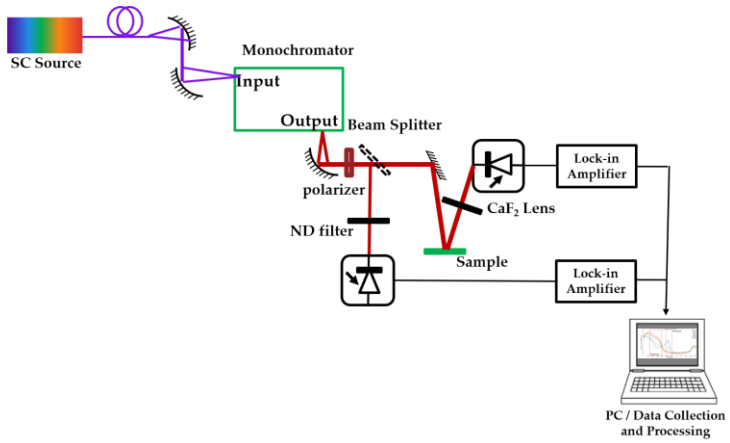


Figure 3-2 Optical setup of the dual-arm spectroscopy system with SC laser as light source used in this study

Thirty-two wheat flour samples of various protein concentrations are measured in this experiment. These wheat samples are acquired through mixing five different wheat flours purchased from local grocery store. Each of the purchased flour samples is sent to a chemistry lab (Eurofin) to have its protein concentration measured with the Dumas method. After the protein concentration measurement, these store-bought flours are thoroughly mixed by weight to create flour samples with protein concentration spanning from 7.87% to 13.4% at 0.18% interval. Each of the wheat flour samples are then evenly filled into a 2-inch petri-dish for reflectance spectra measurement.

Before taking the reflectance spectra of the wheat samples, a reflectance spectrum of a gold diffuse reflector is taken as a reference spectrum to cancel out the background source spectrum. During the sample measurements, for each of the wheat sample, two reflectance spectra from 1160nm to 2000nm and 2000nm to 2350nm are acquired in 4nm steps. A germanium filter is used to block the higher order diffraction from the shorter wavelengths when taking the spectral data between 2000nm to 2350nm.

After the spectral acquisition of each sample, the ratio between the reference arm and the signal arm is taken to remove the source fluctuation. The short/long wavelength spectra are also spliced together by aligning both spectra at an overlapping wavelength of 2000nm. The combined spectra from all 32 samples are processed using partial least square regression (PLSR) software (Pirouette, version 4.5, Infometrix Inc. Woodville, WA, USA) for wheat protein level analysis. Each spectrum is smoothed with a moving average filter and then second derivative transformed before the PLSR analysis. The PLSR models are generated from the protein level measured through Dumas method and the reflectance spectrum. Full cross-validation (leave-one-out approach) is also used to validate the PLSR model.

To further characterize the performance of the spectroscopy system at a distance, we also measure the SNR (mean/standard deviation) of the system with a gold diffuse reflector as the sample at 1m distance. We choose to measure the SNR of the ratio between reference and signal (R/S) arm over 9 minutes at 1500nm as a representation of the system SNR (Fig.3-3). The R/S ratio removes the source fluctuation to show the fundamental SNR performance and the wavelength of 1500nm corresponds to a flat region in the SC spectrum (Fig.3-1(a)). Figure 3-3 shows that the SNR of the system is 27dB at 1m distance and the noise is dominated by the detector noise with small drifts on the time scale of minutes. Such slow drifts could be caused by environment factors such as ambient temperature fluctuation.

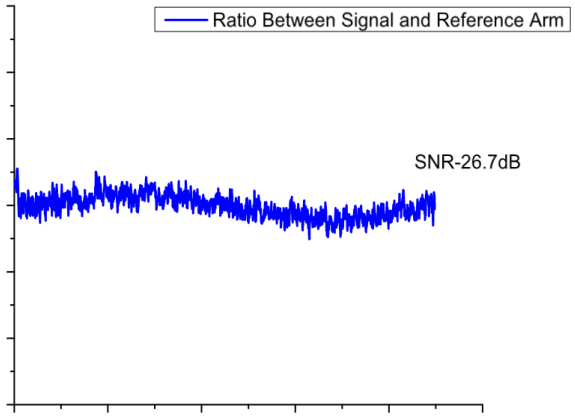


Figure 3-3 Ratio between signal and reference arm at 1500nm measured at 1m distance

3.2.3 Protein Level Prediction from NIR Spectrum

Figure 3-4(a) shows typical reflectance spectra measured from thirty-two wheat samples. The absorption peaks at 1450nm and 1915nm are from the water absorption while the features between 1700nm to 1800nm and 2200nm to 2350nm represent the absorption from C-H and C=H overtone and combinational bands [4]. Moreover, DC offsets and an upward slope can be seen across different spectra, which could be a result of different surface flatness and texture between different samples. Therefore, pre-processing such as second-order derivatives are required before the PLSR analysis. After being second-order derivative transformed (Fig.3-4b), the DC offsets and upward slopes across different samples are greatly reduced, which in turn emphasis the spectral difference between samples with different protein concentrations.

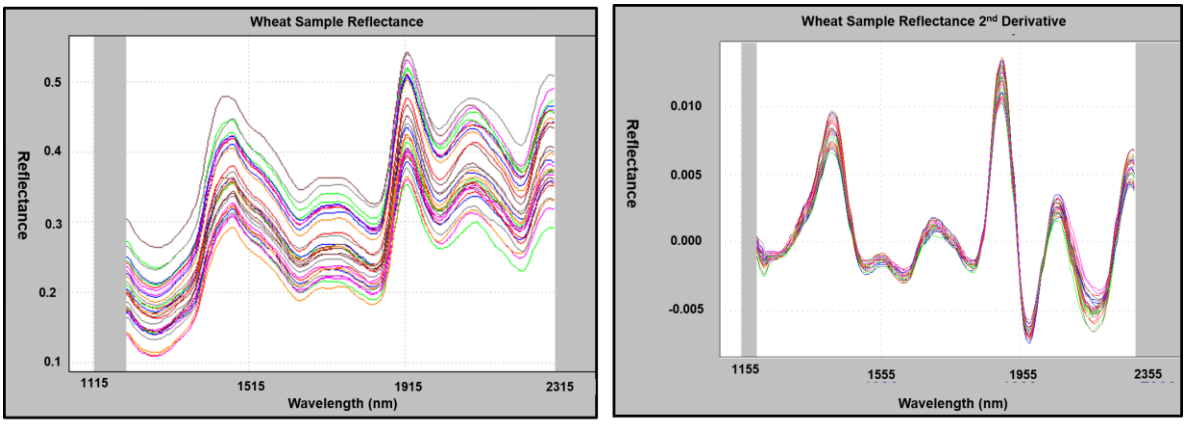


Figure 3-4 (a)Typical reflectance spectrum of the wheat sample from 1100nm to 2400nm. (b) Reflectance spectrum after being second order derivative transformed

The predicted protein concentration versus the Dumas method measured protein concentration can be seen in Figure 3-5 (a). Similar to what we found before [5], combining both the shorter (1160-2000nm) and longer wavelength (2000-2350nm) spectra yield the best protein level detection capability.

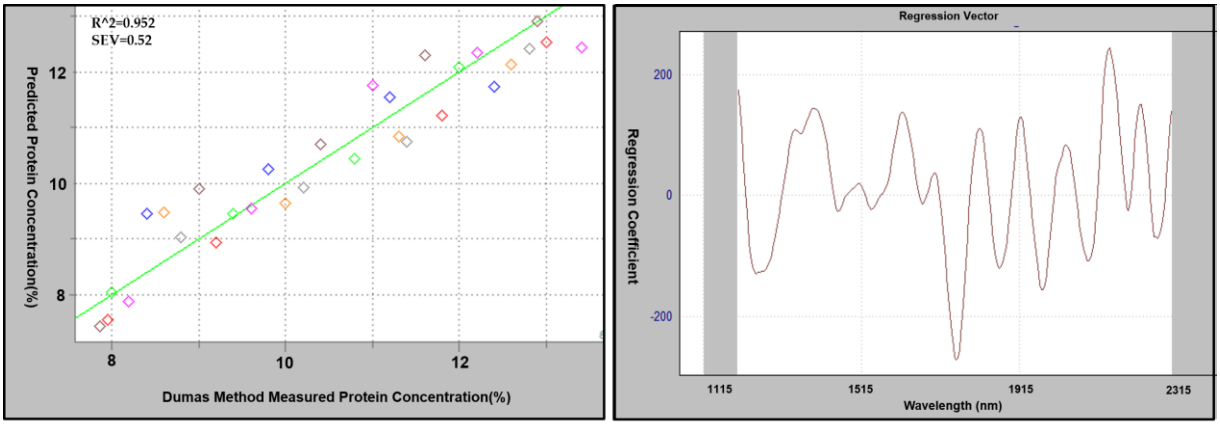


Figure 3-5 (a)PLS fitting between the predicted protein concentration versus the Dumas method measured protein concentration (b)Regression vector across the wavelength range 1160nm to 2350nm

In this study, the predicted protein concentration shows clear linear correlation to the protein concentration measured with gold standard method, with R square value >0.95 and standard error variation at 0.52%. The regression vector (Fig.3-5 (b)) shows that the whole spectrum across the wavelength range from 1160nm to 2350nm contribute equally to the PLS

model, indicating that wide spectral coverage (instead of discrete wavelengths) may be important for accurate protein concentration measurements.

3.3 Non-Destructive Detection of Acrylamide in Potato Fries with a High-Power Supercontinuum Laser in both NIR and MIR

3.3.1 Motivation for Non-Destructive Detection of Acrylamide

Acrylamide that forms in fried, starchy foods has recently drawn attention for being potentially carcinogenic, according to some animal studies [6]. The current gold standard for measuring acrylamide in food is through gas or liquid chromatography-mass spectroscopy (GCMS/LCMS). However, such methods often take hours to run and need specially trained technicians to operate and prepare samples. Infrared spectroscopy, an alternative approach, can provide fast and non-destructive chemical analysis of food samples. Currently, the conventional light sources (halogen lamp, for example) often used in commercial infrared spectroscopy devices, do not provide the beam quality and brightness necessary for real-time, stand-off, high signal-to-noise-ratio spectroscopy in industrial settings. SC lasers could fill this void by offering diffraction-limited beam quality [7] and covering the NIR and MIR simultaneously, making them an ideal light source for near-line or in-line applications.

3.3.2 Spectroscopy System using NIR and MIR SC Lasers

Both NIR and MIR wavelength ranges are used in this experiment. The NIR range is chosen for the availability of the higher power light source as well as the stronger diffusive scattering from the sample, potentially allowing sample characterization from a further distance. The MIR range, on the other hand, contains fundamental absorption peaks of acrylamide, providing more direct relationship between the absorption spectrum and the acrylamide

concentration. To collect the absorption spectra within each spectrum range effectively, we use separate optimized NIR and MIR set-ups. For the NIR measurement, the diagram of our spectroscopy system is shown in Figure 3-7 (a). The SC laser (Fig. 3-7(b)) is an all-fiber SC laser capable of outputting >10W of average power at 4 MHz pulse repetition rate. The SC output ranges from 670nm to 2500nm. The output from the SC laser is first coupled into a grating monochromator (Princeton Instrument, 300g/mm grating, blazed at 2m), which selects a small spectral window to illuminate the sample holder at a 45-degree angle. The monochromator is placed before the sample to prevent the sample from heating up due to direct illumination of a high-power laser beam. The diffused scattered light emitted from the sample is captured with a 1-inch diameter parabolic mirror and focused onto an InGaAs photodiode.

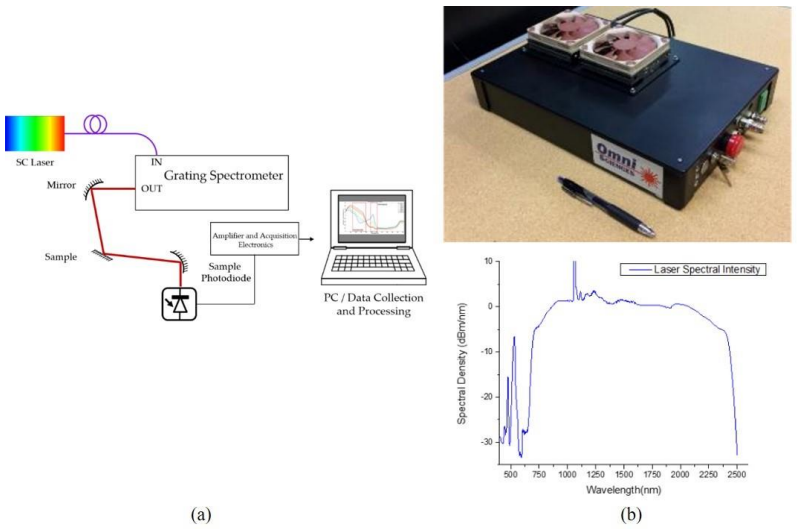


Figure 3-6 (a) Diagram of the stand-off NIR spectroscopy system (b) High power SC laser and output spectrum used in the system

During the NIR spectra collection, each potato fry powder sample is evenly packed in an aluminum foil dish and placed on the sample holder such that the beam is illuminating the center of the dish. The measurement wavelength ranges used for this study are 1100-2100nm and 2000-2500nm. The 1100-2100nm spectral range contains the absorption information from carbon

hydrates in the first overtone band, while the absorption features between 2000nm and 2500nm corresponds to the combinational bands. For each of the samples, the infrared spectrum is taken three times with a 2nm step size over both wavelength ranges, and the three spectra are averaged. A germanium filter is used to block the higher order diffraction from the shorter wavelengths when taking the spectral data between 2000nm to 2500nm. Between each sample measurement, a blank reference spectrum is taken with a roughened aluminum plate on the sample holder to cancel out the fluctuation caused by environmental change and the background laser output spectrum. For the MIR SC measurements, samples are measured in the system shown in Figure 3-8 (a). The SC laser is an all-fiber SC laser covering the wavelength range of 1600nm to 11000nm (Fig. 3-8(b)) with output power exceeding 500mW. The detail of the SC laser can be found in [8,9]. Similar to the NIR system, a grating monochromator (Princeton Instrument, 150g/mm grating, blazed at 5m) is first used to filter out a narrow spectral window from the SC spectrum between 4000nm to 8000nm (limited by the detector and filter at the time of the experiment). The filtered light is then coupled into a three-reflection ATR cell. The output of the attenuated total reflection (ATR) cell is then collected by a 1-inch ZnSe lens and is coupled onto a mercury-cadmium-telluride detector (Vigo). Moreover, to further confirm the results from the SC laser, the same samples are also measured with a commercial ATR-FTIR (Nicolet iS50 FT-IR).

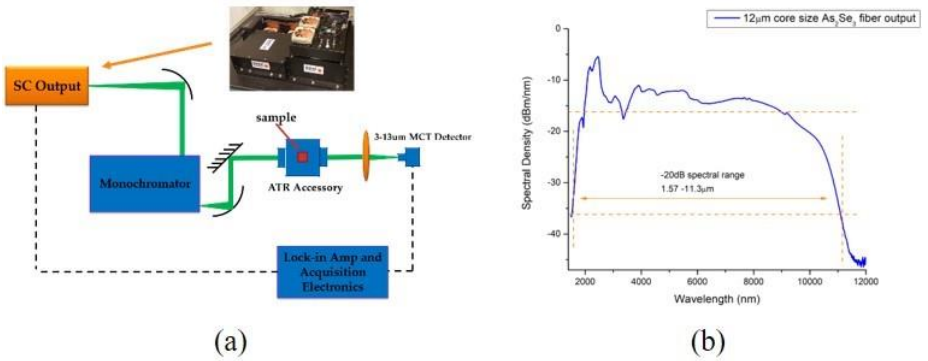


Figure 3-7 (a) Diagram of the MIR spectroscopy system (b) MIR SC laser used in the system

Thirty-two French fry samples are prepared (McCain Foods, Canada) for this study [5]. These samples are fried between 2-5 minutes at 10 second intervals to create different acrylamide levels. The fried samples are then frozen with liquid nitrogen and blended into fine, homogenous powders, which minimize the spectral artifacts from varying particle sizes between samples. Before the GCMS measurement, acrylamide in each sample is extracted with the QuEChERS method [10].To extract the acrylamide, 1g of French fry powder is placed in a 50ml centrifuge tube and added to 0.5ml of a 1ppm solution of 13C-labelled acrylamide in acetonitrile. Hexane(5ml) is then added to the tube, which is vortexed for 30 seconds to de-fat the sample. Next, a salt consisting of 4g MgSO4 and 0.5g NaCl is added to each sample [11]. The tube is then centrifuged for 6 minutes at 4500rpm. Following the centrifuge, 1ml of the acetonitrile is transferred to a 2ml microcentrifuge vial containing 50mg of primary and secondary amines and 150mg of MgSO4. This microcentrifuge vial is vortexed and centrifuged for 1 minute at 5000rpm. Finally, the supernatant is transferred into an autosampler vial for the GCMS measurement. An Agilent Technologies 7820A GC is used with a 5877B MSD (Santa Clara, CA, USA) in this study. A 50m HP-5MS column with a width of 0.25mm and inner diameter of 0.25 m is used for separating the analytes. In addition to the acrylamide solution extracted from the French fries, a standard curve is also obtained by measuring calibrated 13C-labeled acrylamide

solutions with concentrations ranging from 7.8ppb to 1000ppb. Following the GCMS measurement, two major ions at 71.1 and 74.1m/z are measured and used for quantification of the acrylamide concentration. After the sample measurement and calibration, the collected spectra are processed using partial least square regression (PLSR) software (Pirouette, version 4.5, Infometrix Inc. Woodville, WA, USA) for acrylamide content analysis. Each spectrum is second derivative transformed before the PLSR analysis. In addition, the water absorption features at both 1450nm and 1915nm are excluded from the analysis to improve the model robustness, as the water concentration in the samples is sensitive to frying time, storing condition, and environmental humidity, which could distort the results. The quantitative models are generated from the GCMS measured reference data and both the NIR and MIR spectrum. Full cross-validation (leave one out approach) is also used to validate the PLSR model. Samples with residuals greater than 2 are considered outliers and excluded from the analysis.

3.3.3 Predicting Acrylamide Level using NIR and MIR Spectrum

The typical French fry spectra measured in NIR are shown in Figure 3-9 (a) (1100-2100nm) and (b) (20002500nm). The absorption peaks at 1450nm and 1915nm correspond to water absorption in the samples, while the features between 1700nm to 1800nm and 2300nm to 2400nm represent the absorption from C-H overtone and combinational bands [12].

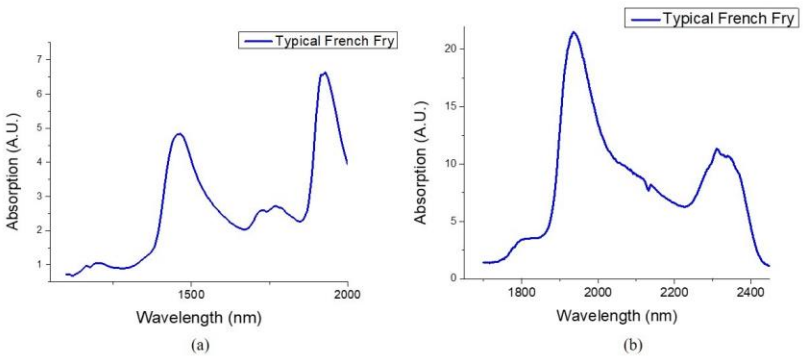


Figure 3-8 Typical French fry absorption spectrum measured with the SC laser between (a)1100-2100nm and (b) 2000-2500nm

Figure 3-10(a) shows the typical MIR sample absorption spectrum measured with the SC laser after background correction. The spectrum was taken with a wavelength step of 10nm over the 4000 to 8000nm wavelength range. A 4um long pass filter is used during the measurement to block the higher order diffraction from shorter wavelengths. Both the laser measured spectrum and the FTIR measured spectrum (Fig. 3-10(b)) shows similar features, with the peak at 6100nm corresponds to water absorption and peaks 5700 and 6800nm corresponds to the fundamental absorption band of C-H, C=H bond.

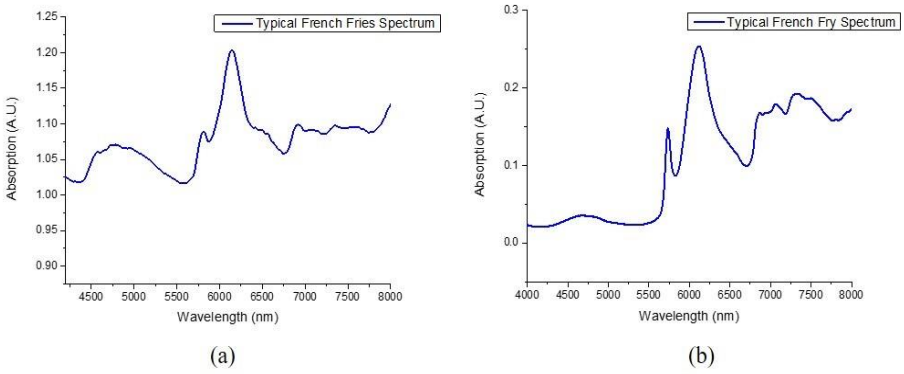


Figure 3-9 Typical French fry absorption spectrum measured with the SC laser between 4000-8000nm measured with both a (a) MIR SC laser and a (b) commercial ATR-FTIR

The predicted acrylamide level in the French fry samples is obtained through PLRS method based on the calibrated acrylamide level from GCMS. Fig. 3-11(a) shows the linear relationship in the shorter wavelength spectra (1100nm-2100nm) between the predicted

acrylamide concentration and the GCMS measured concentration with reasonable R value>0.85. Upon closer inspection of the regression vector (Fig. 3-11(b)), we find most of the correlation can be explained by the wavelength range between 1680nm to 1780nm, which is associated with the first overtone band of C-H, C=O bonds [7].

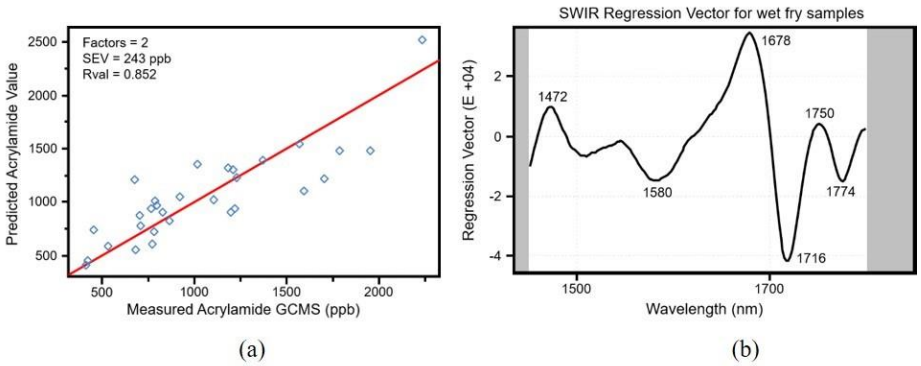


Figure 3-10 (a) PLSR correlation plot (1100nm-2100nm) between predicted and measured acrylamide levels in French fries. (b) Regression vector plot (1100nm-2100nm) of the PLSR model using the NIR SC spectroscopy system.

A better correlation between the acrylamide levels and the NIR spectra is obtained in the longer wavelength between 2000nm to 2500nm. Figure 3-12 (a) shows improved linear relationship between the estimated acrylamide concentration and the GCMS measured acrylamide concentration, with R value>0.93 and standard error at 161ppb. The regression vector plot (Fig. 3-12(b)) shows the correlation to the acrylamide levels can be explained by absorption features between 2250nm and 2450nm. The improved performance in the longer wavelength over the short wavelength side could be attributed to less scattering and stronger absorption in the combinational band compared to the first overtone band from the powdered sample.

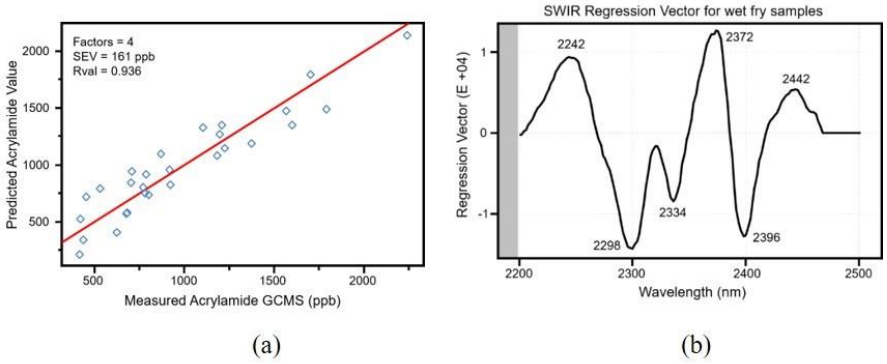


Figure 3-11 (a) PLSR correlation plot (2000nm-2500nm) between predicted and measured acrylamide level in French fries. (b) Regression vector plot (2000nm-2500nm) of the PLSR model using the NIR SC spectroscopy system.

Furthermore, to explore if combining both the shorter and longer wavelength range would yield better acrylamide detection performance, we splice the 1100-2100nm and 2000-2500nm spectra together by aligning both spectra at an overlapping wavelength of 2050nm. By combining both spectral ranges together, the R value of the correlation increases to 0.95 while the standard error decreases to 145ppb (Fig. 3-13(a)). Further analysis of the regression vector (Fig. 3-13(b)) shows both 1680-1780nm and 2250-2450nm wavelength ranges contributing to the correlation of the acrylamide levels (greyed-out spectrum corresponds to water absorption) ; however, the long wavelength contribution is more predictive and significant.

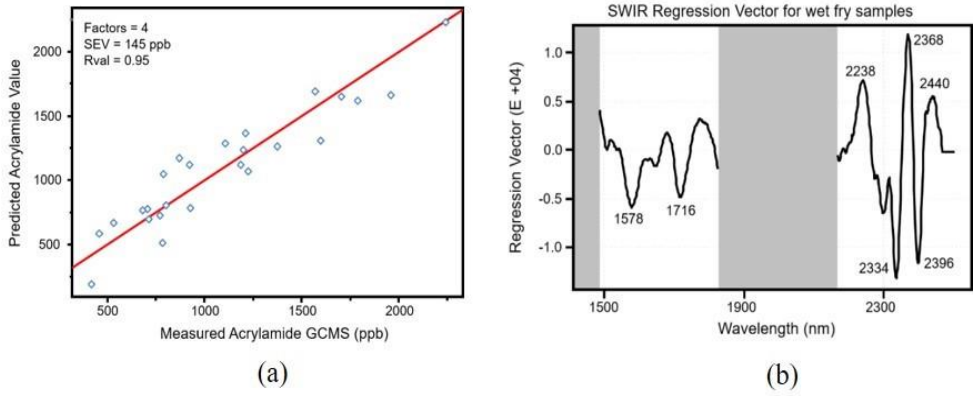


Figure 3-12 (a) PLSR correlation plot (1100nm-2500nm) between predicted and measured acrylamide levels in French fries. (b) Regression vector plot (1100nm-2500nm) of the PLSR model using the NIR SC spectroscopy system.

For the PLSR model in the MIR range, the PLSR plot was shown in Figure 3-14. The regression vector suggests the correlation between the acrylamide level and absorption spectrum

can be mostly explained by the absorption features related to C-H, C=H bond near 6740nm. However, the correlation plot (Fig. 3-14(a)) also suggests that the absorption spectrum in the MIR range is less correlated to the GCMS measured acrylamide, with R-value decreases to 0.8 and SEV increases to 215ppb. Similar degradation of correlation can also be observed from MIR spectrum taken with the commercial FTIR (Fig. 3-15), which shows similar linear relationship between the predicted and the measured acrylamide levels.

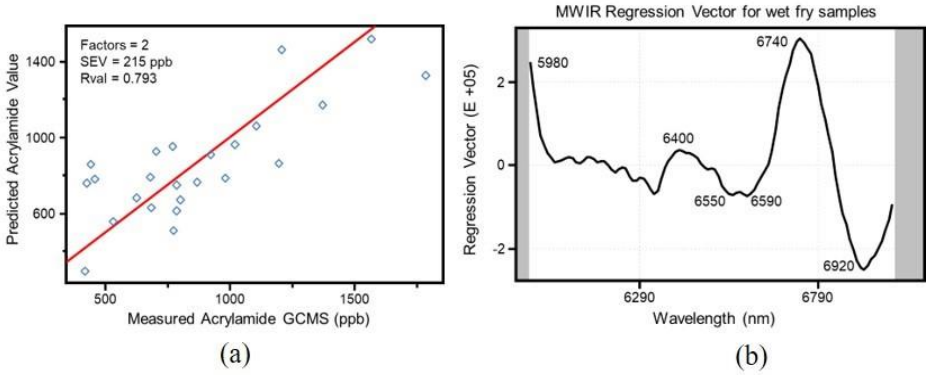


Figure 3-13 (a) PLSR correlation plot (4000nm-8000nm) between predicted and measured acrylamide level in French fries. (b) Regression vector plot (4000nm-8000nm) of the PLSR model using the NIR SC spectroscopy system.

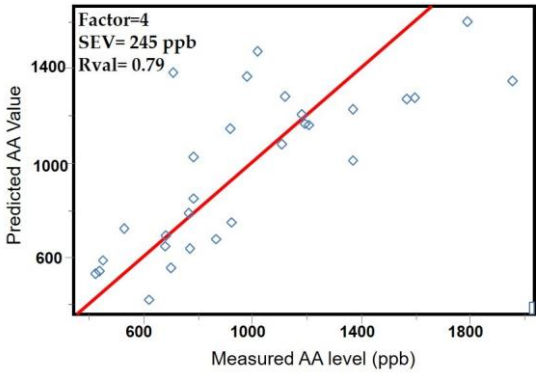


Figure 3-14 PLSR correlation plot (4000nm-8000nm) between predicted and measured acrylamide level in French fries measured with a commercial FTIR

3.4 Discussion

Both our NIR measurements on wheat flour and French fries show very good correlation between the reflectance spectrum and the gold standard measured concentration but such

measurement could be sensitive to different factors. During our measurements, we find that the consistency of sample preparation and proper post-processing of the acquired spectra (e.g., second order derivative transformation) are important to measurement repeatability because the flatness and the texture of the wheat sample can cause a slight bowing and offset in the spectra. Moreover, we also noticed that it is very helpful to add the reference arm to the spectroscopy system when a SC laser source is used as the light source due to the pulse-to-pulse variations of SC sources. Such factors can be more important for chemicals such as acrylamide that has no strong absorption within the NIR spectral range, the NIR measurements actually reflect the changes of the various carbon-hydrate contents (fat and starch for example) that are associated with the change of the acrylamide concentration.

In comparison, MIR spectra contain the strong absorption peaks for both the acrylamide and carbon-hydrates, which could more truthfully reflect the acrylamide levels with less interference from external factors. However, in our experiments, we see instead a decrease of correlation between MIR spectra and acrylamide concentration compared to the NIR spectra. Such degradation could be due to several factors such as the sampling volume is smaller in MIR measurements because of the size and penetration depth of the ATR cell. Moreover, MIR absorption spectrum is more vulnerable to changes that are less correlated to the change of the acrylamide concentrations (sample storage condition or sample texture, for example) compared to the NIR spectrum. Furthermore, although the MIR measurements in this study are limited with using an ATR cell, the high brightness SC source could eventually enable MIR spectral measurement from a stand-off distance.

However, the SC laser is still a key enabler in stand-off measurement because of the flatter spectra as well as the high brightness brought by the superior beam quality. Compared to a

conventional light source (a 1800K black body radiation source) of same output power, the SC source used in this study provides 2.2 times higher the spectral density over the NIR wavelength range. Furthermore, due to the diffraction-limited output beam quality from the single mode fiber, SC laser would allow efficient power delivery at a distance. For example, a F# 4 parabolic mirror would only collect 2.5% of the light while almost 100% of the light can be collected from the SC laser. Combining these two factors, SC laser could provide almost two orders of magnitude higher brightness across the NIR spectral range than a conventional light source (Fig.3-15). In this study, we see that at 1m distance, the SNR of the NIR system is 27dB and mainly limited by detector noise. If a conventional light source was used as the light source, the SNR would drop to single digit, requiring long integration time to achieve the same SNR as the SC system. As a comparison, the acquisition speed of the current SC system is mainly limited by the mechanically scanning monochromator. If faster instruments such as acousto-optic tunable filters or FTIRs [13] are used, the acquisition time could be reduced to a fraction of a second. These benefits of the SC source could eventually enable more versatile real-time quality inspection of food samples from a stand-off distance in various situations.

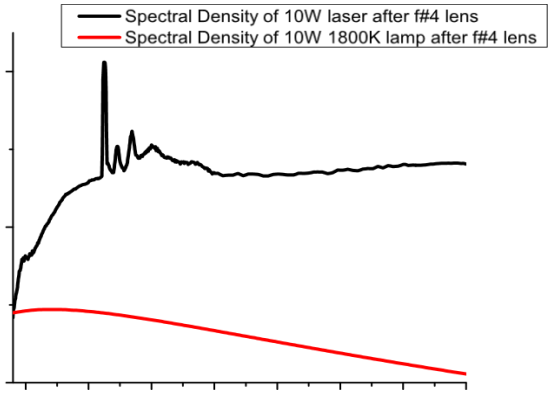


Figure 3-15 NIR SC laser output two orders of magnitude higher spectral density compared to black body source of same output

3.5 Chapter Summary

In conclusion, we present experimental results showing the use of SC lasers for stand-off food inspection. The high brightness of the SC sources allows our system to keep high SNR even at 1 m distance. In the NIR wavelength regime, we show that the NIR spectrum correlates well with protein level in wheat flour and the acrylamide level in fried French fry powders. We also explored the use of MIR for the inspection of acrylamide in French fry powders with an ATR cell. Even though the SC laser measured MIR spectra show less correlation to the actual acrylamide level, it could lead to direct stand-off quantitative acrylamide level measurements due to high acrylamide absorption in MIR wavelengths as well as the high beam quality of the SC source. Our result suggests that SC laser could enable real-time inspection/monitoring at a stand-off distance, with good agreement to the gold standard method such as Dumas/GCMS method in an industrial setting.

Reference

[1] USDA, “World Agricultural Production”, USDA, Washington, DC (2019).

[2] Dudley, J. M., Genty, G., and Coen, S., “Supercontinuum generation in photonic crystal fiber," Reviews of modern physics 78(4), 1135 (2006).

[3] Alexander, V. V., Shi, Z., Islam, M. N., Ke, K., Kalinchenko, G., Freeman, M. J., Ifarraguerri, A., Meola, J., Absi, A., Leonard, J., et al., “Field trial of active remote sensing using a high-power short-wave infrared supercontinuum laser," Applied optics 52(27), 6813-6823 (2013).

[4] Wong, K. A., “Screening for acrylamide levels in french fries using portable vibrational spectrometers," (2017).

[5] Guo, K., Demory, B., Meah, S. Z., Zhai, T., Martinez, R., Islam, M. N., Maksymiuk, L., Terry, F. L., DeWilde, C. A., Freeman, M. J., et al., “Non-destructive detection of acrylamide in potato fries with high-power supercontinuum lasers," in [Fiber Lasers XVI: Technology and Systems], 10897, 108971S, International Society for Optics and Photonics (2019).

[6] Johnson, K. A., Gorzinski, S. J., Bodner, K. M., Campbell, R. A., Wolf, C. H., Friedman, M. A., and Mast, R. W., “Chronic toxicity and oncogenicity study on acrylamide incorporated in the drinking water of fischer 344 rats," Toxicology and applied pharmacology 85(2), 154-168 (1986).

[7] Alexander, V. V., Shi, Z., Islam, M. N., Ke, K., Kalinchenko, G., Freeman, M. J., Ifarraguerri, A., Meola, J., Absi, A., Leonard, J., et al., “Field trial of active remote sensing using a high-power short-wave infrared supercontinuum laser," Applied optics 52(27), 6813-6823 (2013).

[8] Martinez, R. A., Plant, G., Guo, K., Janiszewski, B., Freeman, M. J., Maynard, R. L., Islam, M. N., Terry, F. L., Alvarez, O., Chenard, F., et al., “Mid-infrared supercontinuum generation from 1.6 to> 11 _m using concatenated step-index fluoride and chalcogenide fibers," Optics letters 43(2), 296-299 (2018).

[9] Guo, K., Martinez, R. A., Plant, G., Maksymiuk, L., Janiszewski, B., Freeman, M. J., Maynard, R. L., Islam, M. N., Terry, F. L., Bedford, R., et al., “Generation of near-diffraction-limited, high-power supercontinuum from 1.57 μm to 12 μm with cascaded fluoride and chalcogenide fibers," Applied optics 57(10), 2519-2532 (2018).

[10] Mastovska, K. and Lehotay, S. J., “Rapid sample preparation method for lc- ms/ms or gc-ms analysis of acrylamide in various food matrices," Journal of Agricultural and Food Chemistry 54(19), 7001-7008 (2006).

[11] Wong, K. A., “Screening for acrylamide levels in french fries using portable vibrational spectrometers," (2017).

[12] Ayvaz, H. and Rodriguez-Saona, L. E., “Application of handheld and portable spectrometers for screening acrylamide content in commercial potato chips," Food chemistry 174, 154-162 (2015).

[13] Martinez, R. A., Guo, K., Zhai, T., Terry, F. L., Pierce, L. E., Islam, M. N., Gibson, R., Reed, J., Bedford, R., Maksymiuk, L., et al., “Active mid-wave to long-wave supercontinuum ftir sensor for standoff chemical detection," Journal of Lightwave Technology (2019).

Chapter 4 Contactless Measurement of HR and RR with a Time-of-Flight Camera

4.1 Introduction

We demonstrate a contactless vital sign monitoring (CVSM) system based on a near infrared indirect time-of-flight (ToF) camera that can measure the HR and the RR of an individual at a stand-off distance. The system utilizes a vertical-cavity surface-emitting laser (VCSEL) illuminated indirect ToF camera, which measures both grayscale intensity and depth information simultaneously. We use grayscale intensity information as well as the distance information from two regions of interest (ROI) of a participant to determine the HR and RR. The HR is derived from periodic intensity change on a participant's face induced by blood flow from the heartbeats, while the RR is determined by measuring the periodic change of chest wall movement during breathing. We find that the motion artifacts can dominate the underlying HR signal especially when an active illumination source such as VCSEL lasers are used. In this study, we use the depth information from the ToF camera to compensate for these motion artifacts since the depth information can be used to differentiate the grayscale intensity variations caused by underlying heartbeat versus the user's motion.

We conducted a pilot human study with 29 participants of varying demographics to show that when using distance-based motion compensation, the success rate (defined as the HR reading within 10% of the reference HR measurement) of HR measurement increases to 75%, as compared to only 35% when distance-based motion compensation is not used. The mean deviation from the reference HR measurement is −6.25 BPM if we apply the depth signal for

motion compensation, while the deviation increases to 21 BPM when motion compensation is not used. At the same time, our study shows that the mean deviation of our RR measurement is 1.7 BPM, which is comparable to the pulse oximeter we used in this study. Our results further show that the system performs well among participants of various demographics such as skin color, gender, and age. Such systems could be useful in applications such as vehicle driver/occupant monitoring systems, remote and in-patient patient monitoring systems, telemedicine systems, or unobtrusive health screening systems.

4.2 Motivation

Contactless physiological monitoring systems working at a remote distance have attracted much attention over the past decades. Especially after the COVID-19 pandemic in early 2020, there has been an increased demand for contactless physiological monitoring systems for health monitoring/screening at a safe distance to reduce the spread of viruses. Out of many potential physiological parameters, HR and RR have attracted much attention. To date, most contactless HR/RR measurement systems rely on photoplethysmography (PPG) using RGB (red-green-blue) cameras with visible light illumination [1–8]. Several approaches, such as the skin-tone or blind-source separation-based algorithm, are proposed for the removal of external artifacts and considerably improve the reliability of HR measurement [9–16]. However, in some application scenarios such as vehicle driver monitoring or patient monitoring in hospitals, RGB camera-based systems face challenges from fluctuating or very low background illumination [17]. Moreover, because melanin, which gives rise to skin color, has ~5X higher absorption in visible wavelength of 530 nm as compared to 850 nm [18], the performance of RGB camera-based systems can vary among users of different skin colors [6,10,17]. By using near-infrared illumination, such skin color dependence can be mitigated to achieve more uniform performance

among wider demographics. Due to the benefits of being independent of background illumination and users' skin color, remote HR and RR monitoring systems using a near-infrared light source can be a valuable alternative.

Over the past few years, HR/RR measurement systems using near-infrared cameras or even RGB/Depth cameras (such as Microsoft Kinect) [19–24,28,29] have been studied to show their capability of measuring HR/RR. In this study, we propose a system that leverages the existing ToF cameras in many consumer electronics and vehicles to perform HR and RR monitoring. The ToF camera used in this study is an indirect ToF using a modulated VCSEL laser as its light source [30]. The benefit of this type of ToF camera is that it can extract the grayscale and depth information at the same time. The grayscale image is directly acquired through the exposure of the imaging sensor while the depth image is acquired by examining the phase change of the returned light [30]. Compared to previous studies, one of the main advantages and technical advancements of this study is that we demonstrate a method that combines both the depth and grayscale intensity information from the ToF camera to compensate for motion artifacts. Motion artifacts are known to be a challenging issue for contactless PPG systems, but even more so for systems that operate in the near-infrared wavelengths because the absorption by hemoglobin is much weaker in the near-infrared compared to visible wavelengths [31,32]. As a result, the PPG signal strength between 850 nm to 1000 nm is only about 1/8th the peak amplitude at 530 nm. Since the ToF camera directly measures the body motion of a participant, we find this information useful in distinguishing intensity changes caused by body motion versus heartbeat, which would allow us to compensate for motion-induced artifacts. In addition, by measuring the motion of the chest wall using the ToF camera, we can at the same time directly measure the RR of a participant, instead of extracting RR from HR or other indirect

body motion when an RGB camera is used [26,27]. The ability of measuring RR independent of HR allows the HR/RR function of the system to run independently. Even if HR or RR measurements failed because of the external interference, the system should still be able to continue measuring the other parameter. Furthermore, to our knowledge, this is the first study that investigates the performance of a ToF-based HR/RR monitor system over larger and diverse demographics [32]. A more detailed comparison between this study and previous studies using IR cameras is presented in Table 4-1. It should be noted that the testing conditions as well as the demographics of the participants in different studies are different. Therefore, the results from each study should not be compared directly to each other. For example, in [19], participants are asked to put their head on the head rest during the stationary measurements whereas in this study, the participants are asked to behave normally during the measurements. As indirect ToF cameras are being widely used in many consumer electronics, our CVSM system would enable low-cost, reliable, and multi-modality physiological signal monitoring on various platforms and application scenarios in the future. For example, such a system can be mounted in a vehicle to help monitor the physiological condition of the driver in a continuous manner (we will discuss this in more detail in Chapter 5).

Table 4-1 Summary of recent studies on IR camera-based HR/RR monitoring system

Reference	Wavelength (nm)	Camera Type	HR Error (BPM)	Measures RR?	Avg.RR Error (BPM)	# of Participants
[19]	675/800/842	NIR	0.79	No	N/A	6
[21]	940	NIR	13.6 (RMSE)	No	N/A	2
[24]	850	ToF	3.46	No	N/A	7
[23]	850	NIR	-2	No	N/A	10 (infants)
This Study	850	ToF	6.25	Yes	1.7	29

4.3 Experiment Setup and Procedure

The indirect ToF camera used in this study is a CamBoard Pico Flexx camera (PMD Technologies AG, Siegen, Germany). This camera contains a 3D CMOS sensor with a resolution of 171 × 224, and a field of view of 62° × 45°. The illumination source on the camera is an 850nm VCSEL with eye-safe power output and an operating distance from 0.1 to 4 m. This ToF camera comes with a compact form factor of 68 mm × 17 mm × 7.35 mm and consumes only 300 mW average power, which makes it ideal for mobile application scenarios. In our experiment, the ToF camera is connected via USB to a laptop (2019 Lenovo X1 Extreme), which is used to both control the camera and process the recorded 3D video to extract HR and RR. The ToF camera is mounted on a stand positioned at the same height and ~60 cm away from the participants, which allows us to capture a participant's face and chest region in one frame (Figure 4-1). To provide a reference HR and RR reading, a contact-based finger pulse oximeter capable of recording both HR and RR with accuracy down to +/− 1 BPM (Mighty Sat Rx, Masimo, Irvine, CA, USA) is placed on one of the participant's index fingers. All measurements are made under the illumination of fluorescent light (mounted on the ceiling, powered by AC electricity at 60 Hz), no special control of ambient light illumination is applied during the study.

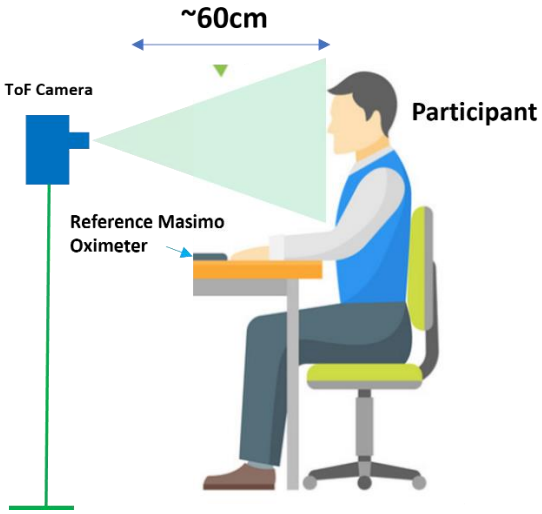


Figure 4-1 Experimental configuration for proof-of-concept HR, RR measurements using the Pico Flex indirect ToF camera.

To determine the HR and RR of a participant, two ROIs are used to extract HR and RR of the participant (Figure 4-2): ROI-1 is used for HR extraction while ROI-2 is used for RR extraction. The location of ROI-1 that covers both the nose and cheek is calculated by evaluating the relative position between the participant's eyes and nose with a 66-point facial landmark detection algorithm [33]. The ROI-2 region that represents the upper chest regions is determined from the relative position between the jawline and the shoulder using a pose estimator [34]. Specifically, the system uses both grayscale intensity and depth information from ROI-1 to derive the HR while only the depth information from ROI-2 (upper chest) is used to derive the RR.

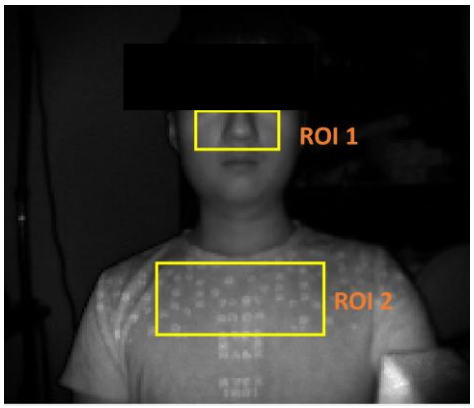


Figure 4-2 Three ROIs used for RR and HR extraction: ROI-1 is used for HR measurements while ROI-2 is used for RR measurements

One advantage of using an indirect ToF camera for physiological monitoring is that it can operate under low or complex ambient light conditions. The enhanced immunity against external lighting conditions is a result of the narrow band-pass filter (centered at 850 nm) placed in front of the optical lens as well as the background illumination suppression from the detection mechanism used in the indirect ToF camera [30]. To demonstrate the benefits of being independent of ambient lighting in physiological measurements, we show the results of HR measurement under various lighting conditions: a dark environment, a bright environment, and an environment where ambient light is switched on/off periodically. Figure 4-3 shows the (a) raw

intensity from ROI-1 when measured under the dark/bright environment and the (b) corresponding frequency domain information. When measuring under the dark environment, all ambient lights are switched off and the background illumination is reduced to <1 Lux. When measuring under the bright environment, in addition to the ambient fluorescent lighting, a 100 W halogen lamp is placed 1 m from the participant to create an illumination of 960 Lux. In both cases, since our system relies on the built-in VCSEL laser for illumination, a clear HR signal can still be seen in the time domain and the correct HR rate is obtained using a Fourier transform.

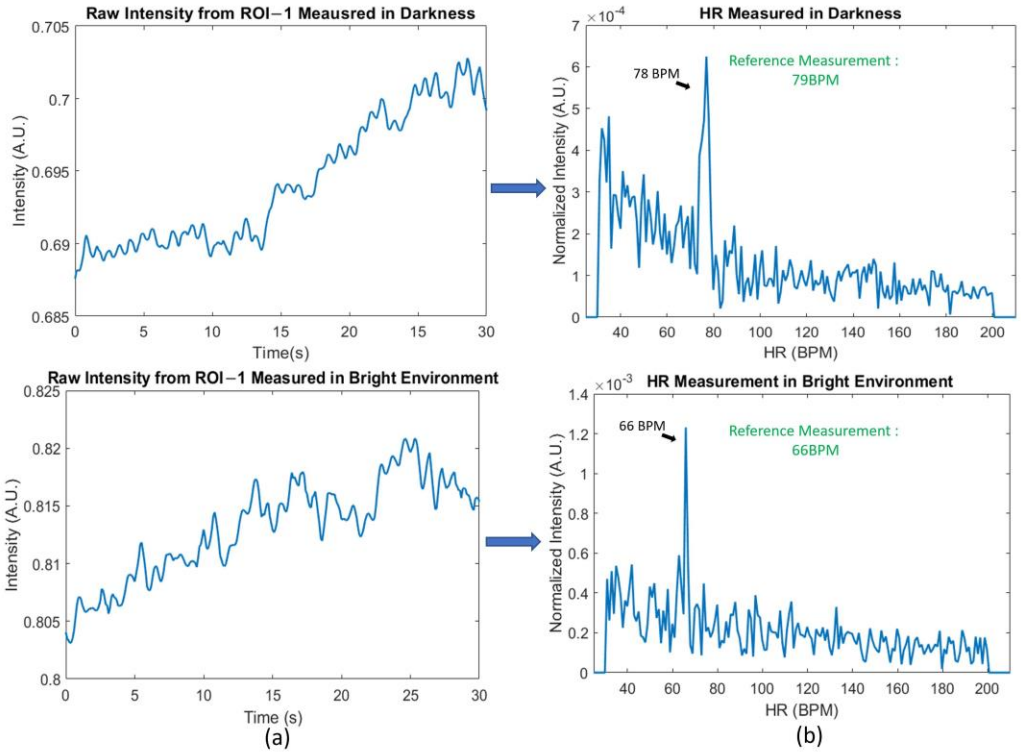


Figure 4-3 (a) Raw intensity signal from ROI-1 measured in dark/bright environment. The grayscale intensity shows a clear HR signal. (b) Frequency domain HR measured in dark/bright environment. The highest peak in the frequency domain corresponds to measured HR.

We also demonstrate that the ToF camera can operate under more extreme lighting conditions. Figure 4-4 shows a measurement obtained with ambient light switched on and off at an interval of 5 s. When the ambient light is turned off, the background illumination intensity is less than 1 Lux while when the ambient light is turned on, the background illumination is 330

Lux. No significant effects of ambient light being turned on/off are seen in Figure 4-4a and a correct HR measurement is still obtained with a Fourier transform.

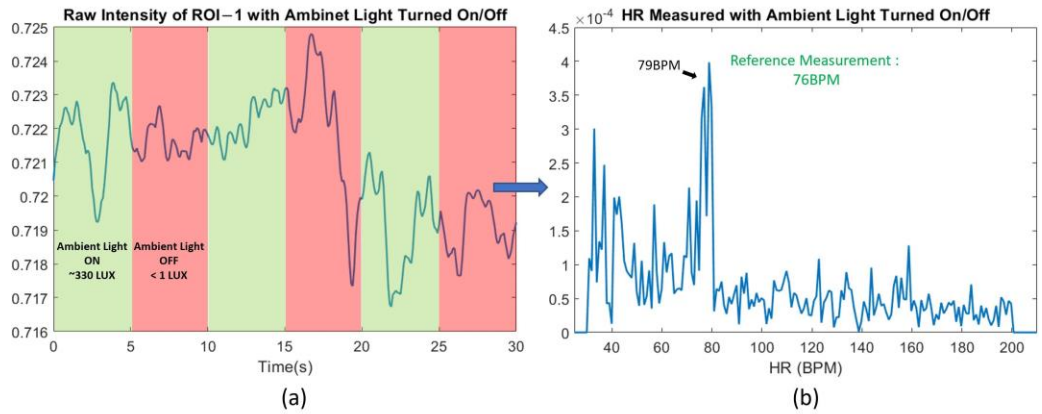


Figure 4-4 (a) Raw intensity signal from ROI-1 measured under alternating dark and bright environment. The ambient is switched on/off at an interval of 5 s. (b) Frequency domain HR measured under alternating lighting condition. The highest peak in the frequency domain corresponds to measured HR

Motion artifact is a key source of noise in contactless HR measurements, especially on a system with low power and active illumination such as the one in this study. When no motion or very limited motion is present, the HR can be obtained directly from the raw grayscale intensity from the ToF camera, as is shown in Figure 4-5a, during which the participant is asked to remain as still as possible. However, in more realistic scenarios, when the users are behaving naturally, there will inevitably be more motion artifacts present in the raw intensity data (Figure 4-5b). Such motion artifacts are especially obvious in our system where active illumination from a point source is used. Intensity changes caused by the user moving closer or further from the light source can be many times stronger than the underlying heartbeat signal, leading to erroneous HR measurements (Figure 4-5b).

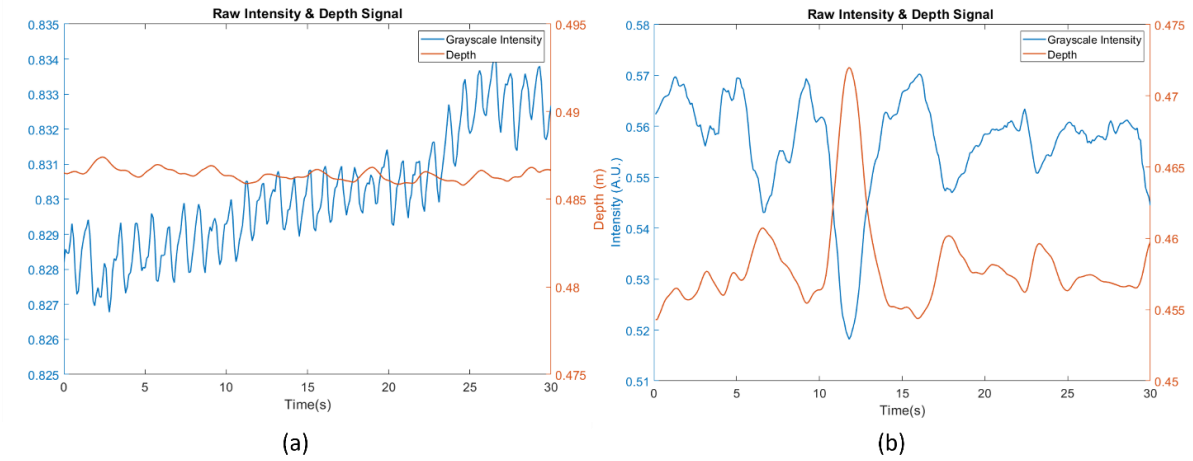


Figure 4-5 (a) Raw intensity signal and depth signal from ROI-1 when participants are intentionally staying still. The grayscale intensity shows clear HR signal (b) Raw intensity signal and depth signal from ROI-1 when motion artifact is present. The grayscale intensity is dominated by motion induced artifacts

Therefore, in this study, depth information is used to compensate for the intensity variation caused by motion artifacts. The underlying logic in the motion artifacts compensation is three-fold: First, because active illumination from a point source is used, the change of grayscale intensity is nonlinearly correlated to the relative position between the head and the camera. Secondly, the depth information recorded by the ToF camera should contain no HR component since the micromotion created by the heartbeat is too small to be measured by the ToF camera. Lastly, after the motion artifacts are removed, the compensated intensity information should have minimum correlation with the depth information. In other words, the motion compensation is achieved when the relationship in equation 4.1 is satisfied, where I_{comp}, I_{raw} and D_{raw} are compensated grayscale intensity, raw intensity, and raw depth signal from ROI-1 respectively. a is the linear coefficient and b is the nonlinear coefficient that minimize the correlation between D_{raw} and $\frac{I_{raw}}{a*(D_{raw})^b}$:

$$I_{comp} = \frac{I_{raw}}{a*(D_{raw})^b} \ , \ a, b = arg\min_{a,b} C\left(\frac{I_{raw}}{a*(D_{raw})^b} \ , D_{raw}\right) \qquad [4.1]$$

Ideally, the intensity variation caused by the distance variation between the participants' faces and the light source should be inversely proportional to the square of the distance variation (i.e., inverse square law of light propagation). However, skin conditions as well as the illumination angle change from person to person [35,36] and we found that different values of the nonlinear coefficients are needed to minimize the correlation between the D_{raw} and $\frac{I_{raw}}{a*(D_{raw})^b}$ across different participants. In this study, the ranges of both linear and nonlinear coefficients are set between 0.1 to 5.

Based on the above logic, we compensate for the motion artifact and extract HR using the following method (Fig. 4-6): (a) ROI-1 is defined and tracked in all frames using a Kanade–Lucas–Tomasi feature tracker; (b) the intensity across pixels within ROI-1 is averaged; (c) by using the relationship described in equation 1, we iteratively calculate the compensated intensity I_{comp} until the minimum correlation between the depth signal D_{raw} and I_{comp} is reached; (d) a bandpass filter between 40 BPM and 150 BPM (which is the common resting HR range) is applied to the compensated signal I_{comp} ; (e) a Fourier transform of the data is taken on the motion compensated intensity signal I_{comp} to find the HR, where HR is determined as the frequency component with the highest amplitude. In this study, we compare the performance of the motion compensated HR results against the results that "do not use the motion compensation". The results that "do not use motion compensation" refers to HR reading derived using the same steps above except for the step of using the depth information to compensate for the motion artifacts.

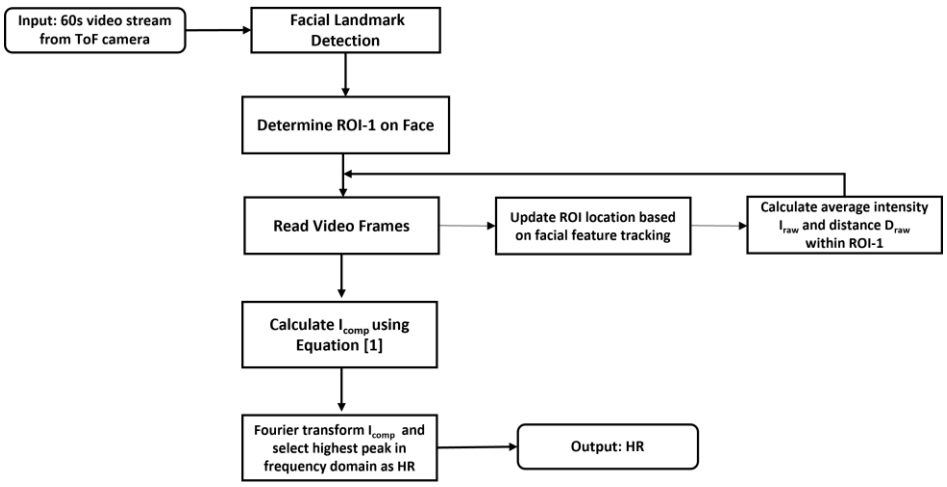


Figure 4-6 HR extraction process from the 3D video streams of a ToF camera

RR extraction is more straightforward as we directly measure the chest wall movement from respiration using the depth signal from the chest region. Specifically, RR is extracted using the following steps (Fig.4-7): (a) ROI-2 is defined and tracked in all frames (b) calculate the average depth across all pixels within ROI-2. (c) Apply Fourier transform to the depth signal and apply bandpass filter between 5 BPM to 30 BPM to find the highest peak as the RR value.

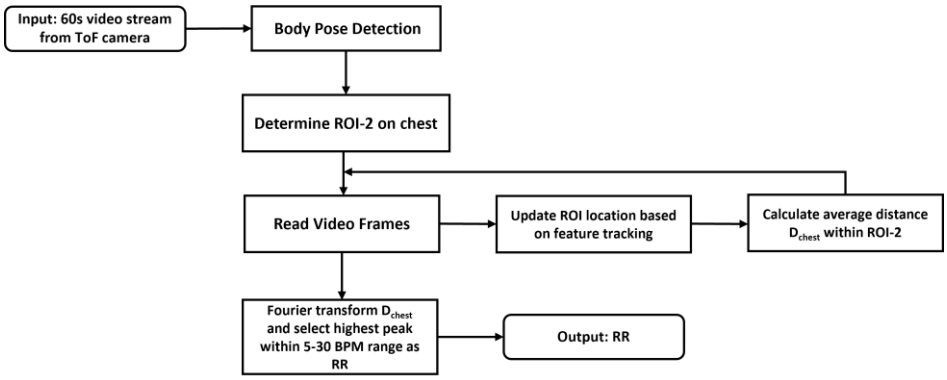


Figure 4-7 RR extraction process from the 3D video streams of a ToF camera

To test the effectiveness of the HR/RR monitoring system, 29 participants from varying demographics were recruited in the study so that performance among different skin colors, genders, and ages could be compared. The study is approved by the Institutional Review Board at the University of Michigan and informed consent was obtained from every participant. Since

the absorption of melanin is well known and should be repeatable even among participants of different skin color, a smaller number of participants within each skin color group should be enough to reflect the system performance over different skin colors. In this study, the 29 participants were classified as either lighter skin color group or darker skin color group based on their Fitzpatrick skin type, a numerical classification for skin type based on a self-reported questionnaire [38]. Participants with skin type I–III were classified into the lighter skin color group, while participants with skin type IV–VI were classified into the darker skin color group. A total of 17 participants in this study were within the lighter skin color group, while the remaining 12 participants were considered as being within the darker skin color group. In terms of gender, 18 participants were male and 11 participants female. As for age, we recruited participants from 18 years old to 72 years old. All participants were divided into groups older than 35 years old and younger than 35 years old. In this study, 8 participants were older than 35 years old and the remaining 21 participants were younger than 35 years old. The demographics of the participants are shown in Table 3. To make up for the smaller number of participants to reach more representative data, A total of 10 60 s videos at 10 frames per second are obtained from each participant. To mimic the real-world scenario, participants were asked to sit in front of the camera and are allowed to move as they see comfortable (such as leaning backward/forward) but they were asked to look toward the camera during the measurements. Among the 290 measurements, 4 measurements were excluded in the study due to the failure of the face recognition algorithm to identify the regions of interest (ROIs). In the end, 286 measurements were used in the study.

Table 4-2 Demographics of the participant population

Group:	Number of Participants		Age Range		Skin Type Range	
	29		18–72 years		II–IV	
Subgroup:	(Female	Male)	(<= 35 years	>35 years)	(I–III	IV–VI)
	11	18	21	8	17	12

4.4 Experiment Results

The raw and processed data from the two ROIs are illustrated in Figures 4-8 and 4-9. Figure 4-8 shows a 30 s segment of a typical 60 s recording of both the raw intensity and depth signal for ROI-1. The second row corresponds to the raw intensity information and the bottom row corresponds to the depth information from the same ROI-1. In ROI-1, the maximum motion from ROI-1 to the camera is as large as 15 cm. As a result, the raw intensity data is strongly inversely correlated to the depth information from the same ROI, suggesting that the raw signal is dominated by the motion artifacts. The grayscale intensity after motion compensation is shown on the top row of Figure 4-8 where most of the motion artifacts in the depth information are removed. From the time-domain signal, the HR signal becomes recognizable compared to the motion-dominated raw signal. The effect of the motion artifacts as well as the benefits of depth-based motion compensation is also evident in the frequency domain. When comparing the frequency domain signal of the raw intensity and the depth signal, we can see the two spectra are similar to each other in shape, and they also share many common lower frequency components. Even though a weak frequency peak near the reference HR of 83 BPM can be seen, it is overshadowed by the frequency component from the motion artifacts. After the motion compensation, we can see that in the frequency domain signal of the compensated signal (Figure 4-8b, top), these artifact frequencies are suppressed and a clear HR frequency near 83 BPM can be seen in the compensated spectrum.

As for the RR measurement, Figure 4-9 shows a typical depth signal from the ROI-2 (chest) region corresponding to a RR of 9 BPM. The amplitude of chest wall displacement caused by the respiration motion is approximately 4 mm. Because of this small amplitude, such motion could be affected by other factors such as overall body motion as well the blockage of clothing. Some potential solutions to mitigate these issues will be discussed in the discussion section.

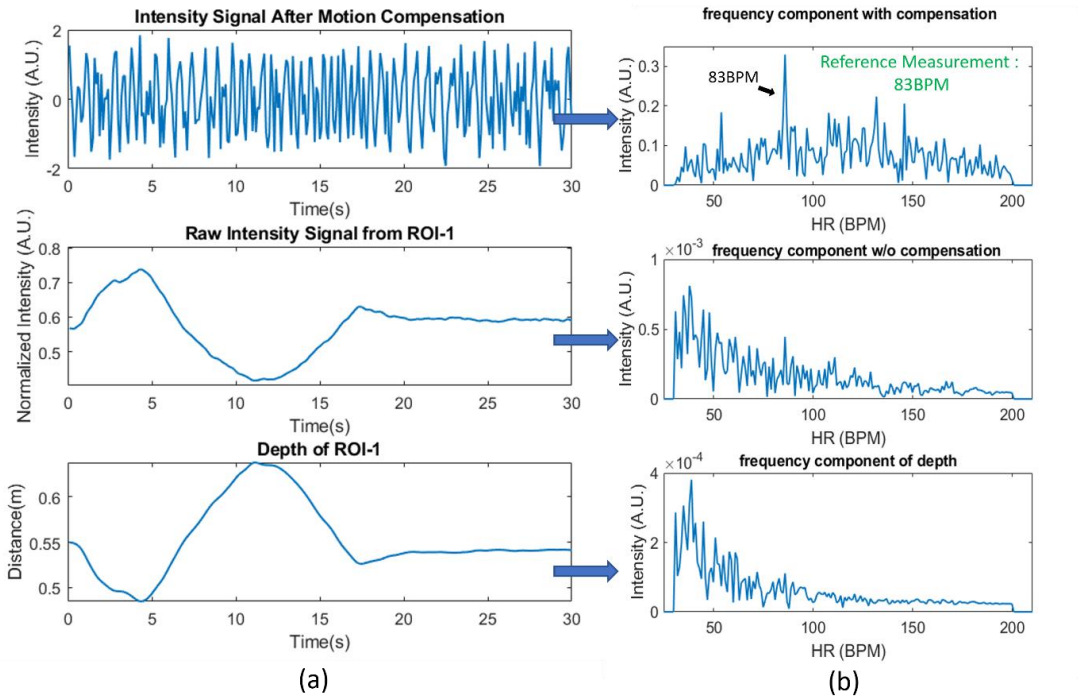


Figure 4-8 (a) Time domain signal for HR extraction: HR signal after motion compensation (top), raw grayscale signal(middle) and raw depth signal (bottom). (b) Frequency domain HR signal: with motion-compensation (top), without motion compensation (bottom)

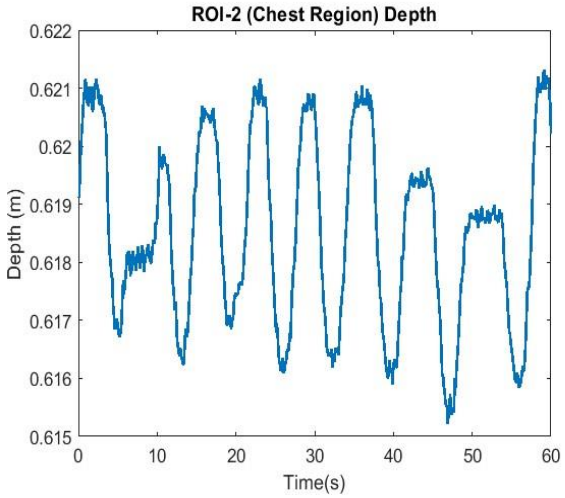


Figure 4-9 ROI-2 (chest) region depth signal, showing the periodic chest wall movement from respiration. The amplitude of the chest wall movement is 4 mm

The pilot human study with 29 participants illustrates the improvement in overall performance achieved for the HR measurements by using depth information compensation. In the study, the mean HR reading during the 60 s of measurement is considered as the ground truth and the "correct measurement" from our system is defined as a HR measurement that is within 10 percent of the ground truth. The top bar graph in Figure 4-10 demonstrates the distribution of measurement error rate after compensation, while the bottom bar graph demonstrates the distribution of measurement error rate without depth compensation. With depth information used to compensate for motion artifacts, 75% of the HR measurements (214 out of 286 measurements) are correct. On the other hand, without compensation, only 35% of the HR measurements (100 out of 286 tests) are correct. It is also worth noticing that with motion compensation, many of the erroneous measurements are below 30% error rate, as compared to between 50 and 60% for the uncompensated case.

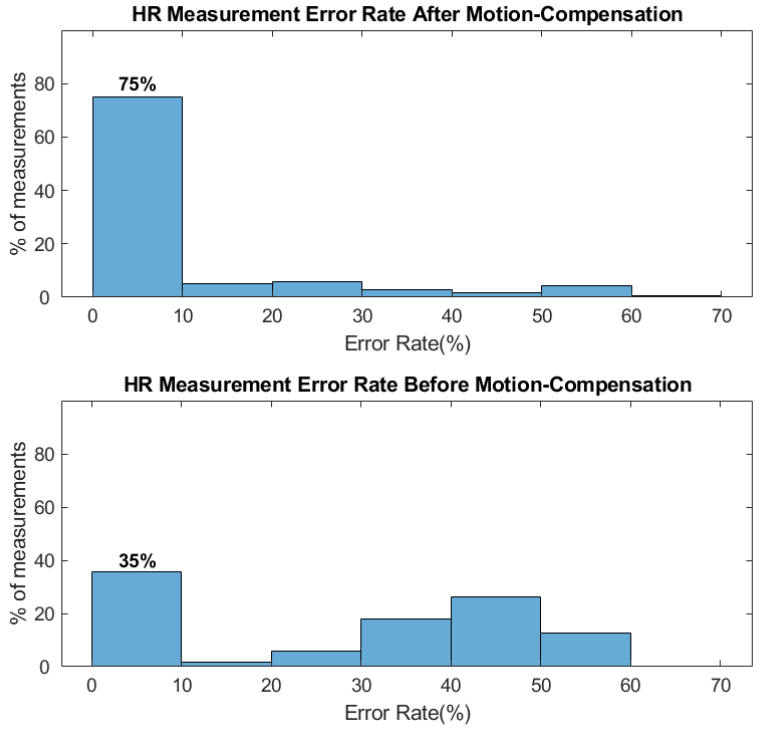


Figure 4-10 HR measurements error rate on all 286 measurements with motion compensation (top) and without motion compensation (bottom)

To analyze the agreement between the reference device (finger pulse oximeter) against our system, we plot the Bland–Altman plot for the HR from the 29-participant study in Figure 4-11. The left plot illustrates the results with motion compensation, and the right plot illustrates the results without using motion compensation. The x-axis is the average HR reading of the reference oximeter and our ToF-based system, while the y-axis is the deviation of the HR measured in the ToF system from the reference oximeter reading. With compensation, the mean value of the deviation is −6.25 BPM, and 95% of the deviation falls within +/− 35 BPM of the mean deviation. In contrast, without compensation the mean value of the deviation is 21 BPM, and 95% of the deviation falls within +/− 36 BPM of the mean deviation. The large standard deviation rises from the extreme erroneous values of the measurement system. These extreme values rise from camera noises as well as intensity artifacts that are not reflected in the depth signal. After the dominating motion artifacts are removed, the system could wrongly pick up

these artifacts as HR. This also explains why the wrong measurements of the uncompensated signal groups around the top left corner of the plot since the dominating motion artifacts are typically at a lower frequency compared to HR. Additionally, because the motion artifacts are likely to be mistakenly picked as HR, it also leads to the seemingly small standard deviation of errors for the uncompensated HR measurements.

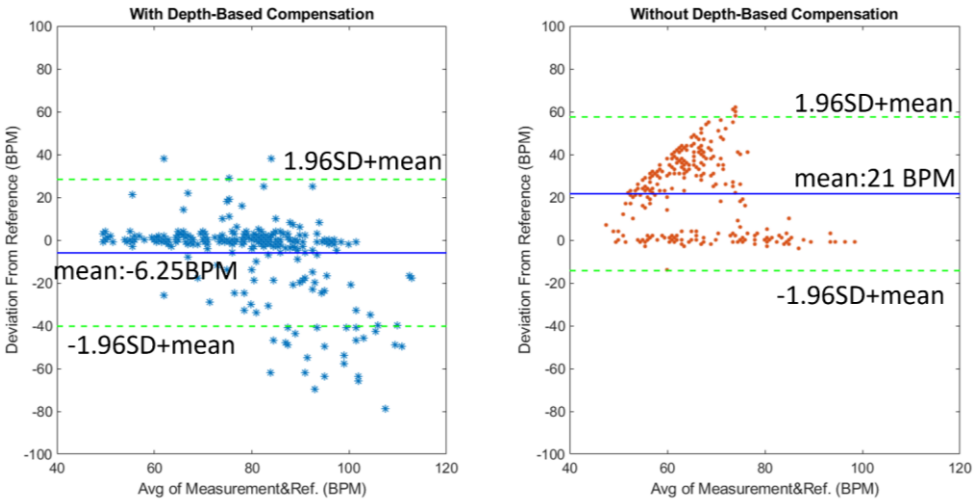


Figure 4-11 Bland-Altman plot for HR measurements on all 286 measurements with motion compensation (left) and without motion compensation (right)

The RR measurements are also examined for the pilot study of 29 participants. Figure 4-12 shows the percentage of 286 ToF-based RR measurements that fall into different bins of deviation from the reference Masimo pulse oximeter. The mean deviation from the reference reading is found to be 1.7 BPM while 60% of measurements are within +/− 2 BPM from the reference RR measurements. However, in our measurements, we can also sometimes see deviation as large as 10 BPM, these errors can be attributed to large body motion as well as the loose clothing that the participants are wearing. Some examples will be discussed in the discussion section.

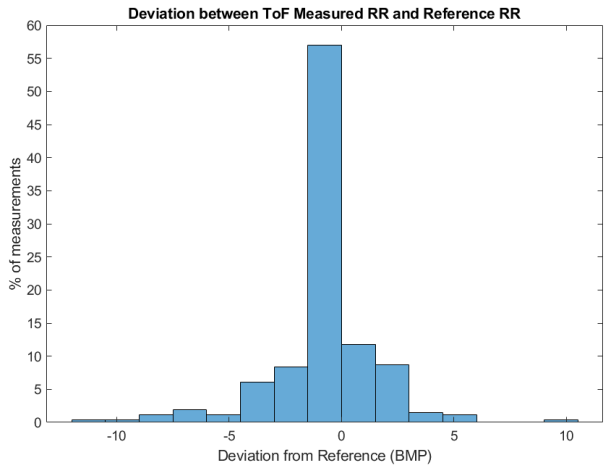


Figure 4-12 Percentage of ToF based RR measurements versus deviation from reference oximeter

4.4.1 HR Measurement vs Motion Artifacts

To compare the performance between distance compensated and non-distance compensated HR measurements against different levels of motion, we plot the percentage of correct measurements versus a motion score (Figure 4-13). The blue bars are for the HR data with compensation, while the red bars are for the HR data without depth information compensation. In this study, we define motion score as the standard deviation of the mean depth change of the ROI-1 to the optical center of the camera, where depth change is calculated as the difference between depth D_{raw} of ROI-1 and the mean depth of ROI-1 over the 60 s measurement.

$$Motion\ Score = Std(Abs(depth_{ROI-1}) - mean(depth_{ROI-1})) \quad [4\text{-}2]$$

Since the motion in real-life situations can sometimes be of an irregular pattern, the motion score defined in this study reflects amplitude and frequency of a participant's motion. The higher the motion score, the larger and more frequent the motion artifacts are. For example, a motion score below 0.3 cm is typical of a participant sitting still, while a motion score above 1 cm is typical of participants adjusting for a comfortable position e.g., sitting restlessly while sitting. It is worth noticing that a motion score of 1 cm does not necessarily mean the participant

moves only 1 cm during the measurements. For example, in a measurement with a motion score of 1 cm, the maximum ROI-1 deviation from the mean position can exceed 4 cm. The blue bars are for the HR measurements with compensation, while the red bars are for the HR measurements without depth information compensation. As can be seen from the plot, the performance of the motion-compensated HR measurements outperforms the uncompensated measurements across every motion score category. Even when small motion is introduced (motion score from 0 to 0.3 cm), the distance-compensated HR measurement outperforms the uncompensated measurement by more than 75% in terms of success rate. Once the motion becomes larger, the performance of the uncompensated HR measurement plummets, indicating that the raw signal is dominated by motion artifacts. At the same time, the success rate of the motion-compensated HR also drops, but to a lesser extent. For example, when motion score exceeds 0.9 cm, ~35% of compensated measurements are correct meanwhile close to none of the uncompensated HR measurements are correct. This is of great significance because motion artifacts are a dominant source of noise in contactless HR measurement, especially with near-infrared wavelength where the absorption of blood is much weaker. We believe the performance of the ToF-based HR measurement system under larger motion could be improved with future development of both the motion compensation model as well as higher performance ToF cameras. We will discuss such future developments in more detail in the discussion section.

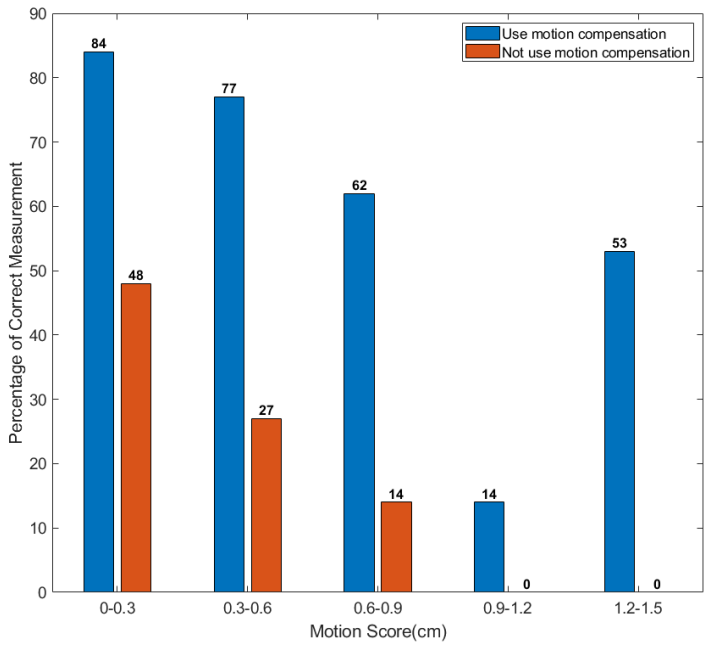


Figure 4-13 Percentage of correct HR measurement within each motion score category

4.4.2 Different Skin Color

One of the challenges for an RGB-based HR/RR monitoring system is that different skin colors could affect the signal quality because of strong melanin absorption in the visible wavelength range [18]. In contrast, the absorption of melanin is much lower at near-infrared, which allows the ToF-based system to perform more uniformly among demographics of different skin colors. Figure 4-14 shows the error rate of the HR measurements among participants with darker skin color and lighter skin color. Participants with Fitzpatrick skin type I–III (17/29 participants) are considered as light skin color, while participants with skin type IV–VI (12/29 participants) are considered as darker skin color. Among the lighter skin color group, the percentage of success rate measurement is 74% with the mean deviation of the measurements being −6.1 BPM. As for the darker skin color group, the same success rate of 74% is achieved with the mean deviation from the reference at −5.8 BPM.

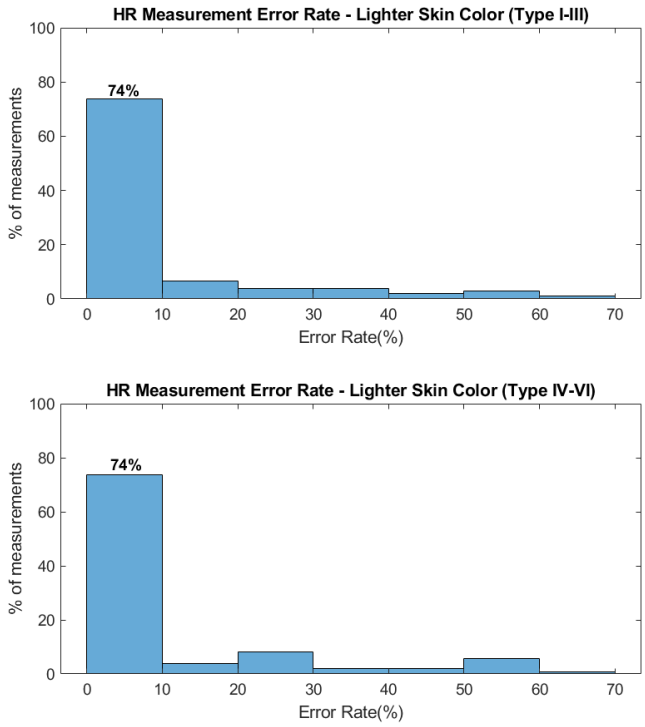


Figure 4-14 HR measurements error rate within groups of: lighter skin color(top) and darker skin color

Similar performance among two skin color groups is also evident when we examine the Bland–Altman plot in Figure 4-15. Both the mean deviation (−6.1 BPM for the lighter skin color versus −5.8 BPM for darker skin color) and the 95% percentile range (+/− 35 BPM for the lighter skin color versus +/− 33 BPM for darker skin color) are very similar between the two groups. Moreover, deviation distribution is also similar among the two groups, indicating that the ToF system used in this study performs equally well among participants of different skin colors. Thus, using near-infrared illumination, we are able to achieve performance independent of skin color.

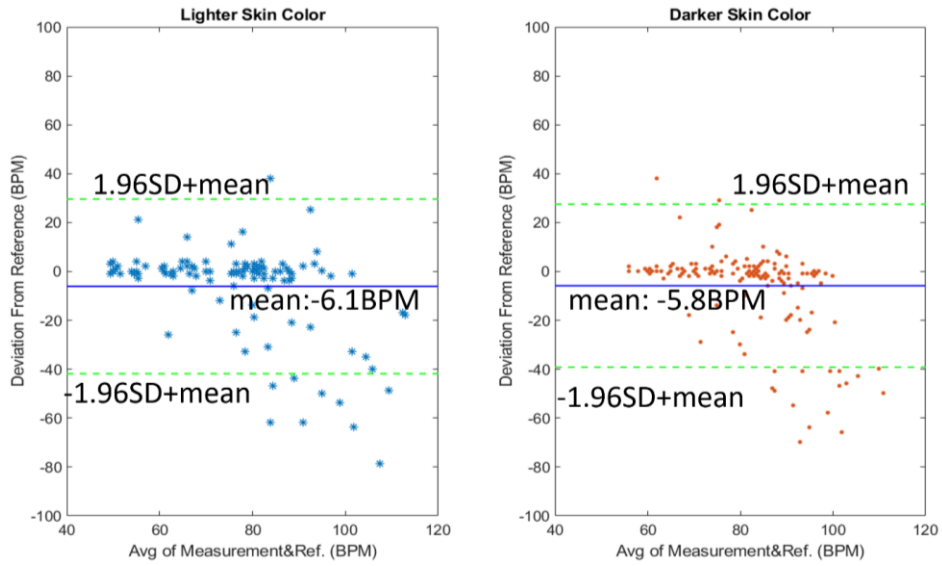


Figure 4-15 Bland-Altman plot for HR measurements within groups of: lighter skin color(left) and darker skin color (right)

4.4.3 Different Gender and Age

We also investigate the performance of the ToF-based HR measurements system in terms of the participant's gender and age. Similar to the RGB camera-based system, no significant performance difference is seen among participants of different gender and age. Figure 4-16 shows the success percentage rate among participants of different gender, we achieve a 77% success rate in the male group and a 72% success rate in the female group. The mean HR deviation from reference is −5.6 BPM for the male group (18/29 participants) and −7.2 BPM for the female group (11/29 participants) (Figure 4-17), respectively. Even though the mean deviation differs slightly, the pattern of deviation data points looks similar. Such differences may be attributed to different skin conditions or even different skincare products used on the skin. Even though participants are asked not to use makeup, there could still be residuals left on the participant's face. Since the blood absorption at infrared is already low, any further decrease of signal could affect the success rate of the HR measurements.

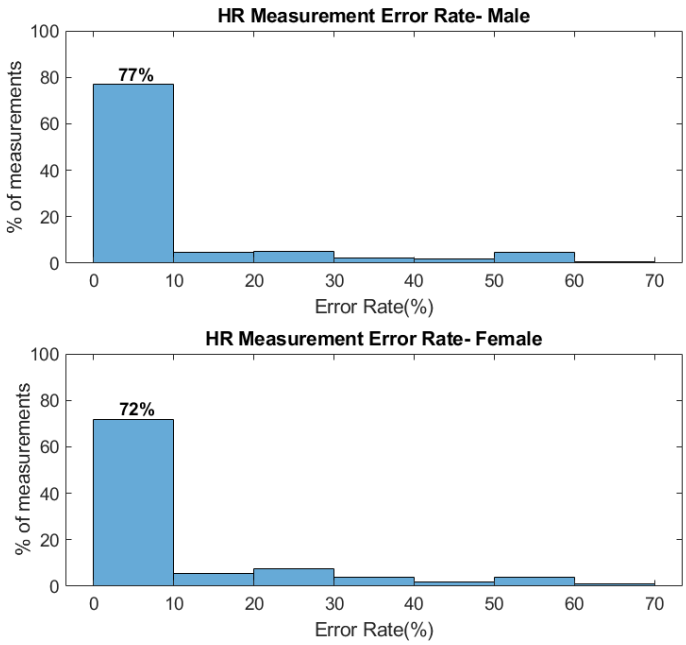


Figure 4-16 HR measurements error rate within groups of: male (top) and female (bottom)

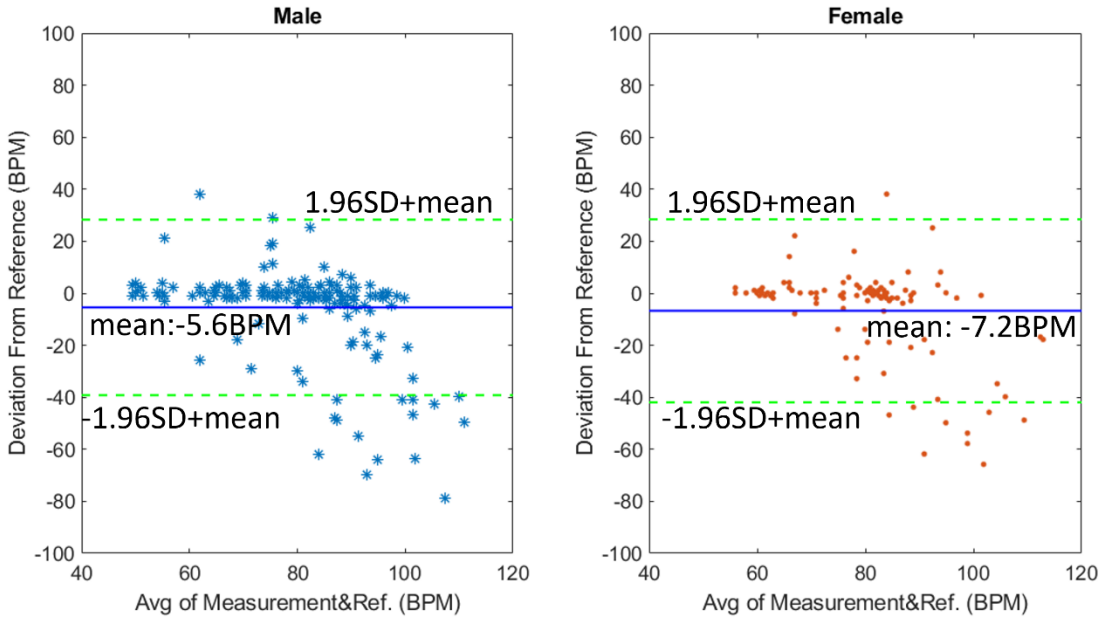


Figure 4-17 Bland-Altman plot for HR measurements within groups of: male (left) and female (right)

In terms of age, we separated the participants into a younger group (21/29 participants) and an elder group (8/29 participants) at the threshold of 35 years old. The success rate/mean deviation is 84%/−7.7 BPM for the elder group and 71%/−5.89 BPM for the younger group

(Figures 4-18 and 4-19). The higher success rate among the elder participants could be caused by elder participants staying more still during the measurements compared to younger participants. In fact, the mean motion score for the younger group is 0.61 cm, compared to 0.47 cm for the elder groups. As we discussed before, the success rate deteriorates as the motion score increases, which could explain the higher success rate among elder participants.

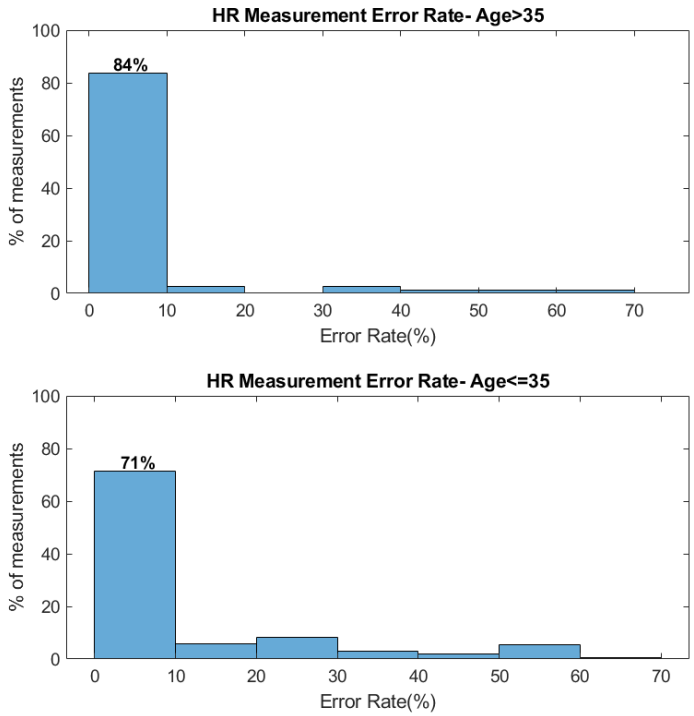


Figure 4-18 HR measurements error rate within groups of: age>35 (top) and age<=35 (bottom)

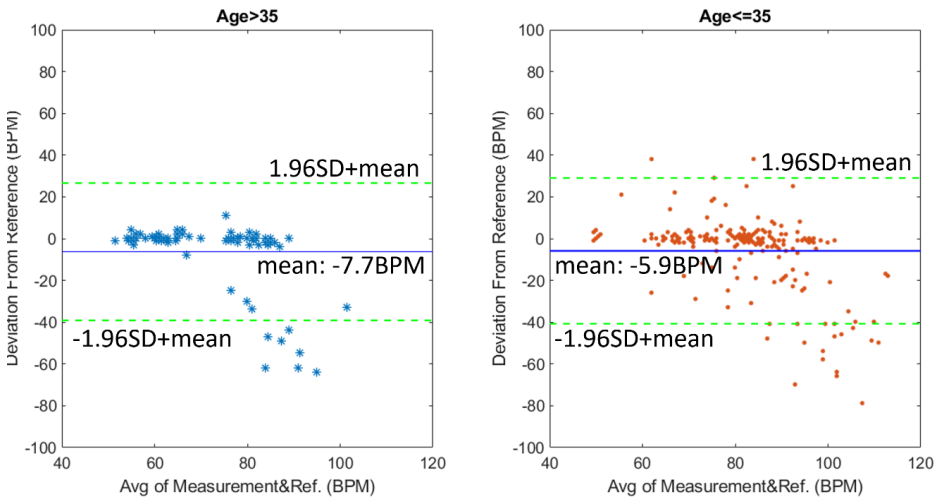


Figure 4-19 Bland-Altman plot for HR measurements within groups of: age>35 (left) and age<=35 (right)

4.5 Discussion

Even though the additional depth information from the ToF-based HR/RR measurements system shows benefits in terms of motion compensation and RR measurements, we also noticed several external factors that can affect the performance, which could help with the future improvement of the system's performance if addressed.

4.5.1 Limitation of RR measurements

In this study, the RRs are acquired by directly measuring the displacement of the chest wall during respiration. In reality, it is often the case when the users' bodies are involuntarily moving while the system is measuring the RR. Therefore, similar to the HR measurement, the RR measurement could also suffer from motion-induced artifacts. Even though such an issue is less pronounced in this study as the participants are asked to sit in front of the camera, we still discuss possible methods to mitigate the effects of body motion that is unrelated to respiration. Since the neck region usually moves with the chest but does not show a strong respiration motion, we could use the depth signal on the neck as a reference region to separate the respiration motion from other body motions. Therefore, we could view the depth signal from the chest region as a

superposition of the general body motion and the chest wall motion from respiration. A blind source separation method such as Independent Component Analysis (ICA) can then be applied to the raw depth signals to extract the respiration motion. For example, Figure 4-20a shows the raw depth signal from the neck and chest region, respectively. The depth signal from the neck region records mainly the motion of the body since respiration does not cause significant muscle contraction on the neck. As a comparison, the signal from the chest region (Figure 4-20a bottom figure) is also affected by the overall body motion as the periodic chest wall motion from respiration is masked. The signal after ICA separation is shown in Figure 4-20b. A clear pattern of the chest wall moving back and forth from the respiring motion can now be seen in the top row of the separated signal. The respiratory rate, derived from the first component in Figure 4-20, is measured as 15 BPM, while the reference pulse oximeter also measures 15 BPM.

It is also worth noticing that since the method of acquiring the RR relies on directly measuring chest wall movement, any type of clothing, such as a loose sweatshirt or down jacket, which obfuscates the chest wall movement, will prevent the system from acquiring RR. To overcome this limitation, some complementary methods such as deriving RR from HR variability or using a thermal sensor to measure RR can be used in combination with the ToF camera to provide RR measurements in more versatile environments [5,7,26,27].

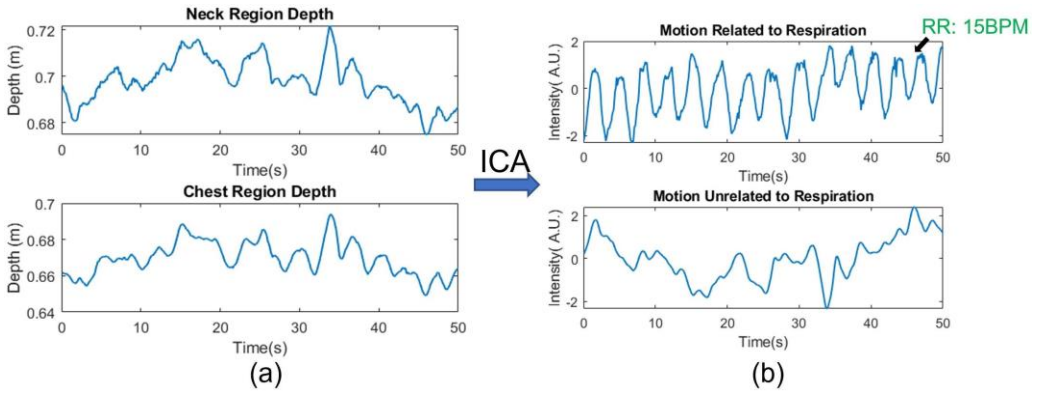


Figure 4-20 (a) Time domain signal for RR extraction: Raw depth signal from neck region not containing RR motion (top), raw depth signal from chest region containing RR motion (bottom). (b) Depth signal after ICA separation: Signal component with RR motion (top), signal component without RR motion compensation (bottom)

4.5.2 Limitation of motion compensated HR measurement using ToF camera

The results of the pilot human study suggest that the magnitude of motion contributes the most to the failure of the HR measurements. When the motion score is relatively small (<0.3 cm), the success rate is 84% while such success rate falls quickly as the motion score increases. The adverse effects of larger motion to the HR measurements seem intuitive as it both makes the ROIs harder to track as well as creates larger intensity artifacts for the ToF camera to compensate. However, there are also some less noticeable factors that can also contribute to the erroneous reading even when the motion artifacts are small.

To obtain a stable signal from a ROI, the ROIs needs to be stably and accurately tracked in every frame. In some cases, reflective spots on the face as well as the changing head pose/facial expression could introduce artifacts to the tracked ROI. For example, we find that the light reflection from the participants' eyes combined with the blinking motion can sometimes cause the positions of the ROI to jitter, even though the participants are not moving at that time. If such artifacts are present during measurement, it can mislead the system to take the blinking frequency as HR.

In terms of the limitation of the depth-based motion compensation, other than the obvious cases where significant motion overwhelms the underlying HR signal, we also find the system performance degrading when local motions, such as involuntary muscle twitches or facial expression changes [6,10], are present. Since the human face is not a rigid body, these local motions can cause intensity artifacts without inducing a change in depth signal at the same time, making them "invisible" to the depth-based motion compensation.

Therefore, the depth signal-based method is more effective toward motion artifacts that induce depth variations that are large enough to be captured by the ToF camera. As an example, global motions, especially scaling and translational motion, can be easily captured by the ToF camera. Even though these larger motions cause large grayscale intensity changes on the ToF camera, they can be effectively removed to prevent them from affecting HR measurement.

4.5.3 Future Improvements

Based on the previous discussion, we believe that the system performance can be further improved by building a more precise model to compensate for motion-induced artifacts and by developing ToF cameras with higher resolution and frame rate. The model we use in this study to compensate for the intensity change caused by motion is relatively coarse as we only consider the average depth change within a larger ROI. If a model can be developed to further utilize the point cloud generated by the ToF camera to take more subtle movements such as head rotation/tilting into consideration, it would expand the types of motion artifacts that the CVSM system can compensate. At the same time, efforts are made to develop an indirect ToF camera with a higher resolution and frame rate [39]. Higher camera resolution could be useful in improving the ROI tracking performance of the system while a higher frame rate would allow the system to capture the motion of higher frequency without aliasing or motion blur. In addition,

to compensate for micro-motion that is not captured by the depth signal, other signal processing techniques such as sparse frequency estimation could be combined with our depth-based motion compensation method to improve the motion artifacts resilience of the system.

4.6 Conclusion

In conclusion, we demonstrate a contactless HR/RR monitoring system based on an indirect ToF camera. The active illumination from an 850 nm VCSEL combined with the depth information from the ToF camera can be used to compensate for the motion artifacts that commonly dominate the underlying heartbeat signal. We show that the depth-based compensation increases success rate (defined as the HR reading within 10% of the reference HR measurement) to 75%, as compared to 35% when no depth compensation method is used. The additional depth information also enables the direct measurement of RR from a participant by measuring the chest wall movement during breathing. The RR measurement from our system shows a mean deviation of 1.7 BPM compared to the reference RR reading. Furthermore, the infrared active illumination makes this system less affected by factors such as environmental lighting or the skin color of the user. In our pilot study with 29 participants, we show that our system performs similarly among participants of different demographics such as skin color, age, and gender. In the future, this system could be found useful in fields such as in-cabin driver monitoring and remote patient monitoring where non-contact unobtrusive and environmentally agnostic physiological monitoring is preferred [19,23,40,41].

Reference

[1] Verkruysse, W.; Svaas, L.O.; Nelson, J.S. Remote plethysmographic imaging using ambient light. Opt. Express 2008, 16, 21434–21445.

[2] Huang, P.W.; Wu, B.J.; Wu, B.F. A heart rate monitoring framework for real-world drivers using remote photoplethysmography. IEEE J. Biomed. Health Inform. 2020, 25, 1397–1408.

[3] Balakrishnan, G.; Dur, F.; Guttag, J. Detecting pulse from head motions in video. In Proceedings of the IEEE Conference on Computer Vision and Pattern Recognition, Portland, OR, USA, 23–28 June 2013.

[4] Cheng, J.; Chen, X.; Xu, L.; Wang, Z.J. Illumination variation-resistant video-based heart rate measurement using joint blind source separation and ensemble empirical mode decomposition. IEEE J. Biomed. Health Inform. 2016, 21, 1422–1433.

[5] Negishi, T.; Abe, S.; Matsui, T.; Liu, H.; Kurosawa, M.; Kirimoto, T.; Sun, G. Contactless vital signs measurement system using RGB-thermal image sensors and its clinical screening test on patients with seasonal influenza. Sensors 2020, 20, 2171.

[6] Kumar, M.; Veeraraghavan, A.; Sabharwal, A. DistancePPG: Robust non-contact vital signs monitoring using a camera. Biomed. Opt. Express 2015, 6, 1565–1588.

[7] Sun, G.; Nakayama, Y.; Dagdanpurev, S.; Abe, S.; Nishimura, H.; Kirimoto, T.; Matsui, T. Remote sensing of multiple vital signs using a CMOS camera-equipped infrared thermography system and its clinical application in rapidly screening patients with suspected infectious diseases. Int. J. Infect. Dis. 2017, 55, 113–117.

[8] Unursaikhan, B.; Tanaka, N.; Sun, G.; Watanabe, S.; Yoshii, M.; Funahashi, K.; Sekimoto, F.; Hayashibara, F.; Yoshizawa, Y.; Choimaa, L.; et al. Development of a Novel Web Camera-

Based Contact-Free Major Depressive Disorder Screening System Using Autonomic Nervous Responses Induced by a Mental Task and Its Clinical Application. Front. Physiol. 2021, 12, 706.

[9] Wang, W.; den Brinker, A.C.; Stuijk, S.; De Haan, G. Algorithmic principles of remote PPG. IEEE Trans. Biomed. Eng. 2016, 64, 1479–1491.

[10] Wang, W.; Stuijk, S.; De Haan, G. Exploiting spatial redundancy of image sensor for motion robust rPPG. IEEE Trans. Biomed. Eng. 2014, 62, 415–425.

[11] de Haan, G.; Jeanne, V. Robust pulse rate from chrominance-based rPPG. IEEE Trans. Biomed. Eng. 2013, 60, 2878–2886.

[12] Wang, W.; Stuijk, S.; De Haan, G. A novel algorithm for remote photoplethysmography: Spatial subspace rotation. IEEE Trans. Biomed. Eng. 2016, 63, 1974–1984.

[13] De Haan, G.; Van Leest, A. Improved motion robustness of remote-PPG by using the blood volume pulse signature. Physiol. Meas. 2014, 35, 1913.

[14] Wu, B.F.; Huang, P.W.; Lin, C.H.; Chung, M.L.; Tsou, T.Y.; Wu, Y.L. Motion resistant image-photoplethysmography based on spectral peak tracking algorithm. IEEE Access 2018, 6, 21621–21634.

[15] Feng, L.; Po, L.M.; Xu, X.; Li, Y.; Ma, R. Motion-resistant remote imaging photoplethysmography based on the optical properties of skin. IEEE Trans. Circuits Syst. Video Technol. 2014, 25, 879–891.

[16] Aoxin, N.; Azarang, A.; Kehtarnavaz, N. A Review of Deep Learning-Based Contactless Heart Rate Measurement Methods. Sensors 2021, 21, 3719.

[17] Zaunseder, S.; Trumpp, A.; Wedekind, D.; Malberg, H. Cardiovascular assessment by imaging photoplethysmography—A review. Biomed. Eng. Tech. 2018, 63, 617–634.

[18] Zonios, G.; Dimou, A.; Bassukas, I.; Galaris, D.; Tsolakidis, A.; Kaxiras, E. Melanin absorption spectroscopy: new method for noninvasive skin investigation and melanoma detection. J. Biomed. Opt. 2008, 13, 014017.

[19] Gastel, V.; Stuijk, M.S.; de Haan, G. Motion robust remote-PPG in infrared. IEEE Trans. Biomed. Eng. 2015, 62, 1425–1433.

[20] Yu, S.; Hu, S.; Azorin-Peris, V.; Chambers, J.A.; Zhu, Y.; Greenwald, S.E. Motion-compensated noncontact imaging photoplethysmography to monitor cardiorespiratory status during exercise. J. Biomed. Opt. 2011, 16, 077010.

[21] Magdalena, N.E.; Marks, T.K.; Mansour, H.; Veeraraghavan, A. SparsePPG: Towards driver monitoring using camera-based vital signs estimation in near-infrared. In Proceedings of the IEEE Conference on Computer Vision and Pattern Recognition Workshops, Salt Lake City, UT, USA, 18–22 June 2018.

[22] Perdue, K.L.; Westerlund, A.; McCormick, S.A.; Nelson, C.A., III. Extraction of heart rate from functional near-infrared spectroscopy in infants. J. Biomed. Opt. 2014, 19, 067010.

[23] Blanik, N.; Heimann, K.; Pereira, C.; Paul, M.; Blazek, V.; Venema, B.; Orlikowsky, T.; Leonhardt, S. Remote vital parameter monitoring in neonatology–robust, unobtrusive heart rate detection in a realistic clinical scenario. Biomed. Eng. Tech. 2016, 61, 631–643.

[24] Nahler, C.; Feldhofer, B.; Ruether, M.; Holweg, G.; Druml, N. Exploring the usage of Time-of-Flight Cameras for contact and remote Photoplethysmography. In Proceedings of the 2018 21st Euromicro Conference on Digital System Design (DSD), Prague, Czech Republic, 29–31 August 2018.

[25] Kranjec, J.; Beguš, S.; Geršak, G.; Drnovšek, J. Non-contact heart rate and heart rate variability measurements: A review. Biomed. Signal Process. Control 2014, 13, 102–112.

[26] van Gastel, M.; Stuijk, S.; de Haan, G. Robust respiration detection from remote photoplethysmography. Biomed. Opt. Express 2016, 7, 4941–4957.

[27] Charlton, P.H.; Bonnici, T.; Tarassenko, L.; Clifton, D.A.; Beale, R.; Watkinson, P.J. An assessment of algorithms to estimate respiratory rate from the electrocardiogram and photoplethysmogram. Physiol. Meas. 2016, 37, 610–626.

[28] Bernacchia, N.; Scalise, L.; Casacanditella, L.; Ercoli, I.; Marchionni, P.; Tomasini, E.P. Non-contact measurement of heart and respiration rates based on Kinect™. In Proceedings of the 2014 IEEE International Symposium on Medical Measurements and Applications (MeMeA), Lisboa, Portugal, 11–12 June 2014.

[29] Procházka, A.; Schätz, M.; Vyšata, O.; Vališ, M. Microsoft Kinect visual and depth sensors for breathing and heart rate analysis. Sensors 2016, 16, 996.

[30] Zanuttigh, P.; Marin, G.; Dal Mutto, C.; Dominio, F.; Minto, L.; Cortelazzo, G.M. Time-of-Flight and Structured Light Depth Cameras; Technology and Applications; Springer: Cham, Switzerland, 2016.

[31] Martinez, L.F.; Paez, G.; Strojnik, M. Optimal wavelength selection for noncontact reflection photoplethysmography. In Proceedings of the 22nd Congress of the International Commission for Optics: Light for the Development of the World, Puebla, Mexico, 15–19 August 2011; International Society for Optics and Photonics: Bellingham, WA, USA, 2011; Volume 8011.

[32] Moço, A.V.; Stuijk, S.; de Haan, G. New insights into the origin of remote PPG signals in visible light and infrared. Sci. Rep. 2018, 8, 1–15.

[33] Asthana, A.; Zafeiriou, S.; Cheng, S.; Pantic, M. Incremental face alignment in the wild. In Proceedings of the IEEE Conference on Computer Vision and Pattern Recognition, Columbus, OH, USA, 23–28 June 2014.

[34] Zhu, X.; Ramanan, D. Face detection, pose estimation, and landmark localization in the wild. In Proceedings of the 2012 IEEE Conference on Computer Vision and Pattern Recognition, Providence, RI, USA, 16–21 June 2012.

[35] So-Ling, C.; Li, L. A multi-layered reflection model of natural human skin. In Proceedings of the Computer Graphics International 2001, Hong Kong, China, 6 July 2001.

[36] Weyrich, T.; Matusik, W.; Pfister, H.; Bickel, B.; Donner, C.; Tu, C.; McAndless, J.; Lee, J.; Ngan, A.; Jensen, H.W.; et al. Analysis of human faces using a measurement-based skin reflectance model. ACM Trans. Graph. (ToG) 2006, 25, 1013–1024.

[37] Shi, J. Good features to track. In Proceedings of the IEEE Conference on Computer Vision and Pattern Recognition, Seattle, WA, USA, 21–23 June 1994.

[38] Fitzpatrick, T.B. The validity and practicality of sun-reactive skin types I through VI. Arch. Dermatol. 1988, 124, 869–871.

[39] Keel, M.S.; Kim, D.; Kim, Y.; Bae, M.; Ki, M.; Chung, B.; Son, S.; Lee, H.; Jo, H.; Shin, S.C.; et al. A 4-tap 3.5 μm 1.2 Mpixel Indirect Time-of-Flight CMOS Image Sensor with Peak Current Mitigation and Multi-User Interference Cancellation. In Proceedings of the 2021 IEEE International Solid-State Circuits Conference (ISSCC), San Francisco, CA, USA, 13–22 February 2021; Volume 64.

[40] Wang, J.; Warnecke, J.M.; Haghi, M.; Deserno, T.M. Unobtrusive health monitoring in private spaces: The smart vehicle. Sensors 2020, 20, 2442.

[41] Jiang, C.; Yabroff, K.R.; Deng, L.; Perimbeti, S.; Han, X. Prevalence of Underlying Medical Conditions Associated with Severe COVID-19 Illness in Adult Cancer Survivors in the United States. JNCI J. Natl. Cancer Inst. 2021, djab012.

Chapter 5 Contactless Vital Sign Monitoring (CVSM) System for Driver and Passenger Monitoring based on NIR ToF Camera

5.1 Introduction

In this chapter, we built upon the Contactless Vital Sign Monitoring system (CVSM) demonstrated in Chapter 4 to monitor HR and RR of the driver/occupants in a moving vehicle. The CVSM system addresses the challenges of varying ambient illumination as well as the interference from excessive motion by utilizing the active illumination and the additional depth information from the ToF camera. The synchronized 850nm active illumination in the ToF camera allows us to operate independent of the ambient light conditions while the additional depth information can be used to compensate for motion induced intensity artifacts. As the users move in the vehicle (passively or actively), their relative position against the ToF camera also changes, thus the additional depth information measured by the ToF camera is correlated with the motion of the driver. We can therefore compensate the motion-induced intensity artifact using similar method demonstrated in Chapter 4. Furthermore, the depth information is also used to estimate the amount of motion during the measurement period, therefore predicting quality of the HR measurements. Additionally, the depth change from chest wall motion can be used to directly measure RR, thereby allowing our system to measure both HR and RR with one monolithic sensor.

We systematically investigate the performance of our CVSM system by performing HR/RR measurements in various realistic environments with different degrees of motion from the roads and the drivers. Our study finds that with the depth-based motion compensation, HR measurement success rate (defined as measured HR within 10% from the reference HR measurement) increase from 13.6% (when compensation not used) to 71.9% while the user is driving on the highway. When the user is driving on local road, success rate increases to 56% from 12% when motion-based compensation is not used. As for the RR measurement, our CVSM system measures RR of the driver on highway scenario with a mean deviation of -1.4 BPM from the reference RR measurements. With the ability to measure two important physiological parameters with one sensor, we believe our ToF based CVSM system can enable a low-cost, compact, and multi-modal driver monitoring system that can be used for applications such as drowsiness or sudden sickness detection in vehicle.

5.2 Background and Motivation

As Advanced Driver Assistant Systems (ADAS) are increasingly adopted by both car manufactures and regulators, there is a growing need to monitor the physiological states of drivers/occupants to assist the engagement of the ADAS system [1,2,3,4,5]. For example, the EuroNCAP regulation requires the driver/occupants monitoring system (DMS/OMS) to detect sudden sickness as well the presence of younger child in the vehicle [39]. Both HR and RR are shown to be used as indicators to predict the awareness level of the driver, which could in turn be used to determine if ADAS functions such as automatic lane keeping or front collision avoidance should be engaged to ensure the safety of the driver [3,4,5]. Additionally, with emerging autonomous services such as robotic taxis gaining traction [3], an unobtrusive CVSM system can be a valuable addition to ensure the wellbeing of the passengers.

Table 5-1 Summary of HR/RR measurement techniques used in vehicle

Type of Sensor	HR Measurement ?	RR Measurement ?	Contactless ?	HR Robust against Motion?	Ambient Light Resistance?	Independent of Skin Color?
ECG [4,40]	++	**Indirect**	**N**	++	++	++
Radar [4,13,14]	-	**Direct**	**Y**	-	++	++
Ballistocardiograph [41,43]	-	**Direct**	**N**	-	++	++
Thermography [18]	**N/A**	**Direct**	**Y**	**N/A**	++	++
PPG with RGB camera [10,12]	++	**Indirect**	**Y**	+	-	-
PPG with IR camera [9, 11]	+	**N/A**	**Y**	-	+	+
PPG with indirect ToF camera (This Chapter)	+	**Direct**	**Y**	+	++	+

+/- indicates system more/less robust against external interference in certain category; Indirect/Direct refers to if sensor extract RR from measured HR signal or not

Several sensors, such as cameras, radars, ECG, and ballistocardiograph sensors have been studied to extract HR and RR from the driver [4,5,6,7,8,9,10,11,12]. Table 1 summarizes characteristics of various sensors commonly used for HR and RR monitoring of driver/occupants in vehicle. Among various sensors, ECG measures HR from the electrical potential of the heart while the ballistocardiograph sensor measures HR through the micro-motion of the body caused by the heartbeat[41,43]. Even though both radars and cameras promise unobtrusive monitoring of HR and RR, cameras also offer other unique functions such as facial recognition and gaze detection that cannot be achieved with radars. Even though it has been shown that HR can be

measured with ballistocardiograph through video using a RGB camera [43], this method is highly vulnerable to voluntary motion of the user, which makes it a less ideal method for HR monitoring in the vehicle cabin [43]. Alternatively, HR can also be acquired through imaging Photoplethysmography (PPG) where the volumetric change of blood flow from the heartbeat causes different amount of light being absorbed by the user's face [15,16,17,18,19]. Several past studies (such as chrominance (CHROM) or independent component analysis (ICA) based method) have shown robustness of using a camera to contactlessly measure HR in controlled environments [20,21,22,23,24] by utilizing the RGB color channels in an RGB camera.

Compared to measuring HR and RR in a controlled indoor environment, additional challenges from the varying illumination as well as the motion artifacts need to be addressed. When driving a vehicle, the illumination level can vary significantly based on factors such as weather or time-of-day. Any imaging-based sensor will need to be unaffected to the ambient light. Secondly, during driving, both the passive motions from the road or active motions from the users can interfere with the measurement result.

Thus, for a camera-based sensor, a method for rejecting motion induced artifacts is important to ensure reliable HR/RR measurement performance. Recently, several studies have discussed the use of a camera to measure HR in a vehicle [9,10,11,12]. For example, Huang et.al. demonstrated HR monitoring in a driving vehicle with a RGB camera [10]. Nowara et.al. demonstrated an in-vehicle HR monitoring system (Autosparse PPG) using a NIR camera with LED illuminations, where a sparse frequency estimation method is introduced to improve the HR measurement reliability against external artifacts [9]. However, for Autosparse PPG method to be effective, uniform illumination of the user is required, which may not be satisfied when a compact sensor with a localized/point illumination source (such as VCESL lasers) is used. In the

previous chapter, we demonstrate a system using an indirect NIR ToF camera to monitor HR and RR in an indoor environment. We expand the on the previous study and demonstrate a CVSM system for HR and RR measurements in a moving vehicle. In this study, we not only use the depth information to distinguish intensity changes caused by body motion versus heartbeat but also to assess the quality of the HR measurements, which further increase the robustness of the HR measurements against motion-induced artifacts [29]. Since our depth-based method does not make the sparse frequency assumption of the PPG signal, this system would work even if a compact/localized VCSEL illuminator is used. Furthermore, even though RR has been shown to be correlated with the drowsiness or stress level of the driver, the existing camera-based system usually does not have adequate signal quality for RR extraction [25, 26]. To circumventing the limitation of low signal quality, in this study, we use the ToF camera to measure RR directly by measuring the chest wall displacement. avoiding the potential complexity of fusing the data from the radar sensor and the camera respectively and reduce the cost for the entire system.

To the best of our knowledge, this is the first study where a ToF camera is used to simultaneously perform HR and RR measurements in a vehicle. Indirect ToF cameras are becoming increasingly popular on various platforms and are already deployed in vehicles for functions such as Smart Restraint Control System (Smart-RCS). Given the benefits brought by the active illumination and depth information, our CVSM system would enable compact, reliable, and multi-modal physiological signal monitoring in a vehicle, improving the safety and the driving experience for both the drivers and passengers.

5.3 Experiment Setup and Procedure

5.3.1 Hardware Configuration

The indirect ToF camera used in this study is an amplitude modulated ToF camera with resolution of 640×480 with 149° diagonal field of view (FoV). This large FoV can accommodate different seating positions and postures of the driver and can potentially be used to monitor multiple passengers in the vehicle. The active illumination is provided by a pair of 850nm (we find both 940nm and 850nm illumination to have similar performance in terms of HR measurements) VCSELs with diffusers at eye-safe power. As a prototype, the ToF camera has a form factor of ~15cm ×5cm×5cm and consumes 5W average power, which could be further reduced with future packaging improvements. The ToF camera is inherently robust against ambient illumination change: Firstly, the lens of the ToF camera is coated with bandpass filter at 850nm to suppress the out-of-band background illumination. At the same time, the underlying lock-in detection principle of the indirect ToF sensor can suppress the residual in-band background illumination [42].

In our experiment, the ToF camera is mounted in a 2015 Jeep Cherokee near the rearview mirror using an adjustable suction cup mount either facing the driver side of the cabin or the passenger side of the cabin. The ToF camera is positioned at roughly eye level and ~50cm away from the participants. Due to the wide FoV, the ToF can capture the users' face, and chest region at the same time (Fig. 5-1). During our experiments, the ToF camera operates at 30 frames per second (FPS) and each measurement records 20 seconds of video. The frame rate as well as the measurement time are chosen because of the bandwidth as well as the processing power of the laptop. Longer measurements could be chosen to improve the resolution of the HR/RR measurements at the cost of the recoding and processing time. The reference HR is measured

with an EKG-based Polar H10 chest strap (Polar Electro Oy, Finland), while the reference RR is measured through a NUL236 Respiration Monitor Belt (Neulog, Israel). The brightness level in the cabin is also recorded with a light meter (MT912, URCERI)



Figure 5-1 Experimental configuration for HR/RR measurements in vehicle with a ToF camera

5.3.2 HR and RR Extraction

Our system extracts HR using both the average grayscale intensity and depth of ROI-1 on the right cheek region while measuring RR with just the average depth information of ROI-2 on the chest. Compared to our previous chapter [29], the ROI-1 selection is the vehicle needs to adapt for more complex scenario. We only select the smooth region on the right cheek so that the signal is less likely to be affected by the facial hair or the uneven shape of the face. To adapt and track ROI-1 and ROI-2 (Fig. 5-2) from various head pose and seating positions that users could potentially take in a car, a more sophisticated face mesh detection algorithm is used [30] to extract 468 facial landmarks (compared to the 66 land-marks in Chapter 4) from the user's face and the landmarks that encircle the right cheek/nose area are selected as the corner points of ROI-1. After the facial landmarks are extracted, we apply a pose estimator to find the shoulder of the user and define the ROI-2 on the chest using the relative positive between the jawline and the

shoulder. When the user sits ~50 cm from the ToF camera, ROI-1 contains roughly 5000 pixels while ROI-2 contains roughly 8000 pixels.



Figure 5-2 Position of both ROI-1 and ROI-2 as seen by the ToF camera. The grayscale intensity and depth information from ROI-1 are used for HR measurement and the depth information from ROI-2 is used for RR measurements

Figure 5-3 (a) shows a typical intensity as well as the depth captured from ROI-1 while the user is driving on the highway. When a localized illuminator (such as VCSEL used in this study) is used, motions from both the driver and the road create artifacts that are several times larger than the underlying HR signal (Fig. 5-3(a). If left uncompensated, such artifacts will lead to inaccurate HR measurements (unwanted peaks in the frequency domain) (Fig. 5-3b)

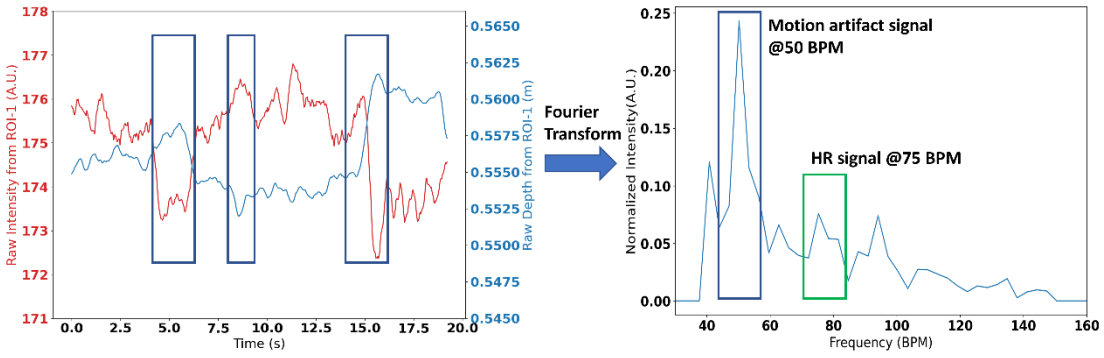


Figure 5-3 (a)Raw intensity (red) and depth (blue) captured by the ToF camera. Depth change induced by motion (blue rectangle) is inversely proportional to the intensity, which is a key source of erroneous HR reading. (b) When motion artifacts are present, they create artifacts frequency components that overwhelm the actual HR signal

In this study, to accommodate for complex driving situations HR is extracted in three major steps (Fig. 5-4): 1. Extract average grayscale intensity and depth information from ROI-1; 2. Compensate for motion induced intensity artifacts using depth information; 3. Use depth information to assess the quality of different sections within the video and extract HR from the processed signal. Because the user in a moving vehicle will encounter more random motion, compared to the method in the previous chapter, the last step is added to further differentiate signal sections with more motion interference from signal sections with less motion interference.

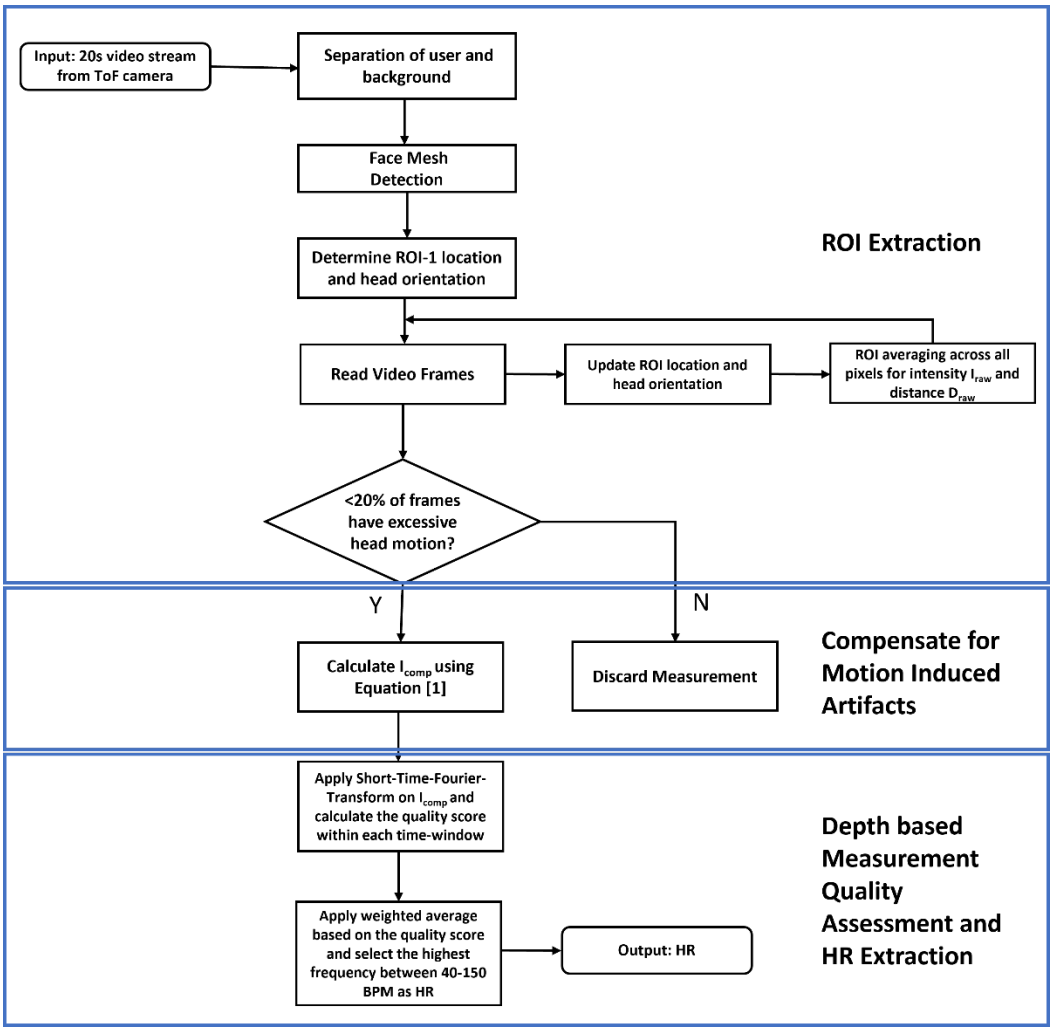


Figure 5-4 Processes to extract HR while driving using depth and grayscale information from a ToF camera

In step 1, before extracting grayscale information as well as depth information from each frame, we first remove the background in each frame by only selecting pixels that are 40 to 70 cm from the camera. The removal of the background in each frame eliminates the interference from the passengers in the backseats. After the background removal, we apply the face mesh detection algorithm to find ROI-1 and average the grayscale intensity and the depth across every pixel in ROI-1 [30]. At the same time the face mesh is obtained, we also determine the head orientation (yaw, pitch, and roll) of the user in each frame using a head pose estimation algorithm [31]. If more than 20% of the frames show excessive head orientation (yaw and pitch deviate more than 10 degrees from head orientation at start), we discard this measurement as the PPG signal can be heavily polluted by head rotation and our depth-based motion compensation method is less effective against intensity changes caused by large head rotation motion [16, 18].

If less than 20% of total frames exhibit excessive head rotation is detected in the video stream, the system moves on to step 2 for the removal of motion artifacts. When an active illumination source such as VCSEL lasers are used, the amount of light that is back scattered to the camera is nonlinearly correlated to the distance between the camera and the participants' face. The voluntary motion from the driver or the involuntary motion caused by uneven roads changes the distance between the driver's face and the light source, resulting in intensity artifacts that could corrupt the HR measurements. Because the ToF camera measures both intensity and depth information, the depth information can be used to compensate for the motion induced artifacts. The depth information obtained from ROI-1, D_{raw} should contain no HR component, while the raw grayscale information from ROI-1, I_{raw} contains both the heartbeat induced intensity change as well as the motion induced intensity change. After the motion artifacts are compensated, the compensated signal I_{comp} should have minimum correlation with D_{raw}. I_{comp} is calculated using

Equation 5-1, where *a* and *b* are the coefficients. We iterated through a range of *a* and *b* to find the minimum the correlation between D_{raw} and $\frac{I_{raw}}{a*(D_{raw})^{-b}}$. In this study, the range of the nonlinear coefficient is set between 0.2 to 5 while the linear coefficient is set as 1 for all measurements taken in this study. More details on the motion compensation method can be found in Chapter 4.

$$I_{comp} = \frac{I_{raw}}{a*(D_{raw})^{-b}} \ , where \ \ a,b = arg\min_{a,b} \ Correlation(\frac{I_{raw}}{a*(D_{raw})^{-b}} \ , D_{raw}) \qquad [5\text{-}1]$$

After the motion artifacts are compensated, we then assess the quality of different sections of the 20s video using both the depth information and Short-Time-Fourier-Transform (STFT). Ideally, for clean HR measurements without artifacts and noise, the measured signal in the frequency domain will contain one peak in the frequency domain (which we select as HR). However, in real-life measurements, various motion artifacts/noises create additional frequency peaks in the frequency domain. Even though we try to compensate for motion induced artifacts in step 2, some large motion or head rotation cannot be effectively compensated. These large motions can come from the driver turning their head or from driving across potholes on the road. If those types of motion are large enough, the amplitude of artifact frequency peak can be higher than the HR frequency component, creating erroneous HR results. Therefore, we use the depth information to determine if such artifacts could exist in a particular section of the recorded signal. The quality assessment is implemented with following steps: 1. The 20s measurements are split into eleven 10s windows with 9s overlap between two consecutive windows. 2. We perform Fourier transform to the 10s window and find the amplitude of highest peak (A_{1st}) and the second highest peak (A_{2nd}) in the frequency domain. 3. We calculate motion score of this 10s window using Equation 5-2. 4. a final spectrum is calculated as the weighted average of all 10 windows

with the inverse of the motion score being the weights (Equation 5-3), where *Xi(f)* is the spectral content of each time window and n is the total number of windows (in this study n=11)

$$\text{motion_score} = \frac{(\text{var}(\text{depth}(t) - \text{mean}(\text{depth}(t))}{A_{1st}/A_{2nd}} \quad [5\text{-}2]$$

$$X_{\text{final}}(f) = \sum_0^n X_i\,(f) * \text{motion_score}(i)^{-1} \quad [5\text{-}3]$$

By applying such weighed average, we reward sections with low motion scores, during which either the user is not moving less, or a clear highest peak can be found in the frequency domain. After the averaged spectrum is calculated, we select the highest frequency component between 40 BPM to 150 BPM as the measured HR.

RR extraction follows the same method as described in Chapter 4 (Fig. 5-5): First, with the pose estimator, we define ROI-2 using the relative position between the chin and the shoulder of the participants. The location of ROI-2 is then tracked in every frame in the 20s video. Then, we calculate the average depth across all pixels within ROI-2. Finally, we apply bandpass filter (5 to 30 BPM) and Fourier transform to the extracted depth signal from ROI-2 and the highest peak in the frequency domain is then chosen as the RR value.

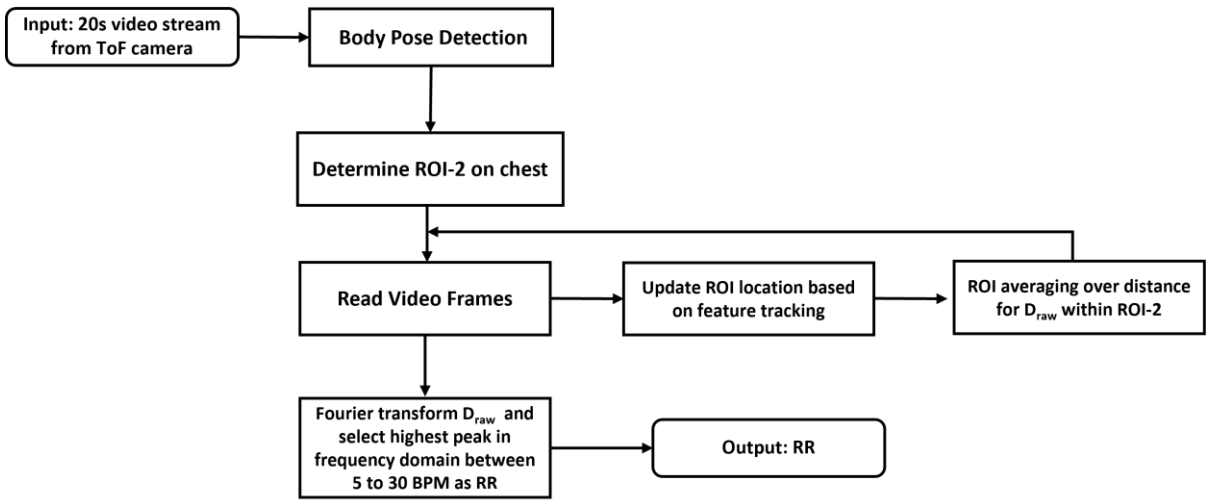


Figure 5-5 Processes to extract RR while driving using depth and grayscale information from a ToF camera

5.2.3 In-Vehicle Testing of the System

To test the system performance and to understand the influences of motion artifacts from various sources, we conduct a series of in-vehicle tests, both on the highway as well as local roads. Our cascaded tests comprise 4 scenarios. Between each scenario, we add one extra source of interference and bring the test scenario closer to a realistic use case. In the first scenario, participants are asked to sit in lab with front face towards the camera. In scenario two, we changed the viewing angle of the ToF camera and added the vibration from engine to the test. Participant are asked to sit in a parked car with the engine running; In the third scenario, participants sit on the passenger seat while being driven on a highway/local road (participants asked to stay still). Compared to the previous scenario, we added the "passive motion artifacts" such as driving on an uneven road as well as making turns. Finally, in the last scenario, we added the voluntary motion from the driver such as checking the traffic conditions and adjusting their seating position while driving. Participants are asked to drive the car themselves on highway/local road, mimicking the real-life operation scenario that the system intended to be used. In total, 6 of the study team members participated in scenarios 1-3, while only 5

participated in scenario 4. During the measurement of each team member, roughly 25 measurements of HR/RR are taken (actual number of samples depends on time the participants spend to drive the designated route), leading to more than 125 measurements for each scenario. In terms of RR measurements, we measure RR of the participants as they drive on the highway while wearing the respiration belt. Table 2 shows the details of the cascaded driving test.

Table 5-2 Testing Condition for Each of the Scenario Tested

Parameters Measured	Test Condition	Number of Participants	Total Number of Measurements	Total Miles Driven
HR	Highway-Passenger	6	141	>70
HR	Highway-Driver*	5	151	>60
HR	Local-Passenger	6	141	>15
HR	Local-Driver	5	143	>12
RR	Highway Driver*	5	135	>60

** Indicate more important application scenarios*

5.4 Experiment Results

5.4.1 HR and RR Measurements in Bright and Dark Lighting Condition

One advantage of using ToF camera is that the 850nm active illumination provided by the VCSEL allows the system to operate independent of the ambient light conditions. Such benefits can be attributed to both the bandpass filter as well as the underlying lock-in detection schematics of the indirect ToF camera [32]. Figure 5-6 shows the images seen by the ToF camera in both bright and dark environments. In the bright environment, the brightness level in the cabin exceeds 1800 Lux while in the dark environment the brightness level is less than 5 Lux.



Figure 5-6 The user's face seen by an RGB camera (a) in both bright (top) and dark (bottom) condition versus the user's face seen by the ToF camera in both bright (top) and dark (bottom) condition

In both bright and dark environment, the image seen by the ToF camera are very similar, and HR can be extracted in both cases (Figure 5-7).

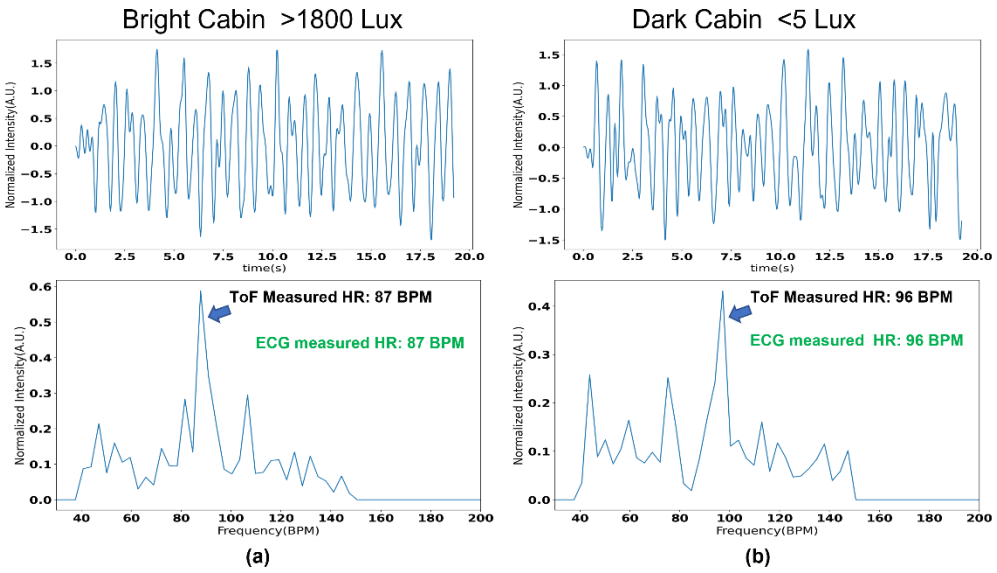


Figure 5-7 Time (Top) and frequency (Bottom) domain of the motion-compensated HR signal in both bright (a) and dark (b) environments

5.4.2 On-the-Road Testing of HR and RR

Figure 5-8 and Figure 5-9 show a waterfall chart of the success rate tested under each of the scenarios (Table 2). The success rates of HR measurements on highway conditions outperform the success rates on the local road conditions in all cases. Such results are expected since the occurrences of both the road bumps and the active driver motion are much more frequent on the local road than on the highway. With the adding of each component of the potential sources of motion artifacts, we can see a degradation of HR measurement performance by different amounts. In the case of the highway scenario, the success rate drops from 90% when measured in the lab to 71.9% when the driver is driving the vehicle on the highway, with the most significant performance drop occurring when we add the voluntary head motions from the driver (i.e., the case when driver drives the car him/herself). As a comparison, the success rate drops to a lower 56% when the driver is driving on the local road. However, the most significant decrease of performances for the local road scenarios seems to arise from the road surface and traffic conditions rather than the driver's active motion. The highway scenario will be the more important use case for the CVSM system, due to higher speed as well as the longer time of driving leading to drowsiness and potentially more catastrophic accidents [32]. We will discuss in detail the system performance under each in-vehicle scenario in the following paragraphs.

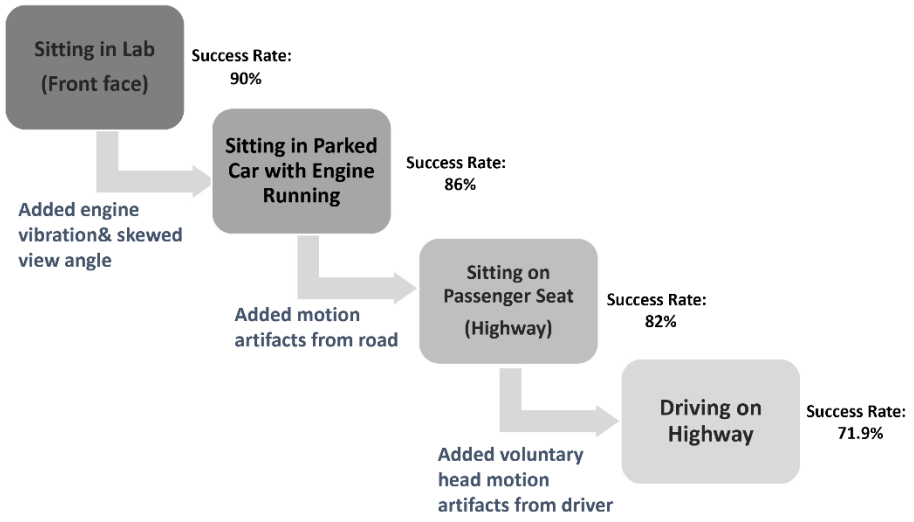


Figure 5-8 Waterfall diagram of the success rate of the HR measurements under different testing scenarios on highway

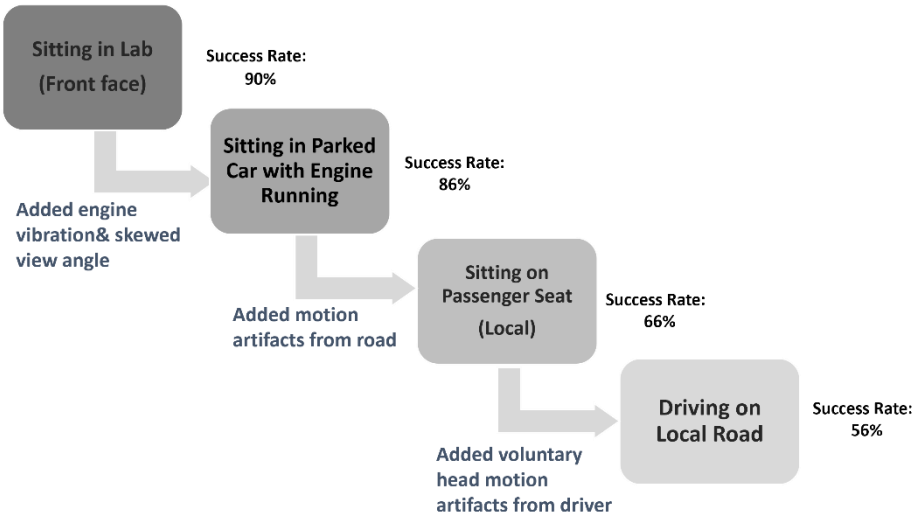


Figure 5-9 Waterfall diagram of the success rate of the HR measurements under different testing scenarios on local road

Figure 5-10 compares the distribution of error rates of the HR measurements with or without depth-based motion compensation when the user is sitting in a parked car with engine running. An HR measurement from our CVSM system is defined as 'successful' if the measurement is within 10% of the of the HR measured by our reference device, a Polar H10 chest strap. In the following analysis, "motion-compensated" refers to HR measurements utilizing both grayscale intensity and depth information for motion compensation.

"uncompensated" measurements refer to the HR measurement using the same grayscale intensity as the "compensated" HR measurements, but not using the depth information for motion compensation (as is the case of a normal 2D camera). Similar to our findings in Chapter 4, with the depth-based motion compensation, the success rate is 86% while the success rate drops to 36.5% when the motion compensation is not used. Even though the participant is sitting still in their seat, there still exist involuntary motion which can obfuscate the HR signal if left uncompensated.

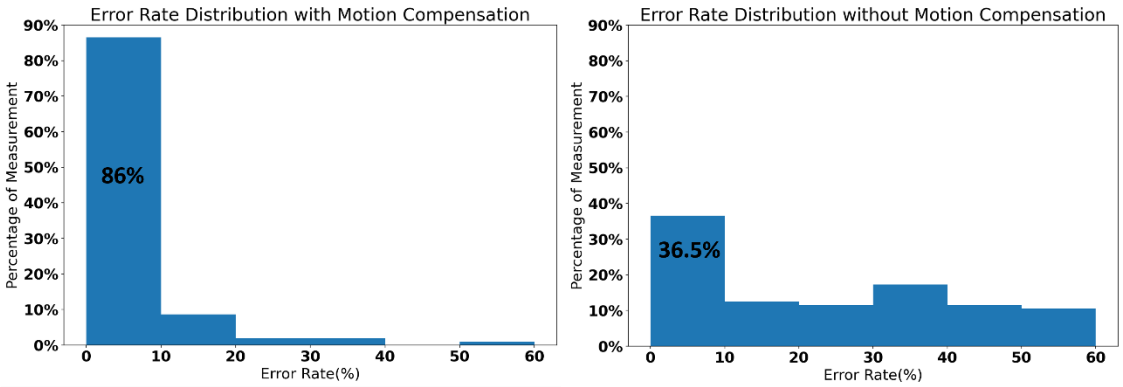


Figure 5-10 HR measurements error rate when participants sit in a parked vehicle with motion compensation (left) and without motion compensation (right)

Figure 5-11 shows the Bland-Altman plot of the HR measurements in the parked vehicle with engine running. With depth-based motion compensation enabled, the mean deviation of the HR measurements from is -2.9 BPM and 95% of the measurement deviations falls between +/- 19.6 BPM of the mean deviation. When depth-based compensation is not used, we observe a much higher negative bias of -16.3 BPM with 95% of deviation falls between +/-35 BPM of the mean. Such larger bias is usually caused by the lower frequency motion artifacts being mistakenly recognized as HR.

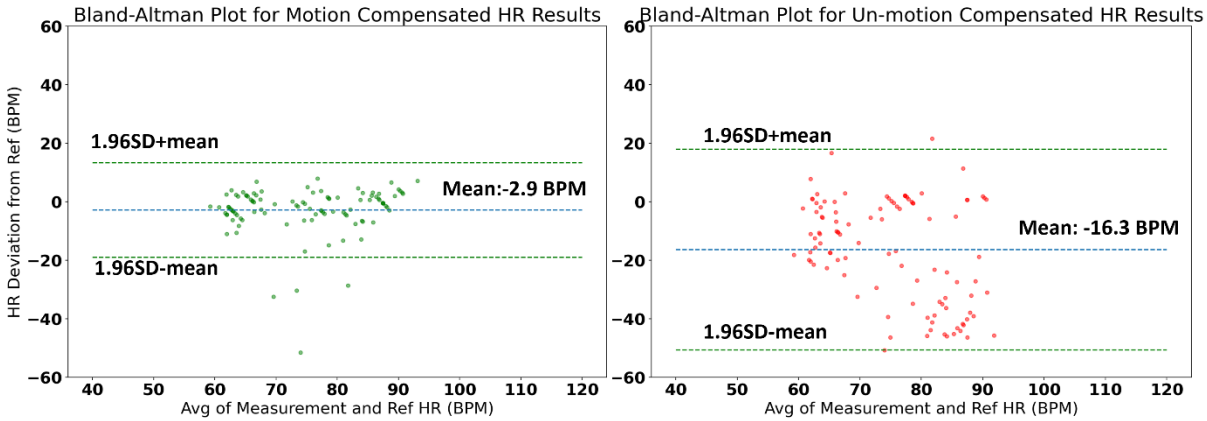


Figure 5-11 Bland-Altman plot of HR measurements when participants sit in parked vehicle with motion compensation (left) and without motion compensation (right)

Testing on Highway:

Once on the road, the car motion from the road bumpiness starts to affect the performance of HR measurements. Figure 5-12 shows the histogram of the error rates when the participants are sitting on the passenger seat while the car is driving on the highway. The participants are asked to not move their heads during the measurements to suppress active head motion. Since there is less road roughness and distractions from traffic signs/lights or pedestrians on the highway, we did not observe significant degradation of HR measurement success rate. Figure 5-13 shows the Bland-Altman plot for the HR measurements under the same conditions. The mean deviation for the motion compensated case is 0.13 BPM (absolute mean deviation at 5.8 BPM) and the 95% of deviation within +/- 22 BPM from the average deviation. When motion compensation is not used, the success rate drops to 34% while the mean deviation increases to -19BPM (absolute mean deviation at 20.5BPM).

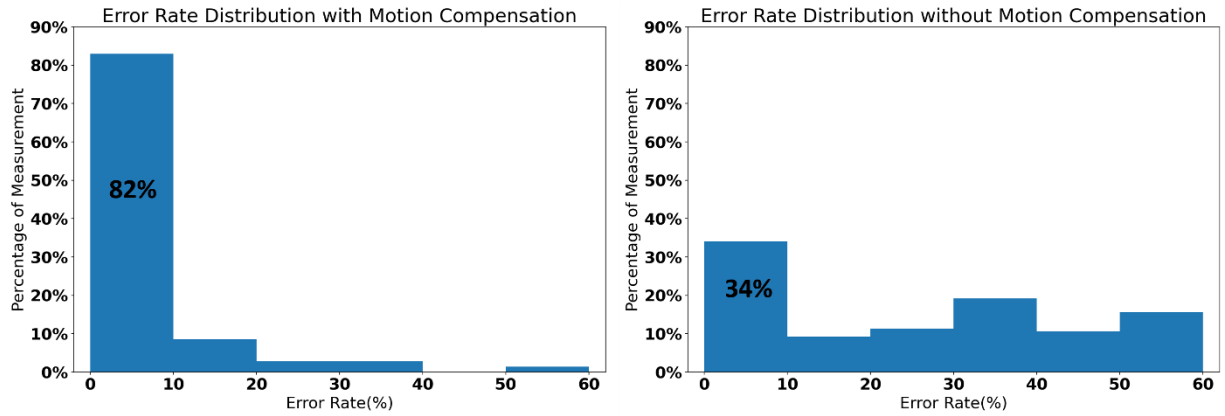


Figure 5-12 HR measurements error rate when participants sit in passenger seat on highway with motion compensation (left) and without motion compensation (right)

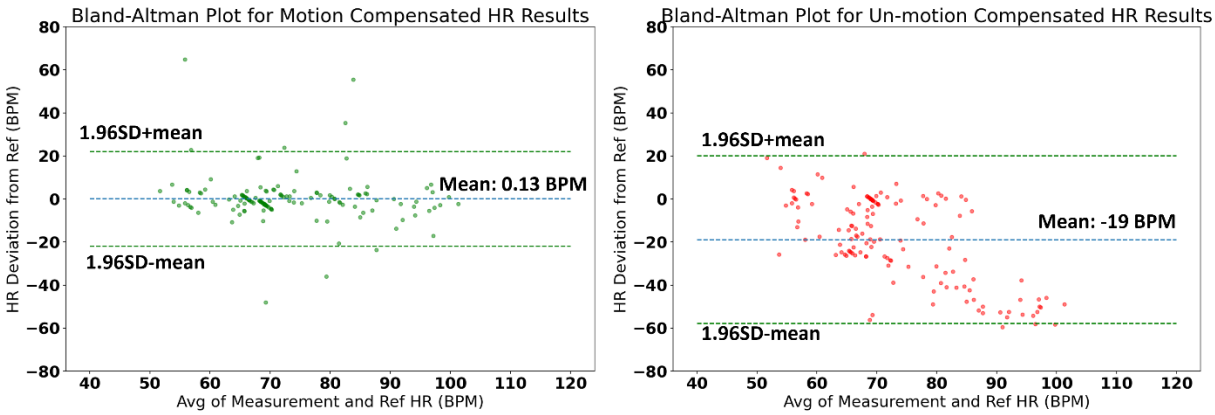


Figure 5-13 Bland-Altman plot of HR measurements when participants sit in passenger seat on highway with motion compensation (left) and without motion compensation (right)

Figure 5-14 and Figure 5-15 show the error rate distribution as well as the Bland-Altman plot for the HR measurements when the participants drive the vehicle on the highway. Because the participants need to turn their head occasionally to check traffic or change lanes, these head motions translate into large motion artifacts that add further complexity to HR measurements. Even though such motions only last for a few seconds, they could still induce motion artifacts that are large enough to disrupt the HR measurements. With the depth-based motion compensation enabled, the HR measurements success rate is 71.9% (absolute mean deviation: 7.7 BPM) while the success rate with no compensation is only 13.6% (absolute mean deviation:

25 BPM). From the Fig. 5-15, we can see more of the wrong HR readings clustered at the bottom of the graph, which are the results of the additional motion artifacts from the driver's motion. We will discuss potential ways of mitigating such outliers later in the discussion section.

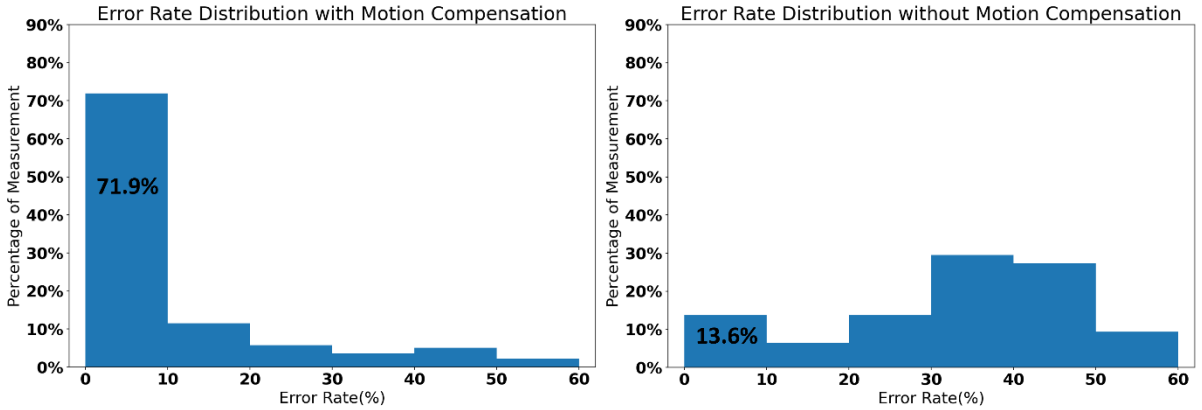


Figure 5-14 HR measurements error rate when participants drive on highway with motion compensation (left) and without motion compensation (right)

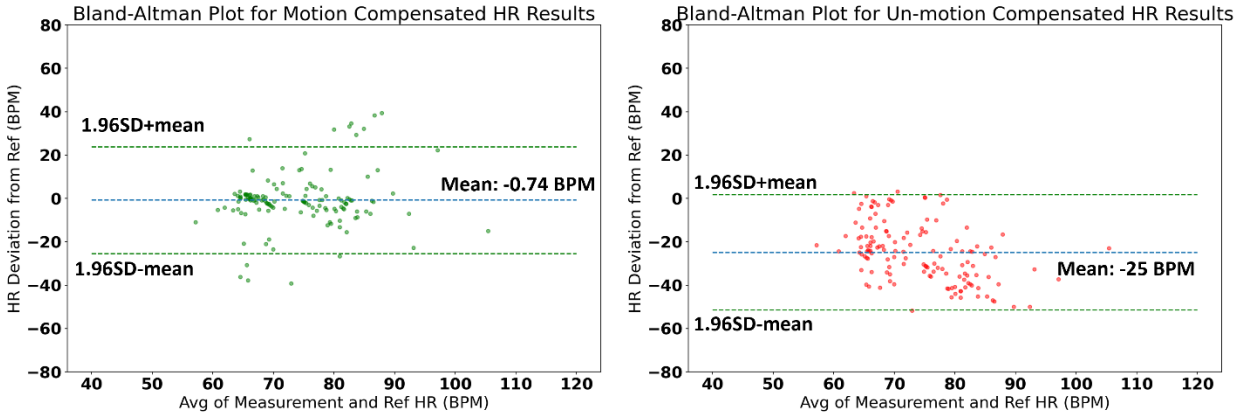


Figure 5-15 Bland-Altman plot of HR measurements when participants drive on highway with motion compensation (left) and without motion compensation (right)

Testing on Local Road:

When testing the CVSM system on the local road, we observe the same performance improvement brought by the depth-based motion compensation. Figure 5-16 and Figure 5-17 show the error rate as well as the Bland-Altman plot for HR measurements for the local road and participants on passenger seat scenario. Because both the road surface condition (roughness,

potholes) and the traffic (number of stop signs, number of cars) are much worse compared to the highway scenario, the success rate degradation for the HR measurements is also more severe. With the participants sitting on the passenger seat, the success rate is 66% (absolute mean deviation 8.4 BPM) with motion compensation and only 22% (absolute mean deviation 22 BPM) for HR measurements without motion compensation.

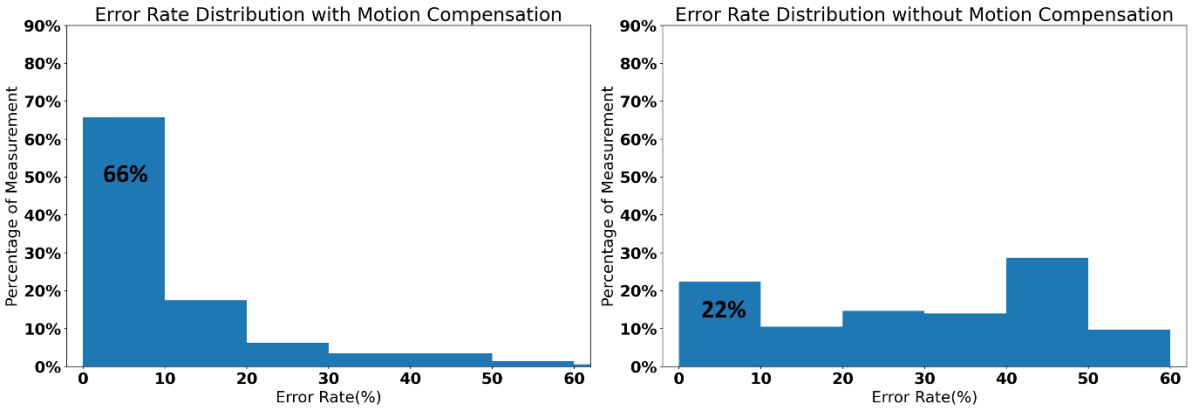


Figure 5-16 HR measurements error rate when participants sit in the passenger seat on local road conditions with motion compensation (left) and without motion compensation (right)

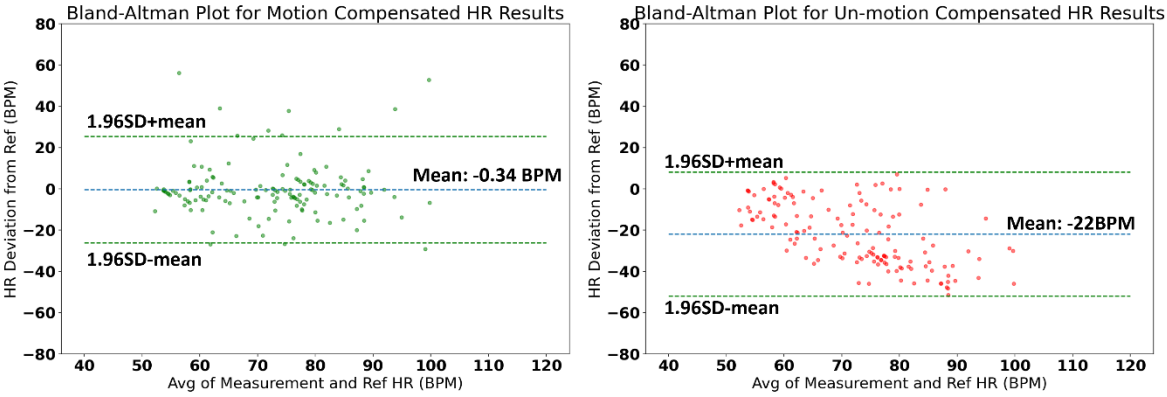


Figure 5-17 Bland-Altman plot of HR measurements when participants sit in the passenger seat on local road conditions with motion compensation (left) and without motion compensation (right)

When the participants move on to drive on the local road, we see similar HR measurements degradation (~10%) as the highway scenario (Fig.5-18, 5-19). With motion compensation, the success rate of the HR measurements is 56% (absolute mean deviation 10.5

BPM) when depth-based motion compensation is used and only 12% (absolute mean deviation 25 BPM) when the depth-based motion compensation is not used.

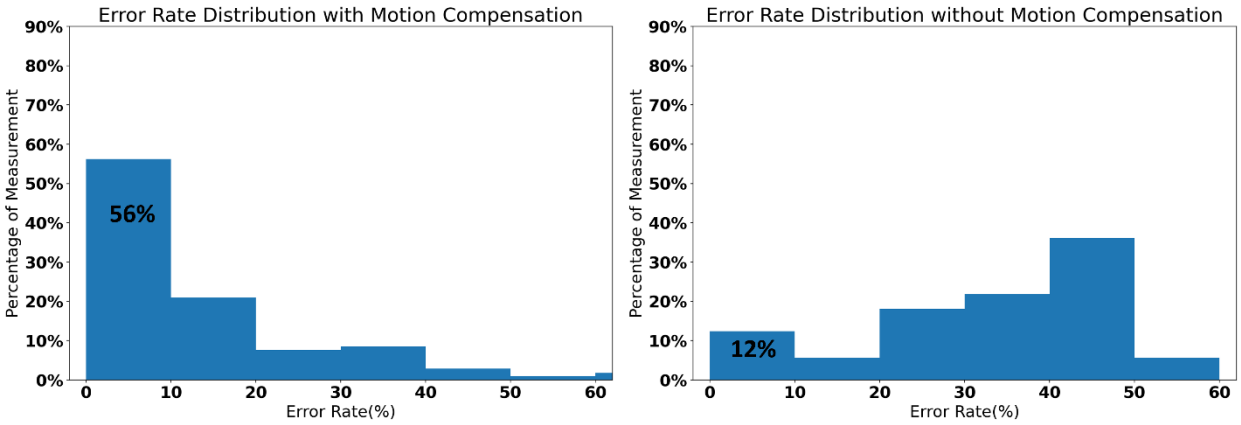


Figure 5-18 HR measurements error rate when participants drive on a local road with motion compensation (left) and without motion compensation (right)

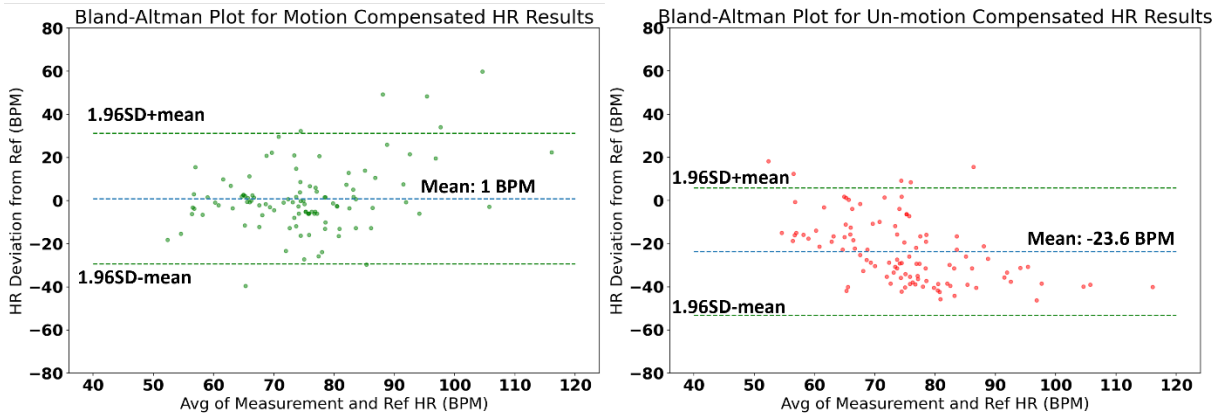


Figure 5-19 Bland-Altman plot of HR measurements when drive on a local road with motion compensation (left) and without motion compensation (right)

RR Measurements on Highway:

In this study, RR is also measured on participants while driving on the highway. Figure 5-20 shows typical respiration motion acquired on the chest region compared with the reference chest belt on the highway. The ToF camera measures typical chest wall depth change of ~±2mm, with the pattern matches with the pressure change measured by the reference respiration belt.

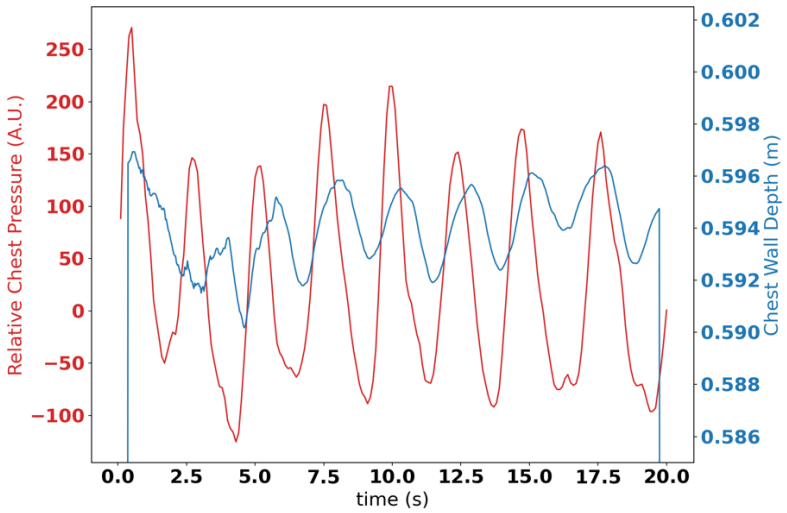


Figure 5-20 Typical RR motion measured by ToF camera (blue), and the RR measured by the reference respiration belt (red)

Figure 5-21 shows the distribution of the deviation of RR measurements from the reference respiration monitoring belt. The mean deviation from the reference reading is found to be -1.4 BPM with a total of 71% of measurements falling within the error of +/- 3BPM. It should be noted that since RR is extracted through the Fourier transform of a 20s measurement, the reference RR measurements is limited to a resolution of 3 BPM. In our measurements, we could sometimes see some extreme outliers with error as large as -10 BPM. These errors could be attributed to events such as driving over potholes or the participants adjusting themselves for a more comfortable position while driving.

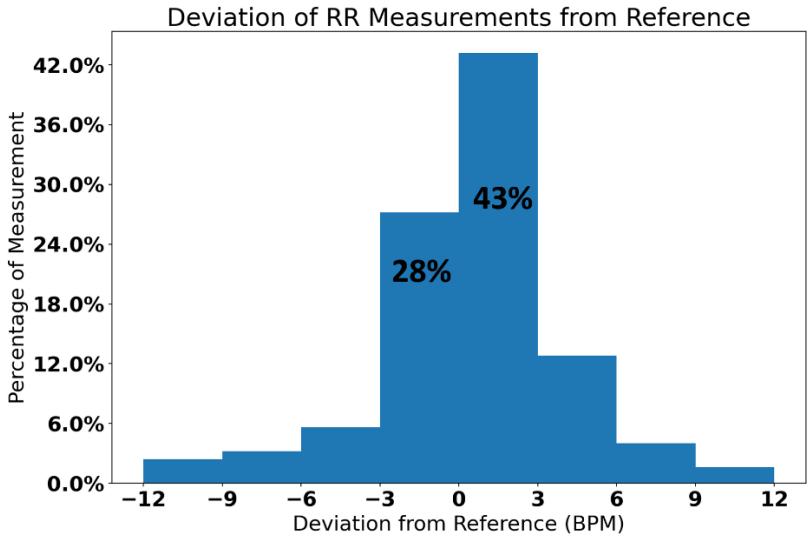


Figure 5-21 Percentage of ToF based RR measurements versus deviation from reference respiration belt

5.5 Discussion

In the previous chapters, we have shown the benefits of using the both the active illumination and depth information from an indirect ToF camera for HR and RR measurement in vehicle. However, because of the complex environments with a vehicle cabin, it is worth discussing the potential limitations of the current methods and exploring potential approaches that could be used to improve the robustness and accuracy of our CVSM system.

5.5.1 Potential Limitations and Improvements for HR measurements

To obtain HR reliably, the system needs to keep track of the same ROI accurately across all frames. Facial expression, or facial occlusions could all interfere with the acquisition of ROIs on the face. If the vertices of the ROI are jittering from frame to frame, the system could mistake the ROI jittering frequency as the HR. For example, Figure 5-22 shows an example where the blinking of the participant interferes with the HR measurement. The participant is asked to blink his eye at the same frequency of an external metronome at 115 BPM (selected to be out of the normal range of the participant's resting HR). The periodic bright reflection from the eye causes

the ROI-1 locations to jitter at the same frequency, which introduces an artifact frequency that overwhelms the true HR frequency component. Since this type errors rises from the jittering of ROI locations, they could potentially be mitigated by using a face tracking algorithm that is less sensitive to external interference. Also, one possible solution is to check the grayscale intensity change against the position change of the ROIs to make sure the dominating frequency peak in the frequency domain is not from the jittering of ROIs [10].

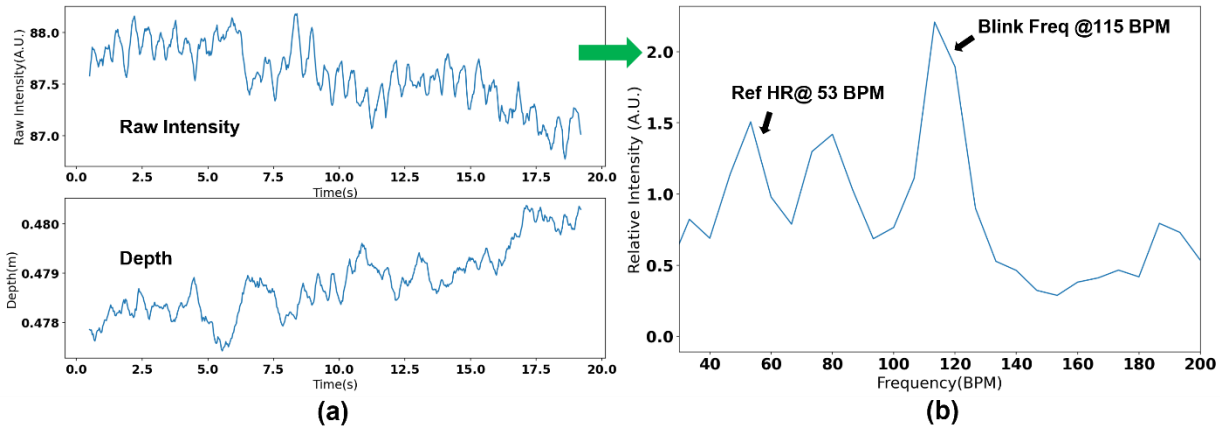


Figure 5-22 Periodic reflection from participant blinking could affect the location of the ROI-1 to jitter. The jittering can lead to additional intensity artifacts that will not be captured by the depth signal (a), leading to erroneous HR reading from the frequency domain (b)

In addition to the interference to the ROI acquisition, subtle motions such as facial expression change and talking could also limit the performance of the CVSM system because these motions could introduce motion artifacts without causing detectable depth changes from the ROI [29]. These subtle artifacts that are confined to localized areas on the face could be alleviated with method such as the sparse frequency estimation and will be discussed in the later sections.

Moreover, a unique challenge to monitoring HR in a vehicle is the sudden motions from either the driver/passenger or the road conditions. In order to capture these motions accurately, it might be beneficial to use a camera with higher frame rate. To investigate the potential benefits of using a higher frame rate camera, we measure HR on three participants while driving on the

highway at 60 FPS (compared with 30 FPS in the experiment section). The acquired 60 FPS videos are then down-sampled (only using every other frame in the original video) to 30 FPS and 15 FPS to compare the performance of HR measurements at different frame rates. Therefore, each frame captured at 60/30/15 FPS shares the same integration time and therefore same background noise. Figure 5-23 shows the error rate distribution for the HR measurements on the highway. With a higher frame rate (60 FPS), the motion across two consecutive frames is smaller, which makes tracking the ROI easier when sudden or large motions are present. In our preliminary test, the original 60 FPS videos result in success rate of 76% while the down-sampled 30 FPS videos leads to a reduced success rate of 68%. When the frame rate is further reduced to 15 FPS, a further degradation of the success rate to 58.7% is observed.

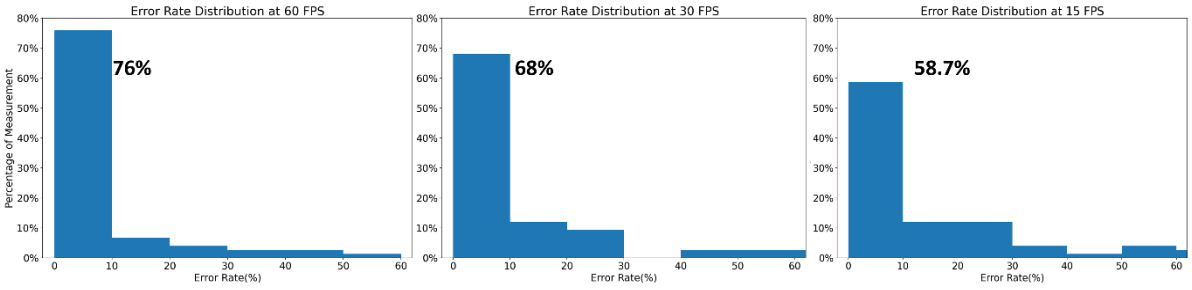


Figure 5-23 HR measurements error rate when participants drive on highway recorded at 60 FPS (left) and 30 FPS (right)

The given benefits of higher frame rate could be attribute to the smaller motion between two consecutive frames. For example, if we assume the user is sitting at 50cm away from the camera, for the ToF camera with 149-degree diagonal FOV and half inch imaging sensor size (diagonal), we could roughly calculate how many pixel will the ROI landmarks shift across two different frames using equation 4, where D_{user} is the distance between the user and the driver, θ is the half angle of the horizontal field of view, L is the horizontal size of the imaging sensor, μ is the pitch of the pixel, v is the velocity of the motion and FPS is the frame rate of the camera.

$$N_{pixel} = ceiling(\frac{D_{user} * \tan(\theta)}{L * \mu} * v/FPS) \quad [5\text{-}4]$$

By doing this calculation, we are assuming that the image fills the entire sensor, and the active area of the pixel is small. In this case, we consider the head of the user is moving at 50cm/s (typical for a fast head turning) and Table 3 shows the number of pixels the ROI landmark would transit at different frame rate.

Table 5-3 Success rate and number of pixels transitioned across two consecutive frames at different frame rates

Frame Rate (FPS)	**15**	**30**	**60**	**105**
N_{pixel} (pixels/frame)	**7**	**4**	**2**	**1**
Success Rate	**56.7%**	**68%**	**76%**	**N/A**

Lower the frame rate, the larger motion (more pixels transitioned) seen by the face tracking algorithm between two frames and therefore higher possibility for the face tracker to output erroneous estimation of facial landmark positions [9]. The erroneous landmarks can cause the detected ROI-1 to change over time, leading to average intensity change over time in the measured signal. When the frame rate reaches ~105 fps, the motion across two consecutive frames will not move more than 1 pixel across different frames. Of course, higher frame rate does not solve all the challenges of HR measurements in NIR, but it should alleviate the burden of the motion compensation as well as the face tracking algorithm. In the future, with ToF cameras of higher resolution and frame rate being developed [33], the robustness of tracking fast motion could be increased and reduce the effects of driver's active motion to the HR measurements.

Another potential improvement for the CVSM system proposed in this chapter is to combine the depth-based motion compensation with other post-processing methods to improve the reliability of the HR measurements. For example, in the 2020 study from Nowara et al. [9], a sparse matrix estimation method is used to further reject noise from the remote PPG signal. The sparse matrix estimation method makes the assumption that HR signal is common across different ROIs on the face while the noises/artifacts will differ within different ROIs. Therefore, by extracting the common signal across multiple ROIs, one can differentiate the HR signal from the external interferences. However, such method may not be directly applicable to the CVSM demonstrated in this chapter because the localized VCSEL source causes intensity from all regions on the face to change in a same pattern against motion from the user. If different ROIs on the face shares the same artifacts/noise, the sparse frequency matrix method from [9] could still pick the artifacts/noises as the HR signal. For example, Figure 5-24 shows an example of an erroneous HR measurement using the sparse matrix estimation method. We extract intensity signals from three ROIs from cheek, nose and forehead, respectively and apply the Autosparse PPG method from [9] to the extracted signals to find the common frequency component across these three ROIs. Fig.25 (a) show the signals from cheek, nose and forehead shows similar pattern of artifacts. Therefore, even though the sparse frequency estimation method correctly identified the HR at 62 BPM, it also included the artifacts that is common to the three ROIs into the extracted frequencies (Fig.25 (b)).

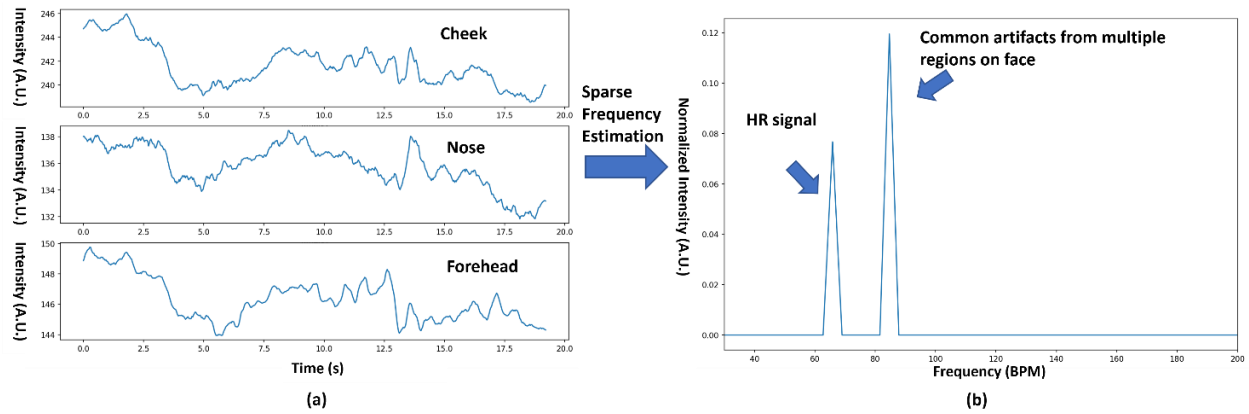


Figure 5-24 (a)Grayscale signal from three different ROIs on face captured with the VCSEL illuminated ToF camera, showing similar patterns of artifacts among all three ROIs. (b)Extracted sparse frequency component using method in [9], showing both HR and artifacts frequency components

One potential solution to this challenge is to also utilize the fact that HR is usually slowly varying in time. One could potentially find the sparse frequency that is common across both multi regions on face as well as within several consecutive HR measurements in time. By combining both time and multiple ROIs on face, such method could hopefully further reject noises from the compensated HR signal and improve the signal reliability.

Finally, in this chapter, the open-source face landmark identification and tracking algorithms [30] are trained mostly with RBG images in various environments and therefore may not be optimized for videos that are taken in the NIR spectrum. In the future, commercially available face tracking algorithm (i.e., Visage, Seeing Machine, Emotion3D etc.) specifically designed for the facial landmarks tracking on NIR videos in driving environment might be used to improve the robustness against sudden motion or reflection glares. With the help of a more optimized face tracking algorithm, one could alleviate the problems from either sudden motion or reflection glares mentioned in the previous discussion, which in turn improve the reliability and accuracy of the HR measurements in the vehicle.

5.5.2 Potential Limitations and Improvements for RR measurements

Regarding using a ToF camera for RR measurements, a natural question to ask is how would different types of clothing (that could block or dampen the motion of the chest wall) affect the performance of RR measurement using the ToF camera. Even though the ToF camera offers the capability of directly measuring RR similar to a millimeter-wave radar, one drawback is that the 850nm light cannot penetrate clothes compared to the millimeter wave used in radar. To test the effect of clothing, we measure the depth change on ROI-2 while the participants wearing clothes of different degrees of thickness (Fig. 5-25). Fortunately, in all cases, even including the case of a thick down jacket, we were able to detect the chest wall motion from respiration in various commonly worn clothes (Fig. 5-26). Only when the participant is purposefully wearing multi-layer "puffy" cloths with air gaps in between, we started to see the errors on RR measurements increasing as the puffy clothing started to block the chest motion from the camera (Fig. 5-27) (Table 5-4). Finally, it should still be noted that the amplitude of the chest motion is only ± 2mm, and the RR is derived solely from the depth data. In the existence of large external motion, it is still possible for the excessive motion to corrupt the RR measurements. Such limitation could be mitigated by adding complementary RR measurements methods such as RR extraction from HR variability or through extra sensors such as thermal cameras that are co-equipped in the vehicle [18,19,25].



Figure 5-25 Types of clothes worn by participants in this chapter. Participants are asked to sit in a parked car with engine running and breathe naturally during the measurements.

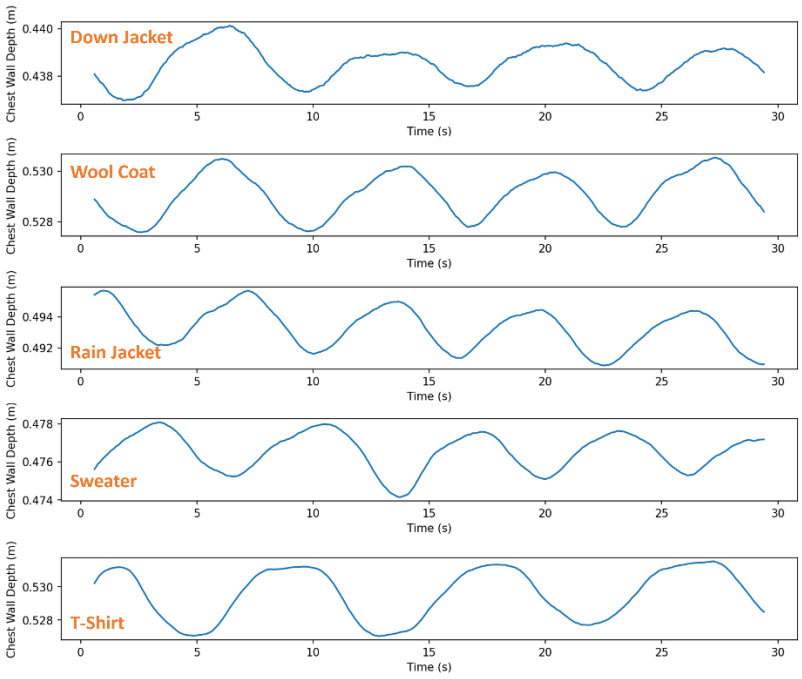


Figure 5-26 Respiration motion on chest measured by the ToF camera while the participants are wearing different types of clothing. Clear respiration patterns can be clearly seen in all cases.

Table 5-4 Absolute mean error of RR measurement when the participant is wearing different type of clothing

Clothing	T-Shirt	Sweater	Rain Jacket	Wool Coat	Down Jacket	Multi-layer Clothing
Absolute Mean Error (BPM)	1.77	1.56	1.51	1.02	1.75	3.57

**** "Multi-layer" clothing refers to wearing several different cloths with air gaps in between.***

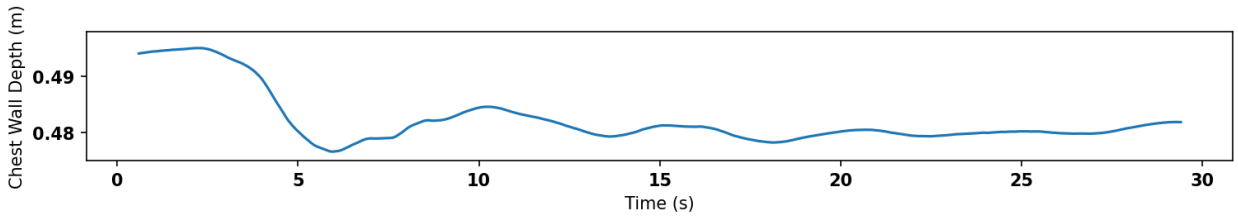


Figure 5-27 Respiration motion on chest while the participants are wearing multi-layer cloth with air gaps in between. The chest wall motion measured by the ToF camera is attenuated due to the clothes' poor contact with body.

5.6 Chapter Summary

In this chapter, we first present a non-distracting, CVSM system that can monitor the HR and RR for both passengers and drivers in a vehicle using an indirect ToF camera. The ToF camera allow us to mitigate two major challenges for measuring HR in a moving vehicle, namely, varying illumination level and motion artifacts [9]. Compared to a conventional 2D camera, ToF camera is inherently robust against the ambient light fluctuation that is commonly encountered in a moving vehicle. Moreover, the ToF camera also provides additional depth information that can be used to compensate for the motion induced intensity artifacts. In this study, the depth information is first used to compensate for the motion-induced artifact and then to assess the quality of HR signal within different sections within the HR measurement (20s

video/measurement). In addition, with the depth information from the ToF camera, the CVSM system can measure RR directly from chest wall motion.

We conduct a series of on-the road testing to evaluate the performance of the CVSM system in realistic operation environment. We first show that because of the 850nm active illumination, the system can measure HR independent of ambient light condition. We then show that the depth-based motion assessment/compensation greatly improves the HR measurement success rate. When the user is sitting in the parked vehicle with engine running, the CVSM system can measure HR with 86% success rate with motion compensation and only 36.5% success rate when only the 2D grayscale information is used. Such improvement becomes more evident on more complex driving scenarios. When measuring passenger while driving on the highway and local roads, the success rate is 82% (34% without compensation) and 66% (22% without compensation), respectively. Ultimately, in the case of measuring users driving the vehicle, the compensated HR measurement achieves success rate of 71.9% and 56% on highway and local roads, respectively, as compared to just 13.6% and 12% when only the grayscale information is used. Even with motion compensation, the HR measurement on the local road remains the most challenging task since both the road unevenness and driver's active motion are more significant in this case. Moreover, we show RR measurement on highway driving scenarios with an average deviation of -1.4 BPM.

The limitations to the HR measurements with the CVSM system comes from effects such as facial expression, sudden motion or even reflection glares from the driver. These limitations could potentially be alleviated using a higher frame rate ToF camera or using other post-processing algorithms to further reject the intensity artifacts. As for the RR measurement, even though the 850nm illumination does not penetrate as deep as a millimeter-wave radar, our

CVSM system is still able to measure the respiration pattern of the chest wall when the user is wearing various types of clothing. With its robustness against both ambient light and motion artifacts, the ToF-based CVSM system could be the key enabler in a low-cost and compact driver /occupant monitoring system in the vehicle and the physiological information measured by the system could one day empower a safer and more functional ADAS system.

REFERENCES

[1] Ziebinski, Adam, et al. "Review of advanced driver assistance systems (ADAS)." AIP Conference Proceedings. Vol. 1906. No. 1. AIP Publishing LLC, 2017.

[2] Ziebinski, Adam, et al. "A survey of ADAS technologies for the future perspective of sensor fusion." International Conference on Computational Collective Intelligence. Springer, Cham, 2016.

[3] Béquet, Adolphe J., Antonio R. Hidalgo-Muñoz, and Christophe Jallais. "Towards mindless stress regulation in advanced driver assistance systems: a systematic review." Frontiers in psychology 11 (2020): 3406.

[4] Wang, Ju, et al. "Unobtrusive health monitoring in private spaces: The smart vehicle." Sensors 20.9 (2020): 2442.

[5] Patel, Mitesh, et al. "Applying neural network analysis on heart rate variability data to assess driver fatigue." Expert systems with Applications 38.6 (2011): 7235-7242.

[6] Kiashari, Serajeddin Ebrahimian Hadi, et al. "Monitoring the variation in driver respiration rate from wakefulness to drowsiness: a non-intrusive method for drowsiness detection using thermal imaging." Journal of Sleep Sciences 3.1-2 (2018): 1-9.

[7] Fujiwara, Koichi, et al. "Heart rate variability-based driver drowsiness detection and its validation with EEG." IEEE transactions on biomedical engineering 66.6 (2018): 1769-1778.

[8] Leonhardt, Steffen, Lennart Leicht, and Daniel Teichmann. "Unobtrusive vital sign monitoring in automotive environments—A review." Sensors 18.9 (2018): 3080.

[9] E. M. Nowara, T. K. Marks, H. Mansour, and A. Veeraraghavan, "Near-Infrared Imaging Photoplethysmography During Driving," in IEEE Transactions on Intelligent Transportation Systems, doi: 10.1109/TITS.2020.3038317.

[10] Huang, Po-Wei, Bing-Jhang Wu, and Bing-Fei Wu. "A heart rate monitoring framework for real-world drivers using remote photoplethysmography." IEEE journal of biomedical and health informatics 25.5 (2020): 1397-1408.

[11] Magdalena Nowara, Ewa, et al. "SparsePPG: Towards driver monitoring using camera-based vital signs estimation in nearinfrared." Proceedings of the IEEE conference on computer vision and pattern recognition workshops. 2018.

[12] Zhang, Qi, et al. "Heart rate extraction based on near-infrared camera: Towards driver state monitoring." IEEE Access 6 (2018): 33076-33087.

[13] Lee, Yee Siong, et al. "Monitoring and analysis of respiratory patterns using microwave doppler radar." IEEE journal of translational engineering in health and medicine 2 (2014): 1-12.

[14] Zhao, Peijun, et al. "Heart rate sensing with a robot mounted mmwave radar." 2020 IEEE International Conference on Robotics and Automation (ICRA). IEEE, 2020.

[15] W. Verkruysse et al., “Remote plethysmographic imaging using ambient light,” Opt. Express, vol. 16, no. 26, pp. 21434–21445, Dec.2008.

[16] Mayank Kumar, Ashok Veeraraghavan, and Ashutosh Sabharwal, "DistancePPG: Robust non-contact vital signs monitoring using a camera," Biomed. Opt. Express 6, 1565-1588 (2015)

[17] Wang, Wenjin, et al. "Algorithmic principles of remote PPG." IEEE Transactions on Biomedical Engineering 64.7 (2016): 1479-1491.

[18] Sun, Guanghao, et al. "Remote sensing of multiple vital signs using a CMOS camera-equipped infrared thermography system and its clinical application in rapidly screening patients with suspected infectious diseases." International Journal of Infectious Diseases 55 (2017): 113-117.

[19] Negishi, Toshiaki, et al. "Contactless vital signs measurement system using RGB-thermal image sensors and its clinical screening test on patients with seasonal influenza." Sensors 20.8 (2020): 2171.

[20] G. de Haan and V. Jeanne, “Robust pulse rate from chrominance-based rPPG,” IEEE Trans. Biomed. Eng., vol. 60, no. 10, pp. 2878–2886, Oct. 2013.

[21] Cheng, Juan, et al. "Illumination variation-resistant video-based heart rate measurement using joint blind source separation and ensemble empirical mode decomposition." IEEE journal of biomedical and health informatics 21.5 (2016): 1422-1433.

[22] Feng, Litong, et al. "Motion-resistant remote imaging photoplethysmography based on the optical properties of skin." IEEE Transactions on Circuits and Systems for Video Technology 25.5 (2014): 879-891.

[23] Van Gastel, Mark, Sander Stuijk, and Gerard de Haan. "Motion robust remote-PPG in infrared." IEEE Transactions on Biomedical Engineering 62.5 (2015): 1425-1433.

[24] Yu, Sun, et al. "Motion-compensated noncontact imaging photoplethysmography to monitor cardiorespiratory status during exercise." Journal of biomedical optics 16.7 (2011): 077010.

[25] P. H. Charlton, T. Bonnici, L. Tarassenko, D. A. Clifton, R. Beale, and P. J. Watkinson, “An assessment of algorithms to estimate respiratory rate from the electrocardiogram and photoplethysmogram,” Physiol. Meas. 37(4), 610–626(2016).

[26] Van Gastel, Mark, Sander Stuijk, and Gerard de Haan. "Robust respiration detection from remote photoplethysmography." Biomedical optics express 7.12 (2016): 4941-4957.

[27] Martinez, Luis F. Corral, Gonzalo Paez, and Marija Strojnik. "Optimal wavelength selection for noncontact reflection photoplethysmography." 22nd Congress of the International Commission for Optics: Light for the Development of the World. Vol. 8011. International Society for Optics and Photonics, 2011.

[28] Moço, Andreia V., Sander Stuijk, and Gerard de Haan. "New insights into the origin of remote PPG signals in visible light and infrared." Scientific reports 8.1 (2018): 1-15.

[29] Guo, Kaiwen, et al. "Contactless Vital Sign Monitoring System for Heart and Respiratory Rate Measurements with Motion Compensation Using a Near-Infrared Time-of-Flight Camera." Applied Sciences 11.22 (2021): 10913.

[30] Lugaresi, Camillo, et al. "MediaPipe: A Framework for Perceiving and Processing Reality." Third Workshop on Computer Vision for AR/VR at IEEE Computer Vision and Pattern Recognition (2019).

[31] Ruiz, Nataniel, Eunji Chong, and James M. Rehg. "Fine-grained head pose estimation without keypoints." Proceedings of the IEEE conference on computer vision and pattern recognition workshops. 2018.

[32] Zanuttigh, Pietro, et al. "Time-of-flight and structured light depth cameras." Technology and Applications (2016): 978-3.

[33] “Traffic Safety Facts”, National Highway Traffic Safety Administration, https://crashstats.nhtsa.dot.gov/Api/Public/ViewPublication/812957

[34] Keel, Min-Sun, et al. "A 4-tap 3.5 m 1.2 Mpixel Indirect Time-of-Flight CMOS Image Sensor with Peak Current Mitigation and Multi-User Interference Cancellation." 2021 IEEE International Solid-State Circuits Conference (ISSCC). Vol. 64. IEEE, 2021.

[35] Qiao, Donghao, et al. "Measuring heart rate and heart rate variability with smartphone camera." 2021 22nd IEEE International Conference on Mobile Data Management (MDM). IEEE, 2021.

[36] Vicente, José, et al. "Drowsiness detection using heart rate variability." Medical & biological engineering & computing 54.6 (2016): 927-937.

[37] Fujiwara, Koichi, et al. "Heart rate variability-based driver drowsiness detection and its validation with EEG." IEEE transactions on biomedical engineering 66.6 (2018): 1769-1778.

[38] Slapničar, Gasper, Mitja Luštrek, and Matej Marinko. "Continuous blood pressure estimation from PPG signal." Informatica 42.1 (2018).

[39] EUROPEAN NEW CAR ASSESSMENT PROGRAMME, “Test and Assessment Protocol-Child Presence Detection” https://cdn.euroncap.com/media/64101/euro-ncap-cpd-test-and-assessment-protocol-v10.pdf

[40] Matsuda, Toshiyuki, and Masaaki Makikawa. "ECG monitoring of a car driver using capacitively-coupled electrodes." 2008 30th Annual International Conference of the IEEE Engineering in Medicine and Biology Society. IEEE, 2008.

[41] Wusk, G.; Gabler, H. Non-invasive detection of respiration and heart rate with a vehicle seat sensor. Sensors 2018, 18, 1463

[42] Foix, Sergi, Guillem Alenya, and Carme Torras. "Lock-in time-of-flight (ToF) cameras: A survey." IEEE Sensors Journal 11.9 (2011): 1917-1926.

[43] Hassan, Mohamed Abul, et al. "Heart rate estimation using facial video: A review." Biomedical Signal Processing and Control 38 (2017): 346-360.

Chapter 6 Summary and Future Work

This dissertation represents my PhD study on both supercontinuum sources as well indirect ToF cameras that could enable contactless and non-invasive inspection and monitoring in both industrial and health applications. In this chapter, we summarize our findings and discuss potential directions that we could take to further improve the results of the current studies.

In Chapter 2, we present the design of an ultra-broadband SC source in LWIR with a nanosecond thulium MOPA configuration. Compared to previous study, the novel cascaded SC generation schemes allow us to generate high output power as well as ultra-broad spectrum at the same time. In our study, we generate 417mW/108mW SC with spectral coverage from 1.57μm to ~11.3μm/1.6μm to ~12μm through a cascade of ZBLAN fiber, As_2S_3 fiber and As_2Se_3/$GeAs_2Se_5$ fiber. The MOPA design eliminate the need of femtosecond OPAs while the use of a cascaded SC fiber chain improves the output power of the SC sources by separating the SC generation process in steps that best matching each SC fiber's spectral expansion capability and power handling capability. This result represents the highest output power generated at such broadband spectrum at the time of publication. Additionally, our beam characterization reveals a single spatial mode output with near diffraction beam quality across the entire wavelength range despite the wavelength dependence of the beam NA. However, since the pump source in our SC design has much lower peak power (~15kW) compared to femtosecond OPAs, much longer SC fibers are needed to generate the broad SC spectrum. We therefore investigate the effects of different fiber parameters on SC generation in LWIR. To effectively generate SC into LWIR, the optical pulse needs to stay confined within core of the SC fibers. Such requirement implies that the SC

fiber to have high NA, low core and cladding loss, as well as an efficient way to couple light from one SC fiber to the other. We satisfy these by requirements by designing a selenide fiber with ~0.76NA,low loss $GeAs_2Se_5$ as cladding which enables high-power SC generation covering both LWIR and MWIR spectral region when pumped by an all fiber MOPA configuration.

In terms of future improvements, the inter-coupling between different SC fibers could be improved to increase the efficiency and reliability of the LWIR SC source. In the current study, the mechanical coupling between ZBLAN and As_2S_3 fiber remains one of the weak points in the SC fiber chain. Currently, to protect ZBLAN fiber tip from environment humidity, the ZBLAN and As_2S_3 coupling interface are sealed with in a nitrogen purged box ("tube-on-groove coupling" in our study). However, one drawback of this mechanical coupling method is that both the coupling efficiency and reliability remains low compared to a fusion splice. Because of the high refractive index of As_2S_3 (~2.4 for As_2S_3 [2]), Fresnel reflection between the air/ As_2S_3 interface alone will cause a 17% of coupling loss between As_2S_3 and ZBLAN. If we could replace such mechanical coupling with a fusion splice between As_2S_3 and ZBLAN fiber, the Fresnel reflection loss could be reduced to ~ 5%. Moreover, removing the air gap between sulfide and ZBLAN fibers also eliminates the need for an airtight enclosure with nitrogen purge, which could in turn improve the reliability of the system and make a truly monolithic all-fiber LWIR SC source possible. In fact, a high efficiency fusion splice between fluorotellurite fiber and As_2S_3 has been achieved recently [3].

In Chapter 3, we design and build SC source-based stand-off spectroscopy system and show our SC sources could enable non-contact, stand-off quality inspection of food samples. Compared with conventional light sources such as halogen lamp, the high brightness and beam quality of SC laser allows a broadband illumination to be projected from a long distance without

sacrificing intensity. Such advantage could increase the SNR of the spectroscopy system, thereby improving the through put of the inspection system or improving the reliability of the system. In our study, we show a good linear relationship between the NIR/MIR spectrum verses key chemical concentrations (such as acrylamide and protein) measured by gold standard methods in food samples. With high brightness and broad spectral coverage, SC sources could eventually enable the online, real-time inspection/monitoring of food ingredients and even other products in an industrial environment.

In the future, for the SC based system to be practically deployed near the production line, both the speed and the pulse-to-pulse stability of the source need to be improved. In our proof-of-concept study, a large percentage of time per measurement is spent on scanning across the wavelength range using the monochromator. For example, for wavelength range from 1100nm to 2500nm with a step size of 5nm, the monochromator will need to move the grating 280 times within a measurement. At an integration time of 300ms, each measurement would take well more than a minute to finish. In an actual system, such speed will not be acceptable. Therefore, one will need to replace the monochromator either with a Fourier transform spectrometer or using an array detector for spectrum recording. Moreover, with the recent development of low-cost quantum dot SWIR camera [4], one could also add the imaging capability to the spectroscopy system, which would allow one to characterize the surface geometry of the sample, which could then be used to compensate for spectral artifacts that are related to surface texture.

Additionally, pulse-to-pulse can also limit system performance in some applications such as agriculture sorting, during which the measurement time per sample could be well within a millisecond. Since our SC sources has a repetition rate from 500kHz to 4MHz, in some cases, each sample can only be illuminated with several hundred pulses during a measurement.

Therefore, we would want to each pulse to have similar spectrum to ensure high SNR and repeatability of the spectroscopy system. However, for SC spectrum generated from nano-second pulses (such as the one used in this study), the majority of the spectra broadening started with the modulation instability. This nonlinear process is seeded from the noises in the initial stage of spectral broadening [5], leading to large variation of spectral content and pulse energy from pulse to pulse. Decades of research have suggested several approaches to control the pulse-to-pulse variation. One approach is to engineer the dispersion property of the SC fiber (either through tapering or photonic crystal fiber) so that a second zero dispersion wavelength can be set to prevent solitons from further red-shifting past this pre-defined wavelength [6]. This method is easier to implement but could potentially limit the spectral expansion to longer wavelength. A more versatile and flexible way to control the instability of SC generation is through seeding the MI pulses with a frequency shifted coherent seed pulse. The seed pulse serves a repeatable source to initiate the MI processing, thereby reducing the shot-to-shot instability and the threshold for the SC generation process[7]. Borrowing from this idea, a potential way to improve the pulse-to-pulse stability of the SC source used in our study is to use a portion of the SC spectrum generated from the previous pulse to seed the SC generation process of the next pulse. By precisely control the timing of seed pulse and the next input pulse, the MI process does not need to be to be initiated from the noise and therefore reducing the randomness of the SC generation process.

Last but not least, unique combination of high beam quality and broadband spectrum of the LWIR SC laser could empower many other applications that would otherwise be hard to achieve with conventional light source. As an example, the light can be coupled into an evanescent waveguide sensor (such as unclad chalcogenide fibers) to enable continuous, high

sensitivity spectroscopy of gas or liquids. Alternatively, LWIR SC laser could enable label free microscopy with better SNR and faster scanning speed, which could prove to become a useful tool in field such as histology, pathology or biomedical imaging.

In Chapter 4, we demonstrate a CVSM system based on an indirect ToF camera. The active illumination of the ToF camera enables 24/7, unobtrusive physiological parameter monitoring of the users. To overcome the dominating motion artifacts associated with the use of the point illumination source, we develop a novel method to compensate for motion artifacts by exploring the relationship between the depth and the motion-induced intensity change. Moreover, the depth information also allows our system to directly extract RR from a participant by measuring the chest wall movement during breathing (instead of acquiring RR indirectly from HR variability). We conduct a pilot study with 29 participants to show that in the indoor environment, the depth-based compensation greatly increases success rate of HR measurements to 75%, as compared to 35% when no depth compensation method is used. Furthermore, we also show that the infrared active illumination makes this system less affected by factors such as environmental lighting or the skin color of the user. In our pilot study, we show that our system performs similarly among participants of different demographics such as skin color, age, and gender.

In Chapter 5, We then further develop the CVSM system to monitor HR and RR in a driving vehicle on both passengers and drivers. In addition to the motion compensation method, we introduced in Chapter 4, we also introduce a new method that assess the quality of HR signal within different sections within the HR measurements to adapt for complex environment in the cabin. Through our systemic on-the-road test on both highway and local road, the HR measurements with the 3D video (using depth information) significantly outperform the HR measurements with only the 2D video. Specifically, when measuring HR on drivers, the compensated HR measurement achieves success rate of 71.9% and 56% on highway and local roads, respectively, as compared

to just 13.6% and 12% when only the grayscale information is used. Furthermore, we also show that the infrared active illumination and lock-in detection principle of the ToF camera make the CVSM system much less affected by the varying illumination encountered during driving.

In the future, the CVSM system could be improved in two ways: Firstly, we could expand the types of physiological parameters that the system can measure. Secondly, the reliability of the existing CVSM system could be further improved so that the system can be deployed in more versatile environments. To measure more physiological parameters, we could utilize other characteristics of the PPG signal beyond just intensity change. For example, studies have shown that blood pressure can be inferred from the pulse transit time of the PPG signal [8]. Similarly, using the blood volume change on the face, one could determine the awareness of the user [9]. To further improve the reliability of the CVSM system, beyond the potential solutions we discussed in Chapter 5, effort can be made to tackle the limitation of the existing motion compensation method. In the current study, motion compensation method shows poorer performance if the users turn their heads to a large angle during the measurement. Improvements can be made by building a more realistic model between the head orientation and the intensity change. In this way, we can use the 3D point cloud from the ToF camera to accurately measures the head pose of the driver and then compensate for the intensity artifacts that are associated with the head pose changes [10]. Another possibility for improving the reliability of HR measurements with ToF camera is to use a similar idea as the CHROM based methods commonly used in RGB cameras. Another wavelength such as 700nm could be added to the ToF camera so that we can utilize the different absorption characteristics of hemoglobin at 700nm vs 850nm to further reject from the intensity artifacts from external interference (e.g., facial expression, head turning, etc.). Even though such method would require significant modification to both the existing ToF cameras and the current motion compensation

method, it could be valuable in solving the challenges from subtle motions (such as during talking) that are harder for the ToF camera to capture.

Reference

[1] Saad, Mohammed. "Heavy metal fluoride glass fibers and their applications." 2011 Asia Communications and Photonics Conference and Exhibition (ACP). IEEE, 2011.

[2] Rodney, William S., Irving H. Malitson, and Thomas A. King. "Refractive index of arsenic trisulfide." Josa 48.9 (1958): 633-636.

[3] Yang, Lingling, et al. "High-coupling efficiency and robust fusion splicing between fluorotellurite and chalcogenide fibers." Infrared Physics & Technology 122 (2022): 104075.

[4] Steckel, J. S., et al. "1.62μm Global Shutter Quantum Dot Image Sensor Optimized for Near and Shortwave Infrared." 2021 IEEE International Electron Devices Meeting (IEDM). IEEE, 2021.

[5] Solli, Daniel R., et al. "Optical rogue waves." Nature 450.7172 (2007): 1054-1057.

[6] Engelsholm, Rasmus Dybbro, and Ole Bang. "Supercontinuum noise reduction by fiber undertapering." Optics express 27.7 (2019): 10320-10331.

[7] Solli, D. R., C. Ropers, and B. Jalali. "Active control of rogue waves for stimulated supercontinuum generation." Physical review letters 101.23 (2008): 233902.

[8] Mukkamala, Ramakrishna, et al. "Toward ubiquitous blood pressure monitoring via pulse transit time: theory and practice." IEEE Transactions on Biomedical Engineering 62.8 (2015): 1879-1901.

[9] Tashakori, Masoumeh, et al. "Estimation of driver drowsiness using blood perfusion analysis of facial thermal images in a driving simulator." Journal of Sleep Sciences 3.3-4 (2018): 45-52.

[10] Fanelli, Gabriele, et al. "Real time head pose estimation from consumer depth cameras." Joint pattern recognition symposium. Springer, Berlin, Heidelberg, 2011.